UNIVERSITY OF CALIFORNIA,
IRVINE

Ultralight Microlattice Materials with Unique Combination of Stiffness and Damping

DISSERTATION

submitted in partial satisfaction of the requirements
for the degree of

DOCTOR OF PHILOSOPHY

in Mechanical and Aerospace Engineering

by

Ladan Salari Sharif

Dissertation Committee:
Professor Lorenzo Valdevit, Chair
Professor Timothy Rupert
Professor Lizhi Sun

2016

DEDICATION

To my mom and dad who taught me to be strong

and empowered me with the courage to follow

my dreams.

TABLE OF CONTENTS

LIST OF FIGURES

LIST OF TABLES

ACKNOWLEDGMENTS

First and foremost, I would like to express my gratitude to my advisor Professor Lorenzo Valdevit for his support, guidance, and patience throughout my master's and Ph.D. degrees. Working with him was a great pleasure that developed me both professionally and personally: I will be always thankful to him for giving me this opportunity.

I would like to extend my sincere gratitude to my committee members, Professor Lizhi Sun and Professor Timothy Rupert for their careful critiques and enthusiastic support of my thesis. Also for letting me use their lab facilities.

I owe special thanks to Dr. Tobias Schaedler, Dr. Alan J. Jacobsen and Dr. William B. Carter of HRL Laboratories for providing me the samples I needed as well as their insightful discussions. Dr. Tobias Schaedler has been a role model to me and helped me envision a successful research path outside academia.

When I came to UCI, I started working with Professor Arash Kheradvar and he recommended me to Professor Valdevit and encouraged me to join his group once he noticed my passion for solid mechanics. I am so thankful for his wise advice; it was my best decision in my adult life.

During my graduate school I was financially supported by Office of Naval Research (Program Manager: D. Shifler, Contract# N000141110884) and National Science Foundation (NSF) under Award # CCMI-1401496. I am thankful for their supports.

I would like to acknowledge Tobias Schaedler, Babak Haghpanah, Scott W. Godfrey, Stephen M. Ryan, Peyman Pourrajab, Stefan T. Szyniszewski, Mazdak Tootkaboni, Jonathan Hopkins, and Lorenzo Valdevit, all of them co-authors of my scientific contributions.

In addition, I want to thank IMRI (LEXI) facilities located in Calit2 building and extend my gratitude to Professor Matt Law and Dr, Jian-Guo Zheng who gave me an opportunity to work as a supervisor of Polytec Vibrometry machine. I am grateful to Polytec Inc specifically Mario Pineda, Jerome Eichenberger, and Eric Lawrence for giving the opportunity to use their PSV 500 system whenever I needed to, and their insightful discussions.

I started graduate school with a little lab experience; Anna Torrent and Kivanc Azgin helped me ramp up in using lab facilities and Scott Godfrey helped me in build up my finite element simulations skills; I am truly thankful to all of them. Moreover, I want to thank our lab post-doctoral researchers in the past five years specifically, Alireza Assadpour, Babak Haghpanah, and Noemi Bonessio for their insightful discussion during my research. Lastly. I would like to thank my lab mates for creating a friendly and joyful environment; Nicolas M. Ruvalcaba, Anna Guell, Bianca Lis Rossi Dias Endo, and Peyman Pourrajab.

When I first came to UC, Irvine, I was new in town without any family or friends. UC, Irvine not only gave me the great professional life but also it was through its amazing community that I found very special people which now are my best friends. They are like my family and they were with me in my sadness and happiness. Thank you Ali Zandi, Ghazal Razeghi, Athena Ahmadi, Behzad Sadjadi for being by my side.

Last but not least, to my family, my mom and dad, thank you for always believing in me and your unconditional love and supports. I want to thank my brother, Hamid, and my sisters, Haleh and Laleh: I am so lucky to have you in my life.

CURRICULUM VITAE

EDUCATION

Ph.D., Mechanical and Aerospace Engineering**,** June 2016
University of California, Irvine, CA
Dissertation Title*: "Ultralight Microlattice Materials with Unique Combination of Stiffness and Damping"*

M.S., Mechanical and Aerospace Engineering, Mar. 2013
University of California, Irvine, CA

B. S., Mechanical Engineering, Aug. 2009
Sh. Bahonar University of Kerman, Iran
Two semesters as guest student at **Sharif University of Technology**, Iran (Sept. 2006- July 2007)
Thesis Title: **"***Exact Three Dimensional Solution of Free Vibration of Thick Rectangular Plates on Pasternak Foundation*"

RESEARCH EXPERIENCE

Graduate Research Assistant, University of California, Irvine Sept. 2011 – June 2016

- Characterized damping and energy dissipation mechanisms in metallic and hybrid microlattice materials using Instron and Laser Doppler Vibrometry (LDV) at micro and macro scales.
- Modeled the damping behavior of metallic and hybrid microlattice materials both analytically and numerically.
- Proposed an optimal design methodology for microlattice materials with exceptional combinations of high stiffness, low density, and high damping.
- Used Python programming language to pre and post processing thousands of FE simulations to find the optimal design or mechanical response map.
- Proposed a non-contact method to measure the Young's modulus of metallic microlattice materials.
- Studied the effects of imperfection in mechanical properties of hollow microlattice materials using statistical analysis and nano computed tomography.

Supervisor and Trainer for Polytec Micro System Analyzer (LDV) Jan. 2012 – June 2016

- Supervised and managed the instrument in the LEXI facility at UC Irvine.
- Trained new users.
- Measured in-plane and out-of-plane vibration of different materials and structures.
- Preformed surface topography and roughness measurements on different structures.

Supervisor and Trainer for INSTRON Jan.2012 – June 2016

TEACHING EXPERIENCE

Teaching Assistant Sept. 2011 – June 2016

- **Mechanics of structure Laboratory** (Fall 2012, Fall 2013, Fall 2014)
  - My duties included: Creating lab instructional material, holding lab sessions for more than 200 students, as well as training junior teaching assistants.
  - Some of the activities I taught in this class are: (1) building data acquisition systems (using basic circuit component and Arduino board) to measure strain gage signals. (2) Measuring stiffness and strength of aluminum bars, loaded in tension and bending using the home-built data acquisition systems.

- **Lightweight Structures** (Winter 2012, Winter 2015)

JOURNAL PUBLICATIONS

B. Haghpanah, **L. Salari-Sharif,** P. Pourrajab, J. Hopkins, L. Valdevit, "Multistable Shape-Reconfigurable Architected Materials", Advanced Materials (2016).

L. Salari-Sharif, T. A. Schaedler, L. Valdevit, "Energy Dissipation Mechanisms in Hollow Metallic Microlattices", Journal of Material Research 29 (2014) 1755-1770.

L. Salari-Sharif, L. Valdevit, "Accurate Stiffness Measurement of Ultralight Hollow Metallic Microlattices by Laser Vibrometry", Journal of Experimental Mechanics 54 (2014) 1491-1495.

L. Salari-Sharif, S.W. Godfrey, M. Tootkaboni, L. Valdevit, "The Effect of Manufacturing Defects on the Compressive Strength of Ultralight Hollow Microlattices*"* Ready for submission.

L. Salari-Sharif, T. A. Schaedler, L. Valdevit, "Damping and Compressive Stiffness of Hybrid Hollow Microlattices: Experimental Characterization, Modeling and Optimal Design*"* Ready for submission.

S. M. Ryan, **L. Salari-Sharif,** S.T. Szyniszewski, L. Valdevit, "Functionally Bonded Woven Micro-lattice Material with Tunable Stiffness and Damping" Under preparation.

CONFERENCE PRESENTATIONS

L. Salari-Sharif, M. Tootkaboni, L. Valdevit, "Statistical Study of Geometric Imperfection in Ultralight Hollow Microlattices*"* MACH Conference, Annapolis, MD (Apr. 2016) Poster Presentation.

B. Haghpanah, P. Pourrajab, **L. Salari-Sharif**, J. Hopkins, L. Valdevit. "Two-dimensional Shape Re-configurable Architected Materials", 11th International Conference on Micro Manufacturing, Orange County, CA (Mar. 2016).

L. Salari-Sharif, T. A. Schaedler, L. Valdevit, "Mechanical Properties of Hybrid Hollow Microlattice Materials*"* MRS Fall Meeting and Exhibition, Boston, MA (Dec. 2015).

L. Salari-Sharif, L. Valdevit, "The Role of Geometrical Defects on the Compressive Strength of Ultralight Hollow Microlattices" MACH Conference, Annapolis, MD (Apr. 2015).

L. Salari-Sharif, L. Valdevit, "Damping Performance of Metallic and Hybrid Microlattices" AmeriMech Symposium on the Dynamic Response of Periodic Materials and Structures, Atlanta, GA (Apr. 2014) Poster Presentation.

L. Salari-Sharif, L. Valdevit, "Damping Characterization of Hollow Metallic Microlattics" Southern California Society for Microscopy and Microanalysis Symposium, UCLA, CA (Mar. 2013).

O.Sarvi, H.Rafeepour, M.hematipour, **L. Salari-Sharif**, "The Analysis of Friction of Slag Transport Caldron's in Mes-e-Sarcheshmeh Co. By ANSYS Software**"** Second National Conference of Manufacturing Engineering (NMEC), Iran (2009).

AWARDS

Nominated as a finalist for the best teaching assistant in Mechanical and Aerospace Engineering department by Engineering Student Council (ESC) (Fall 2014).

Travel award for *AmeriMech Symposium on the Dynamic Response of Periodic Materials and Structures*, Atlanta, GA (Spring 2014).

Fellowship award for women in mechanical engineering (Summer 2012).

Ranked second in GPA in the mechanical engineering department among graduates of 2009, Sh. Bahonar University, Kerman, Iran.

ABSTRACT OF THE DISSERTATION

Ultralight Microlattice Materials with Unique Combination of Stiffness and Damping

By

Ladan Salari Sharif

Doctor of Philosophy in Mechanical and Aerospace Engineering

University of California, Irvine, 2016

Professor Lorenzo Valdevit, Chair

Ultralight hollow microlattice materials offer tremendous potential for energy dissipation, thanks to a unique form of structural damping associated with local buckling of the hollow bars. This dissertation provides a comprehensive study of this damping mechanism and exploits it for the design of hollow microlattices with superior combinations of stiffness and damping at low mass. To encompass a wide design space, both metallic and hybrid (metal/elastomer) hollow microlattices are investigated. This structural damping mechanism is studied in detail and a simple mechanical model is developed and validated by experimental characterization. The model is adopted to optimize the microlattice geometry for maximum values of a damping figure of merit, expressing optimal combinations of high stiffness, low density and high damping coefficient. We find that hollow metallic microlattices exhibit exceptionally large values of this figure of merit; however, this level of performance requires extremely low relative densities (<0.1%), thus limiting the actual amount of energy dissipated.

In order to increase the damping figure of merit at higher densities, hollow microlattices with metal/elastomer/metal sandwich walls are investigated. The sandwich construction provides

increased local buckling strength, thus increasing the amount of energy dissipated by the lattice in a loading cycle. At the same time, the elastomer provides additional energy dissipation through the classic intrinsic constrained-layer damping mechanism, which is active even at relatively high densities and low deformation amplitudes. An analytical model for stiffness and damping (both intrinsic and structural) of hybrid hollow microlattices is derived, and verified via Finite Elements analyses and experimental characterization. Finally, the model is adopted in optimal design studies to identify hybrid microlattices with ideal combinations of the same figure of merit used for metallic lattices. The results indicate that hybrid lattices are clearly superior.

Over the course of this work, significant discrepancies between predicted and measured values of the mechanical properties (e.g., stiffness, strength) of ultralight hollow microlattices were consistently observed. Such discrepancies are attributed to a complex stress state around the hollow nodes and the existence of a variety of manufacturing-induced geometric imperfections (e.g. cracks, non-circularity of the bars). The ultralight nature of the lattices investigated in this study makes them particularly sensitive to these defects. Here, a detailed study of such imperfections is performed with the aim of quantifying their effects on the mechanical performance of the lattices. The results confirm that the major discrepancy between analytical and experimental results can indeed be attributed to manufacturing-induced imperfections.

.

CHAPTER 1. INTRODUCTION

Cellular materials have been heavily investigated over the past decades, by virtue of their low densities and unique mechanical, acoustic, thermal, and electrical properties [1–5]. In particular, these materials are used for their high mechanical efficiency (specific stiffness and strength) [6–9], sound absorption [2] and impact protection [10–13], and have found broad industrial applications, ranging from packaging and impact absorption [14], to filtration [15], tissue engineering [16], heat dissipation and heat exchange [17, 18].

When fabricated with open cell topology, cellular metals provide exceptional potential for multi-functionality. An example is a sandwich structure with a cellular core offering unique combinations of mechanical properties (specific stiffness and strength) and thermal properties (heat transfer by active cooling [19, 20]). These attractive properties can be further enhanced if cellular materials are carefully architected to possess an ordered *periodic* geometry rather than a stochastic arrangement of matter. A careful topological design of the architecture enables a precise control on property variations from macro-scale to the unit-cell scale, resulting in order-of-magnitude improvements on specific stiffness and strength, among other properties [6, 8]. Importantly, the periodic nature of topologically designed cellular materials enabled a large-body of optimization studies, with an emphasis on specific strength [7–9], active cooling [18], and protection from high-velocity impact [11]. A classic example of periodic cellular materials are lattices, where solid or hollow bars are joined at nodes to form two or three-dimensional unit cells that can be repeated to fill the space. Recently, multi-scale numerical models have been developed to characterize the deformation behavior, stiffness, yield strength, and buckling strength of macro-scale components made up of lattice materials of different topologies [21–23]. These models have

been used to optimally design lattice materials for specific engineering systems (e.g., bone implants [24]). Although most models are linear and assume infinitesimal deformations, some recent examples have been extended to the non-linear deformation regime [25].

When loaded by external compression, typical cellular metals (whether stochastic or periodic) exhibit a stiff linear response, followed by plastic deformation: the plastic regime results in a stress plateau that remains fairly flat all the way to the densification strain, $\varepsilon_d \sim 1-\bar{\rho}$, with $\bar{\rho}$ being the relative density of the material. Upon unloading, only the elastic portion of the deformation is recovered, which is often significantly smaller than ε_d. This behavior makes sandwich structures with cellular metallic cores particularly suitable for impact and blast mitigation [10, 12, 26–28]. The challenge is designing a suitable cellular core with compressive strength low enough to guarantee force protection, and maximum energy dissipation per unit volume upon densification [29]. The minimum thickness of the core necessary to guarantee impact protection depends on the magnitude of the transmitted impulse and the allowable level of stress transfer to the protected structure. Unfortunately, maintaining the plateau stress low enough to ensure force protection requires unreasonably thick panels [30]. Even when an appropriate thickness can be selected, substantial vibration and transmission can be detrimental to delicate electronics and personnel.

Such vibrations can be isolated by various methods, which can be categorized in two approaches: (1) passive isolation [31], e.g., provided by pneumatic or air isolators [32], mechanical spring-dampers [33], pads or sheets of flexible materials such as elastomers [34], rubbers [35], corks, laminate materials [36], and structures incorporating negative stiffness elements [37]; and (2) active isolation [38, 39], e.g. provided by piezoelectric polymer actuators [40]. All these mechanisms significantly increase the weight and complexity of the system.

Integrating high specific stiffness and strength, impact and blast protection, and vibration isolation into a single cellular structure could result in potentially dramatic weight savings for a variety of engineering systems [41] (Figure 1.1).

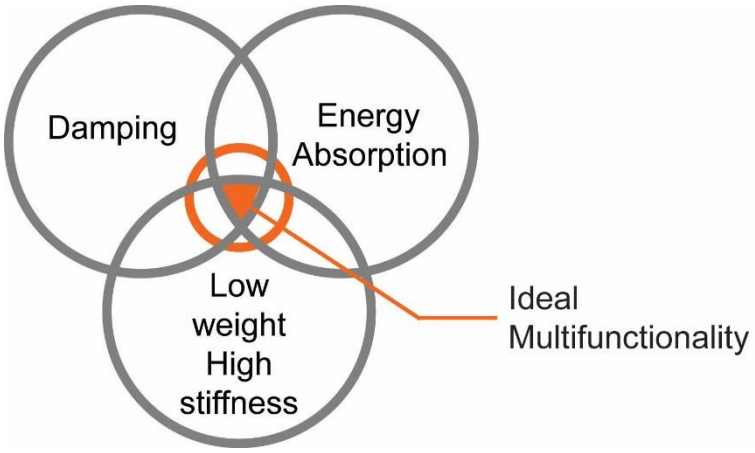

Figure 1.1 Multifunctional cellular core with ideal combinations of low weight, high stiffness, high energy absorption and high damping performance.

Cellular materials have been widely used for vibration isolation in the past decades [1, 42, 43]. The loss coefficient of stochastic cellular materials, η, scales with the loss coefficient of their constituent materials over the relative density of the cellular material ($\eta \approx \eta_s / \bar{\rho}$) [1], effectively limiting the amount of damping that can be achieved by these materials. However, damping in cellular materials can be enhanced by using carefully selected periodic unit cell architectures, incorporating intrinsically dissipative elements (e.g., elastomers) [44] or negative stiffness sub-components [45, 46].

A comprehensive study by Evans et. al. [10] on foams, honeycombs, and hollow-truss based lattices revealed that hollow-truss based lattices exhibit superior impact resistance. The lattices in that study were fabricated with a process developed at HRL Laboratories (Malibu, CA). The general process consists of three steps: (i) fabrication of a polymeric template by a self-propagating photopolymer waveguide process (SPPW) [47, 48]; (ii) coating of the template with

a metallic thin film (or multiple films) by suitable deposition processes; (iii) removal of the polymeric template by chemical etching, thus resulting in a hollow metallic or hybrid cellular materials, as schematically depicted in Figure 1.2. This process is very scalable, and it allows a range of bar diameters from ~50 microns to many millimeters. Pushing the diameter to its lower bound allows fabrication of structurally robust hollow lattices with walls as thin as a few hundred nanometers. As explained below, this allows deposition of films with very small grain size, and hence exceptionally high yield strength [19, 49].

When designed with a density of ~8%, those lattices were proven to be near-optimal for blast protection [29]. Remarkably, as explained below, the very same lattices, designed at a density of ~0.1%, possess unusually high vibration damping compared to any other metallic system [50]. Furthermore, hollow lattices possess among the highest specific stiffness and strength among any cellular material [51]. The implication is that optimally designed cellular cores with hollow-truss-based lattices might provide unique combinations of low weight, high stiffness, impact resistance and vibration damping. Such architected materials are investigated in this dissertation.

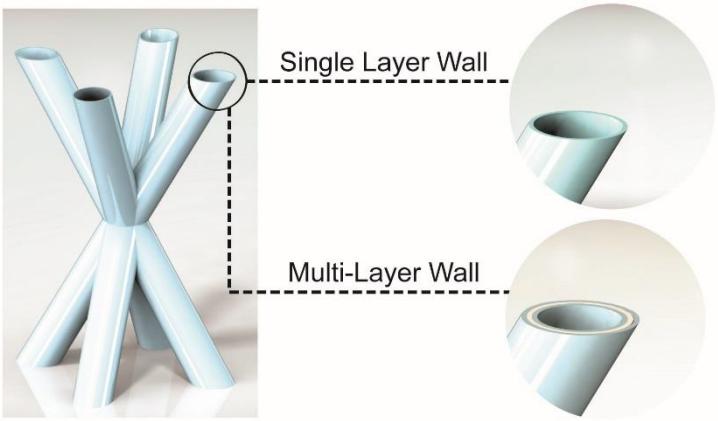

Figure 1.2 Unit cell schematic of an octahedral lattice that can be manufactured by the SPPW technique with two possible wall designs: metallic (containing a single layer of metal) or hybrid (containing two metal layers sandwiching a polymer layer).

The mechanical response of hollow nickel microlattices to external uniaxial compression has been previously investigated experimentally [52], and models for stiffness and strength have been proposed and adopted for optimal design studies [53, 54]. A key feature of these metallic systems is that the compressive behavior under large strain is strongly dependent on the relative density of the lattice: while high-density (~1-10%) lattices deform by plastic hinging of the nodes, resulting in an irrecoverable plastic deformation as illustrated in Figure 1.3a (similarly to conventional cellular metals, as discussed above), lattices with density lower than ~0.1% deform by local buckling and/or partial node fracture followed by large rotation of the truss members, resulting in a nearly flat stress plateau from which the material can fully recover after compressive strains in excess of 50% (see Figure 1.3b).

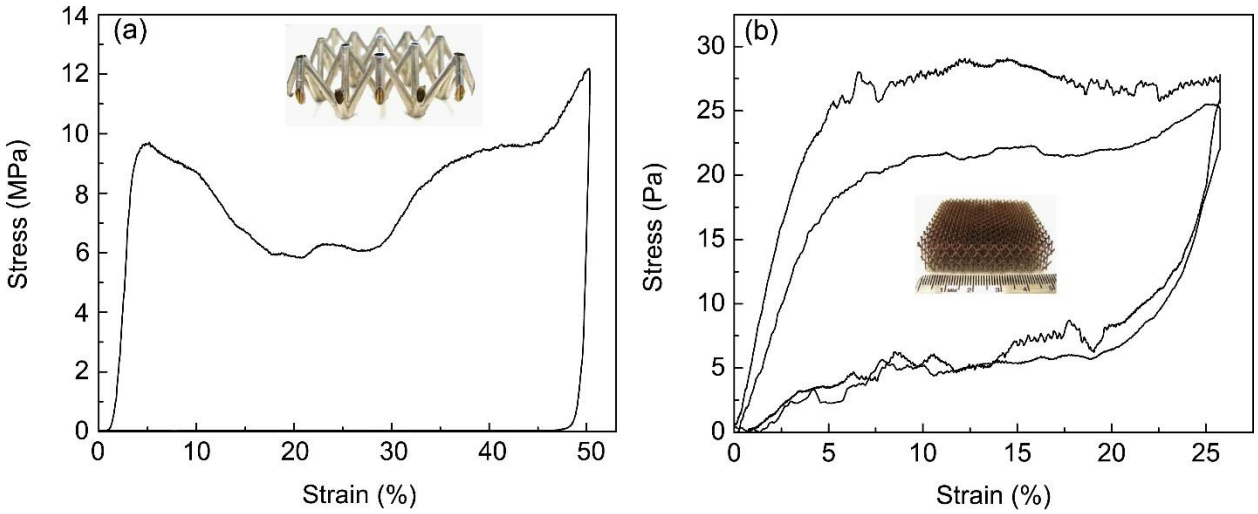

Figure 1.3 Compressive response of microlattices at (a) wall thickness t=26μm and relative density $\bar{\rho} = 8.45\%$;and (b) wall thickness t=150nm and relative density of $\bar{\rho} = 0.01\%$.

The transition between these two regimes has been investigated in detail in [52], and at first order depends on a single geometric parameter of the lattice, a critical wall thickness-to-diameter ratio, $(t/D)_{cr}$:

$$\left(\frac{t}{D}\right)_{cr} = \frac{\sigma_{y,s}}{E_s}\frac{0.25}{\theta - \sin^{-1}[(1-\varepsilon_{\max})\sin\theta]} \tag{1.1}$$

where $\sigma_{y,s}$ is the yield strength of the wall material, E_s its Young's modulus, $\varepsilon_{\max}$ is the maximum compressive strain, and θ is the angle that the lattice bars make with the horizontal plane. For $t/D < (t/\mathrm{D})_{cr}$, individual truss members can locally buckle or partially fracture close the their conjunctions (nodes) and subsequently undergo large rotations without plastic deformation up to a macroscopic strain, $\varepsilon_{\max}$. This simple equation (Eq.(1.1)) has been shown to capture the transition for hollow lattices made with a variety of film materials [55]. From Eq.(1.1), it is evident that the recovery from large compressive strains requires a very high yield strain of the constituent material and very low truss member aspect ratios, both of which are uniquely enabled by the three-step fabrication process described above (the former by using very thin and strong nanocrystalline nickel films and the latter by careful chemical etching of the polymeric preform). This explains why this behavior was never observed before in cellular metals. Although the mechanism for recovery is well understood, the physical mechanisms for energy loss upon cycling are still elusive, and will be thoroughly investigated in this thesis.

A qualitatively similar compressive response (exhibiting exceptional elastic recovery and energy dissipation) has been recently documented in a number of multiscale material systems, for example forests of carbon nanotubes in thin-film form [56] and ultralight boron nitride foams [57]. The mechanism for recovery is similar in all of these cases: elastic instabilities in discrete members enable large rotations of members relative to each other without the introduction of irrecoverable plastic strain. Franternali et al. [58] modeled the recovery and damping behavior of carbon nanotube forests using a bi-stable spring model. Moreover, in recent years, a number of studies have introduced materials that are capable of achieving stable geometrical changes using the

concept of bi-stable negative stiffness elements [45, 46, 59, 60]. These designs generally require elastomeric constituents with very large yielding or fracture strain in order to achieve the required reconfigurable behavior without material failure. This results in shape reconfigurable materials with fairly low strength and limited energy absorption capabilities.

A unique characteristic of hollow microlattices (in contrast with nanotube films and foams) is that the geometric parameters can be carefully chosen to meet a desired performance metric, thus providing an excellent platform for optimal design. However, this unique energy dissipation mechanism is only applicable to ultralight lattices ($\bar{\rho} < 0.1\%$). In order to design higher density lattices with exceptional combinations of specific stiffness, damping and energy absorption, alternative damping mechanisms must be sought. A possible way to achieve this combination is the use of lattices with hybrid (sandwich) walls, where two metallic layers enclose a lossy polymeric film (Figure 1.2). When the hybrid lattice is compressed, the lossy layer deforms (primarily in shear), dissipating energy. This approach is akin to the classic constrained-layer damping, widely exploited in flat aircraft structure design [35, 61]. Moreover, the metallic films increase stiffness and strength, potentially resulting in higher values of structural damping. This intrinsic damping can emerge as the main damping mechanism in lattices of high relative density or it can appear in tandem with the structural damping mechanism discussed above (albeit, exclusively in ultralight lattices). These two mechanisms in hybrid hollow microlattices will be characterized, modeled and demonstrated in this thesis.

Previous studies on strength and stiffness analysis of metallic microlattices produced with this technique [53, 54] have shown that the experimentally measured stiffness and strength are always significantly lower than predicted by analytical and numerical models, thus compromising the reliability of the optimal design studies based on these models (including those presented in

this thesis). Incidentally, similar discrepancies were observed in other 3D micro/nano-lattices with the polymeric preform manufactured by different techniques, such as projection microstereolithography [51], and two-photon lithography 3D direct laser writing (3D-DLW) [62], [63]. In all these works, this large discrepancy is generally attributed to the complex stress state around the nodes (not predicted by simple models) and the presence of manufacturing-induced geometric imperfections. Note that due to the buckling dominated [53] nature of ultralight samples, the effects of defects can be even more significant in ultralight samples compared to denser counterparts. Wallach [64] performed a sensitivity analysis on the 3D solid truss lattices, where imperfections were artificially introduced (by randomly removing bars from structure) to quantify their effect on stiffness and strength. However, to the best of our knowledge, no work has been performed to quantify the magnitude of defects naturally introduced by the manufacturing process in hollow lattices, and their quantitative effect on mechanical properties.

In this dissertation, such an analysis is provided for hollow microlattices produced with the three-step process described above. Although the shape and size of the defects are specific to this manufacturing approach, the methodology presented here is entirely general and applicable to all architected materials.

To summarize, this research aims to develop a lightweight lattice-based cellular material with optimal combinations of stiffness, strength and vibration damping. This objective will be reached by addressing the following fundamental research challenges:

- Developing a physics-based understanding of the multi-scale mechanisms that lead to damping in metallic ultralight lattice-based cellular materials, and incorporating it in optimal design tools to identify the best architecture for combined specific stiffness and damping.

- Developing a physics-based understanding of the multi-scale mechanisms that lead to damping in hybrid lattice-based cellular materials, and incorporating it in optimal design tools to identify the best architecture for combined specific stiffness and damping.
- Developing a methodology to rigorously describe manufacturing imperfections in ultralight metallic microlattices and quantify their effect on the lattice strength, with the aim of ultimately improving the reliability of analytical/numerical models and the optimal design studies that are based on such models.

CHAPTER 2. APPROACH

To achieve the objectives of the research in an efficient and feasible manner, a methodology needs to be determined. The following tasks are developed to address each of the objectives defined in the previous chapter, individually.

Task 1: *Developing a physics-based understanding of the multi-scale mechanisms that lead to damping in metallic ultralight lattice-based cellular materials, and incorporating it in optimal design tools to identify the best architecture for combined specific stiffness and damping.*

As the first step in Task 1, an extensive literature review is performed on cellular materials in general and microlattice structures in particular. Importantly, advantages and disadvantages of the SPPW fabrication process are investigated. This fabrication process is discussed in detail in chapter 3.

A quantitative assessment of energy loss under cycling compression and harmonic excitation of ultralight metallic lattices is performed, to separate and quantify several energy loss mechanisms that can potentially be responsible for the unique damping characteristics of hollow microlattices. A structural damping mechanism based on local buckling of the hollow bars is identified as the key contributor to the energy loss, and an analytical model is suggested to relate the amount of energy loss by this mechanism to the geometric features of the lattice. The accuracy of the model is validated by experimental results and finite element simulations. Finally, optimal geometries are identified based on the model, for maximum values of a damping figure of merit. This figure of merit incorporates the product of two terms: (i) $E^{1/3}/\rho$ with E the Young's modulus and ρ the density of the microlattice, and (ii) the damping coefficient (Ψ). The modeling and optimization procedures are discussed in detail in chapter 5.

In order to calculate the figure of merit, an accurate estimate of the Young's modulus of the ultralight lattices is required. Experimental validation of this model in turns requires accurate measurement of the Young's modulus. The challenges associated with measuring stiffness of ultralight buckling-dominated lattice structures are discussed in detail in chapter 4, where a novel approach is proposed.

Task 2: *Developing a physics-based understanding of the multi-scale mechanisms that lead to damping in hybrid lattice-based cellular materials, and incorporating it in optimal design tools to identify the best architecture for combined specific stiffness and damping.*

The investigation performed in Task 1 reveals that the unique structural damping mechanism discussed above is only present in hollow microlattices with a relative density $\bar{\rho} < 0.1\%$, which limits the total amount of energy dissipation in these architected materials. An alternative mechanism is proposed in chapter 6 to increase the amount of damping coefficient in microlattice materials. In this design, the hollow lattice is fabricated with the wall consisting of two metallic layers enclosing a lossy polymeric film. The specific design increases damping of microlattices by taking advantage of the constrained-layer damping mechanism, while the metallic layers provide stiffness.

We formulate an analytical model for both intrinsic (constrained-layer) and structural (buckling-induced) damping mechanisms of hybrid microlattice materials, followed by numerical validation and experimental verification with the overarching goal of designing lattices with unique combinations of high stiffness, high damping, and low density. Finally, the analytical models are adopted for optimal design studies. In order to assess the effectiveness of this approach, the performance of hybrid microlattices is compared to that of the metallic microlattices discussed in Chapter 5. The details of modeling, experiments and optimization are presented in chapter 6.

Task 3: *Developing a methodology to rigorously describe manufacturing imperfections in ultralight metallic microlattices and quantify their effect on the lattice strength, with the aim of ultimately improving the reliability of analytical/numerical models and the optimal design studies that are based on such models*.

Nearly any published study on the modeling of mechanical response of hollow microlattice materials have shown severe discrepancies between the analytical models and the experimental data. These discrepancies are usually explained by geometric imperfections of the structure. Hence, clear understanding and quantifying the defects in microlattices is essential to minimize the imperfections during the manufacturing process.

In particular, we study the effects of geometric defects on the strength of ultralight hollow microlattices. The geometric defects at the individual strut level are investigated and finite elements (FE) simulations based on Nano-CT scan data are used to investigate the buckling strength of a single bar in a hollow microlattice, from which an indication of the imperfect lattice strength can be obtained. Subsequently, statistical analysis is performed on the imperfection data gathered from Nano-CT scanning of a number of single bars within a metallic microlattice to identify the dominant imperfection modes and build a probabilistic representation that is used to generate thousands of statistically significant samples of imperfect bars. These imperfect samples are used for the statistical analysis of the effects of imperfect geometry over the strength variation in a sample. The detailed study on geometric imperfections is explained in chapter 7.

CHAPTER 3. FABRICATION PROCESS

In order to better understand the damping and energy dissipation mechanisms of hollow microlattice materials, an adequate explanation of the manufacturing process of such materials is necessary. In this chapter, we look into manufacturing process of hollow nickel microlattices and hollow hybrid microlattices in detail.

3.1 Hollow Nickel Microlattices

The nickel microlattice materials are fabricated at HRL Laboratories (Malibu, CA), with the following three-step process (schematically illustrated in Figure 3.1): (i) fabrication of a polymeric template by a self-propagating photopolymer waveguide process (SPPW) [48, 50, 65]; (ii) coating of the template with a thin film by a suitable deposition process (e.g., electroless nickel plating using commercially available process; OM Group Inc., Cleveland, OH; and/or electroplating); (iii) removal of the polymeric template by chemical etching.

In the first step, the polymer microlattice templates are fabricated by exposing a thiol-ene liquid photomonomer to collimated ultraviolet (UV) light through a patterned mask at different angles. When UV light reaches the thiol-ene liquid, it creates a periodic array of tubes, and when the UV beams intersect with each other, they create nodes, hence forming an octahedral unitcell. This polymeric waveguide formation process happens in few seconds, making this technique significantly faster and more scalable than any competing technology. A wide range of architectures can be fabricated by changing the mask pattern and the angle of the UV light rays. The polymeric lattices are then used as a template for depositing the structural film. Different materials can be deposited on top of the polymeric sample (e.g. nickel, copper, gold, etc.) [55].

To prepare the surface for electroless deposition, the samples are first dipped in an aqueous solution of potassium permanganate and sodium hydroxide, then palladium catalyst is deposited by immersion in activator solution containing hydrochloric acid and tin(II) chloride (Fidelity 1018, OM Group Inc.), followed by an etch in accelerator solution containing fluoboric acid (Fidelity 1019, OM Group Inc.). The samples are then dipped in electroless nickel plating solution with nickel sulfate as nickel source, sodium hypophosphite as reducing agent, and sodium malate and acetic acid as complexing agents (9026M, OM Group Inc.). The electroless nickel plating bath is kept at pH 4.9 by addition of ammonium hydroxide and plating is performed at 80ºC. For electroless nickel samples, the plating time is adjusted to achieve the desired coating thickness. A wall thickness *t* of 500 nm is achieved by electroless nickel plating of approximately 3 minutes. The electroless deposition is limited to 3 micron wall thickness. For thicker walls, an electroplating process can be used. Note that the chemical compositions of electroless (Ni-P) and electroplating (pure Ni) nickel are different. The nickel samples which were studied in this work were are prepared by electroless deposition.

After deposition of the wall material, the top and bottom edges of the sample are sanded to expose the underlying polymer at each node. Finally, the polymeric template is etched out by using a chemical solution (3M NaoH at 60°) for 24hrs, resulting in a hollow tube microlattice sample. Samples produce with this technique can span up to three orders of magnitude in relative density (0.01%-14%), depending on the choice of the geometric parameters (wall thickness, diameter, bar angles, etc…)

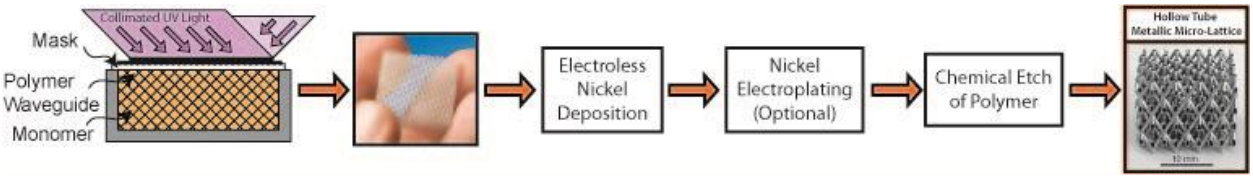

Figure 3.1 Schematic of the SPPW fabrication process for nickel hollow microlattice materials.

This process was used to generate hollow lattices with the octahedral topology shown in Figure 3.2, where ℓ denotes the length of each bar, D its diameter, t its wall thickness, and θ the angle between the diagonal bars and the horizontal plane.

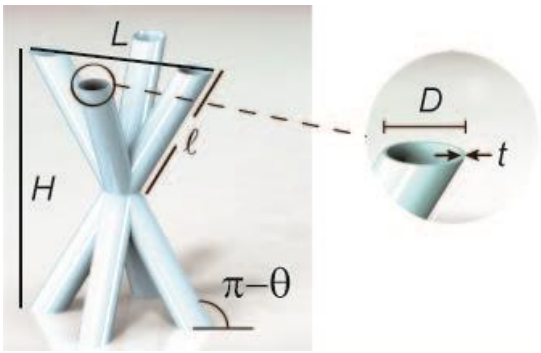

Figure 3.2 Unit cell topology and definition of dimensional parameters for hollow microlattices.

The mechanical properties of the base nickel layer have been previously measured [50, 52]. The electroless nickel layer has density of $\rho = 8900 kg/m^3$, a Young's modulus of $E = 210\text{GPa}$, and a yield strength of $\sigma_y = 2.5\text{GPa}$. This exceptional strength is entirely due to its fine nanocrystalline grain size, a direct result of the electroless thin film deposition process.

3.2 Hollow Hybrid Microlattices

The hybrid hollow microlattice materials are fabricated with a slight variation of the process described in sec. 3.1 (schematically illustrated in Figure 3.3): (i) fabrication of a polymeric template by a self-propagating photopolymer waveguide process (SPPW) [48, 50, 65]; (ii) coating of the template with a film of metal by a suitable deposition process (e.g., electroless and/or electroplating); (iii) coating of the resulting metal layer with a film of polymer by a suitable deposition process; (iv) coating of the resulting polymeric layer with a film of metal by using a

suitable deposition technique (electroless or electroplating); (v) removal of the inner polymeric template by chemical etching.

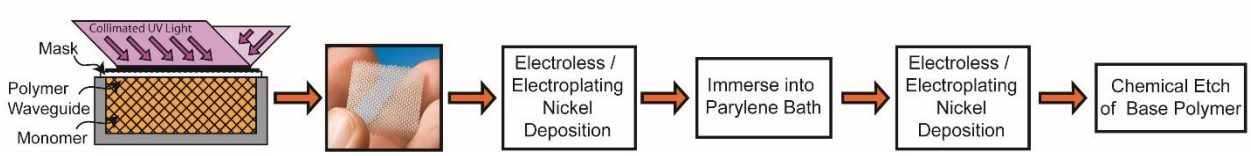

Figure 3.3 Schematic of the SPPW fabrication process for hybrid hollow microlattice materials.

Polymeric templates coated in nanocrystalline nickel by electroless deposition are produced as described in sec. 3.2 (steps (i)-(ii)). In order to deposit the polymer on top of the first metal layer, the lattices are immersed into a polymeric bath for few seconds. Although a variety of polymers can be applied, parylene is chosen for this study due to its combination of high damping and stiffness. Subsequently, another layer of metal is deposited on top of the polymeric layer. Finally, the top and bottom of the samples are sanded to expose the underlying base polymer at each node. The polymeric base template is etched out by using a chemical solution (3M NaOH at 60°) for 24hrs (the solution must be chosen in a way to remove only the base inner polymeric template and not the polymer in the constrained-layer), resulting in hybrid hollow tube microlattices.

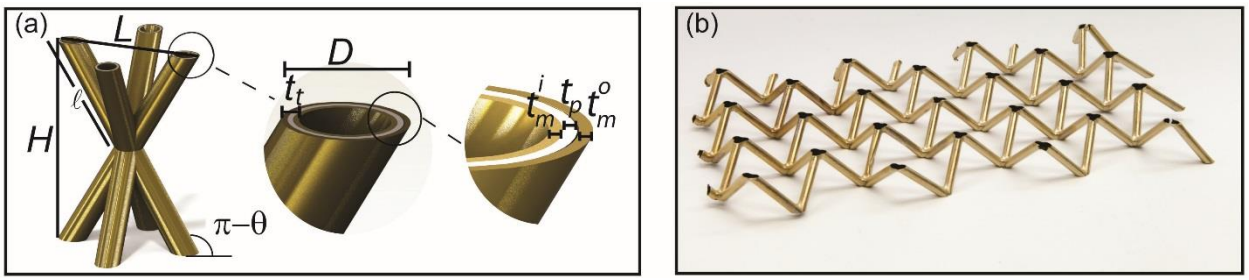

Figure 3.4 (a) Octahedral unit cell topology and defining dimensional parameters for hybrid hollow microlattices. (b) A tetrahedral hybrid hollow microlattice manufactured by HRL laboratories.

The discussed process results in hybrid hollow microlattices consisting of periodic octahedral unit cells shown in Figure 3.4a, which is built of bars with length ℓ, diameter D, inner layer metal wall thickness t_m^i, polymer wall thickness t_p, outer layer metal wall thickness t_m^o, and truss angle θ. Figure 3.4b shows a half-layer tetrahedral hybrid lattice. Thanks to the large scale of this sample, the truss angle, length, and diameter of the lattice can be readily measured with a Dino Digital microscope. This lattice contains bars with a length of $\ell = 22.4\text{mm}$, diameter of $D = 3.2\text{mm}$, and truss angle of $\theta = 47^\circ$. (Figure 3.5a). The wall thickness of the three different layers was measured by scanning electron microscopy (SEM) of one bar. The bar was extracted from the lattice and fixed in epoxy resin. The epoxy is sanded with various roughness sand paper (the softest one was $1\mu\text{m}$ sand paper) to achieve a uniform cross section. During the whole process the sand wheel was perpendicular to the bar. The thickness of three different layers of the bar was carefully measured by SEM. The inner and outer nickel layer appears to be pretty uniform with an average thickness of $t_m^i = 19.5\mu\text{m}$ and $t_m^o = 15.1\mu\text{m}$, however, the thickness of the parylene layer is non-uniform and varies between $t_p = 1.5\mu\text{m}$ to $t_p = 31\mu\text{m}$ (Figure 3.5b and c). Electroplating or electroless nickel plating result in conformal coatings with a uniform thickness that can be controlled by the plating time. However, the polymer layer is coated by immersing the lattice into a polymeric bath for a few seconds. Therefore, the thickness varies a lot according to the angle of resting orientation. Gravity is the main factor in the thickness of polymer which results in very non-uniform polymeric layer. Note that this is only one cross section of a single bar in the lattice, hence, this variation can be even larger in the whole structure.

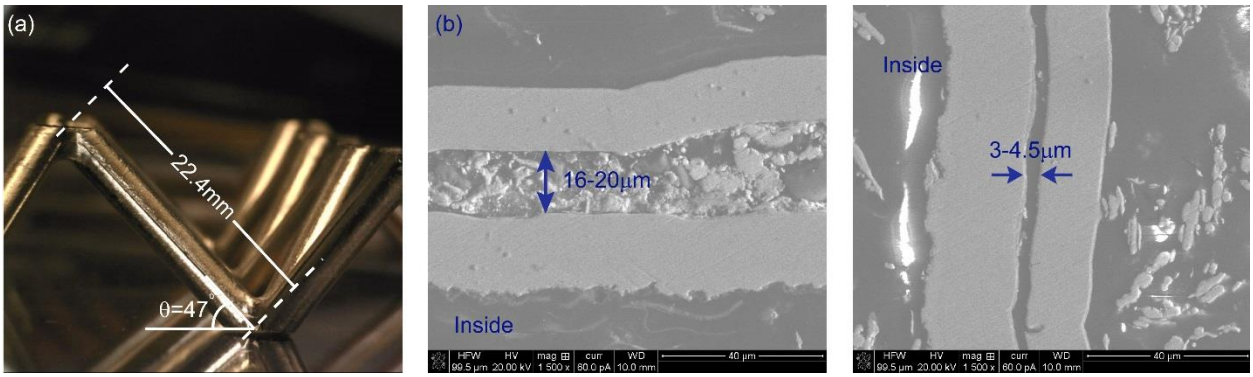

Figure 3.5 (a) Bar length and angle measurements of hybrid hollow microlattices via a Dino Digital microscope; (b) and (c) variations in polymer layer thickness of hybrid hollow microlattices measured via SEM at different locations in a single cross section of a single bar.

The mechanical properties of the base nickel and parylene layer were measured at HRL laboratories. The nickel layer has a density of $\rho = 8900\text{kg/m}^3$, a Young's modulus of $E = 165.8\text{GPa}$, and a yield strength of $\sigma_y = 607.2\text{MPa}$, whereas the parylene layer has a density of $\rho = 1040\text{kg/m}^3$, a Young's modulus of $E = 1.4\text{GPa}$, and a damping coefficient of $\tan\delta = 0.25$.

CHAPTER 4. STIFFNESS MEASUREMENTS OF ULTRALIGHT HOLLOW METALLIC MICROLATTICES

Previous studies on microlattice materials [54] show that measuring the compressive stiffness of these ultralight lattices with conventional contact techniques presents a major challenge, as the lattice bars buckle or locally fracture immediately after contact with the loading platens is established, with associated reduction in stiffness. Therefore, a novel technique is needed to capture the stiffness of these lattices accurately. Non-contact resonant approaches have been successfully used in the past for modulus measurements in solid materials, at both small [66–69] and large scales [70–72]. In this research we demonstrate that Laser Doppler Vibrometry [73, 74] coupled with Finite Elements Analysis (FE) is a suitable technique for the reliable extraction of the Young's modulus in ultralight microlattices. The experimental methodology is explained in detail in section 4.1. The finite element model used to extract the Young's modulus of the lattice from the experimental data is described in section 4.2. The results are compared with those obtained with conventional uniaxial compression tests, and the accuracy of this method is validated by FE simulations of microlattice unit cells in sec. 4.3. The summary of this chapter is available in [75].

4.1 Experimental Approach

Ultralight nickel hollow microlattices (Figure 4.1) were fabricated as described in chapter 3, and glued to carbon/epoxy face sheets using Epoxi-Patch Adhesive glue, resulting in a sandwich configuration. The planar face sheets are essential for reliable laser surface tracking. All sample dimensions are reported in Table 4.1. All vibrometry measurements were performed with a Polytec

Micro Systems Analyzer (MSA-500), a fully integrated structural dynamics system. This instrument enables real-time, non-contact in-plane and out-of-plane vibration analysis (only the latter is used in this work). From the detection of resonant frequencies, the effective Young's modulus, *E*, of the sample in the direction normal to the face sheets can be obtained by close-form analytical solutions or fitting to Finite Elements models.

To verify the accuracy of this approach, an aluminum cantilever bar (E=69GPa) was excited acoustically and the first two resonant modes were measured at 409 kHz and 2,560 kHz. The Young's modulus, *E*, was extracted from the analytical expression of the resonant frequency of each mode *n*, $f_{(n)} = \frac{\alpha_{(n)}^2}{2\pi}\sqrt{\frac{EI}{\rho A L^4}}$, where *I*, *A* and *L* are the moment of inertia, the area and the length of the beam, respectively, ρ is the density of the material, and $a_{(1)} = 1.875$ and $a_{(2)} = 4.694$ ($a_{(n)} = k_{(n)}L$, with $k_{(n)}$ the wave number associated to the nth vibration mode) [76]. The modulus extracted from the first two modes was $E = 68.6\text{GPa}$ and $E = 68.4\text{GPa}$, respectively. The consistency between the two measurements and the agreement with the known value for aluminum demonstrate the robustness of the approach.

The microlattice sandwich samples were mounted on a piezoelectric actuator with a travel range of 15μm. The actuator excited the sample from one side in the direction normal to the face sheet; the actuation was sinusoidal, with frequency swept in the 0-4 kHz range. The velocity of the opposite face sheet along the same direction was measured by scanning laser vibrometry. Multiple points on the face sheet were scanned, to capture the three-dimensional movement of the sample (and hence enable the identification of the different modes). The instrument and the test configuration are shown in the inset in Figure 4.1.

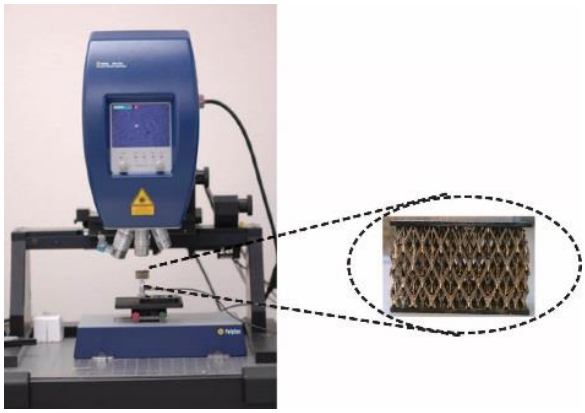

Figure 4.1 The experimental setup, Laser Doppler Vibrometry, and microlattice core with facesheets.

The Response of sample C (Table 4.1) is shown in Figure 4.2. For this sample, two eigenmodes were detected within the excitation range at 1,746 Hz and 2,302 Hz.

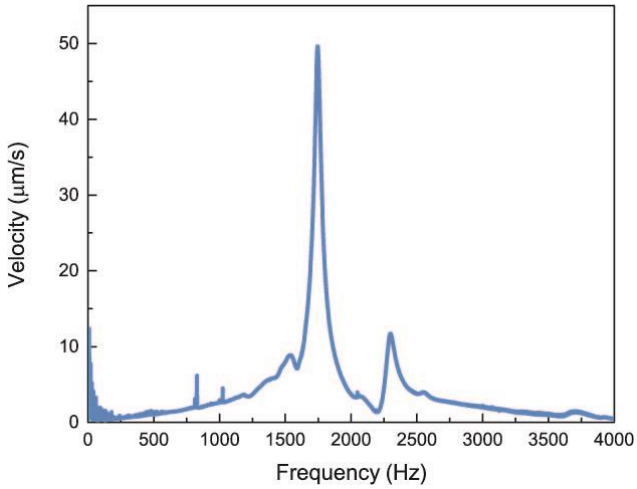

Figure 4.2 Frequency response of a sandwich panel with ultralight micro-lattice core, captured by Laser Doppler Vibrometry.

Table 4.1 Summary of dimensions and properties of tested microlattices and facessheets mass (thickness of facessheets=0.78mm)

Sample	Wall Thickness t(μm)	Strut Diameter D(μm)	Strut Length L(μm)	Strut Angle(°)	Thickness/ Diameter	Density (Kg/m^3)	Relative Density (%)	Face sheet Mass (mgr)	The Core to Face sheet Mass Ratio
A	1±0.1	560±30	4600±120	60±2	(1.8±0.3)E-3	7.66±0.7	0.086±0.01	500	9.8
B	0.53±0.06	460±20	1743±36	55±2	(1.1±0.2)E-3	8.82±0.8	0.09±0.01	475	10.5
C	1.2±0.12	560±30	4600±120	60±2	(2.1±0.4)E-3	10.05±1	0.11±0.02	475	8
D	0.56±0.03	115±9	1050±32	60±2	(4.8±0.6)E-3	18.22±1.8	0.21±0.03	283	11.3
E	4±0.4	430±15	4000±120	60±2	(9.3±0.7)E-3	28.95±2.9	0.33±0.04	334	4

4.2 Young's Modulus Calculation

Finite element simulations were performed in ABAQUS to extract the relation between the Young's modulus and the natural frequencies. The sample was modeled as an effective isotropic solid core within two perfectly bonded face sheets. The density of the core was determined by weighing the microlattice sample and dividing the mass by the bounding volume.

As the Poisson's ratio, ν, of these lattices is difficult to measure, selected Finite Elements simulations were performed with ν=0 and ν=0.5. For all cases, the difference in the natural frequencies was ~ 10%, inducing a change in the predicted Young's modulus of less than 12%, and hence generally negligible. Consequently, a Poisson's ratio of 0.3 for the core was assumed for all subsequent calculations.

The effective Young's modulus of the solid core was swept within a reasonable range, chosen based on analytical estimates according to the sample density [54]. The six lowest vibration modes and corresponding eigenfrequencies were obtained via eigenvalue extraction. The effect of the Young's modulus of the core on the natural frequencies for the first six modes is depicted in Figure 4.3b. The first and second modes involve primarily shear motion in the xy plane, along the x and y directions, respectively (z being the out-of-plane axis for the sandwich configuration); as the z-motion is negligible, they are generally undetectable with z-direction actuation/detection. The third mode is a twist about the z-axis, and does not contain any z-component of displacement; as such, it is undetectable with out-of-plane vibrometry and is not included in the figure. The fourth mode is the classic extensional mode. Finally, the fifth and sixth modes are combination of extensional and bending modes about the X and Y axes, with displacement primarily in the z-direction. In the experiments, these two modes appeared combined, as indicated by the X and Y

components of the rotation axis of the top face sheet (see inset in Figure 4.3a). Hence, an average curve was added to the numerical results (dotted line in Figure 4.3b).

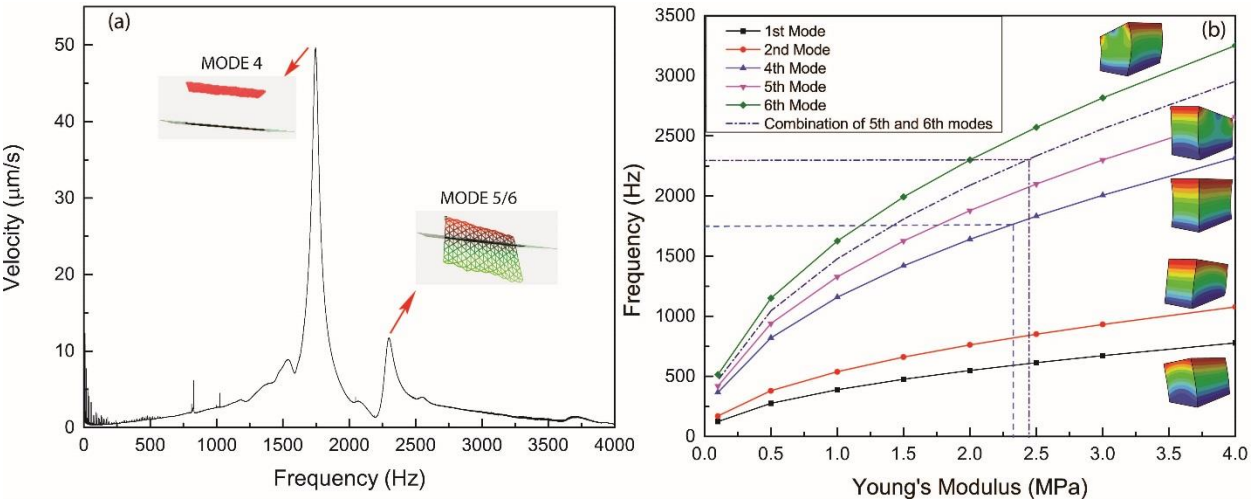

Figure 4.3 (a) Frequency response of a sandwich panel with ultralight micro-lattice core, captured by Laser Doppler Vibrometry. The mode shapes are displayed. (b) Natural frequencies of a sandwich panel with homogenized core, as a function of the Young's modulus of the core (from Finite Elements analysis). The mode 4 peak in (a) can be used in (b) to extract the modulus E_z of the core.

It is important to notice that the microlattices under consideration are orthotropic. If the x and y directions are equivalent, six elastic constants would be needed to fully characterize the elastic response of the material. As the presence of the face sheets (essential for optical detection) and the single-axis detection limit the number of modes that can be observed, fitting the entire elastic tensor to the observed peaks presents significant challenges. For the sake of simplicity, here we concern ourselves with the determination of the Young's modulus in the z direction (which is one of the critical engineering properties for lattice materials). For a more rigorous extension of this technique to orthotropic architected materials, see Appendix A.

As the fourth mode depends almost exclusively on E_z, its detection and identification allows extraction of the modulus. Once E_z is extracted, the modeling/experiment agreement on the frequency of other detected modes provides some information on the deviation from isotropy. For

the sample depicted in Figure 4.3b (Sample C in Table 4.1), the modulus E_z extracted from the experimentally measured mode 4 frequency (Figure 4.3a) is 2.3MPa. As modes 5 and 6 also depend almost exclusively on E_z, a fitting from the mode 5/6 peak would result in a modulus prediction that is fairly similar (~7% larger). Fitting on higher modes that involve other elastic moduli would obviously not provide realistic results, unless the lattice under investigation was isotropic. In conclusion, this approach provides a simple methodology to calculate the modulus in a single direction via a non-contact technique that allows detection and identification of the suitable mode (mode 4) or combination of modes.

4.3 Comparison with Uniaxial Compression Measurements and Finite Element Simulations

The Young's modulus of micro-lattice materials extracted with this technique is compared to FE and experimental results previously published [54] (Figure 4.5). All samples exhibit relative density between 0.08% and 0.32%. All FE simulations were performed on single unit cells, meshed with a dedicated geometry modeling code [53, 54] (Figure 4.4). Notice that these FE analyses are very different from those used for the extraction of the Young's modulus of the lattice (Figure 4.3b): while those were solid models of an effective cellular medium, in this case a single unit cell of the truss lattice is meshed with shell elements. Two different boundary conditions were used: fully periodic BCs, and free-edge BCs. In the latter, no translational or rotational constraint is imposed along the sides of the unit cell [54], simulating a deformation process where each cell is only minimally constrained by the adjacent cells (e.g., as a consequence of local buckling or fracture events at the nodes [52]).

Figure 4.4 displays contours of Mises stress, for the same lattice under the same applied external strain, for the two different boundary conditions. Much higher stress levels are noticeable

for the periodic boundary conditions, indicating higher strain energy (and higher stiffness). Notice that as expected, the free-edge BC localizes the strain energy at the nodes with the bars carrying minimal stress. As shown in Figure 4.5, the difference in modulus prediction between the two BCs can be in excess of an order of magnitude.

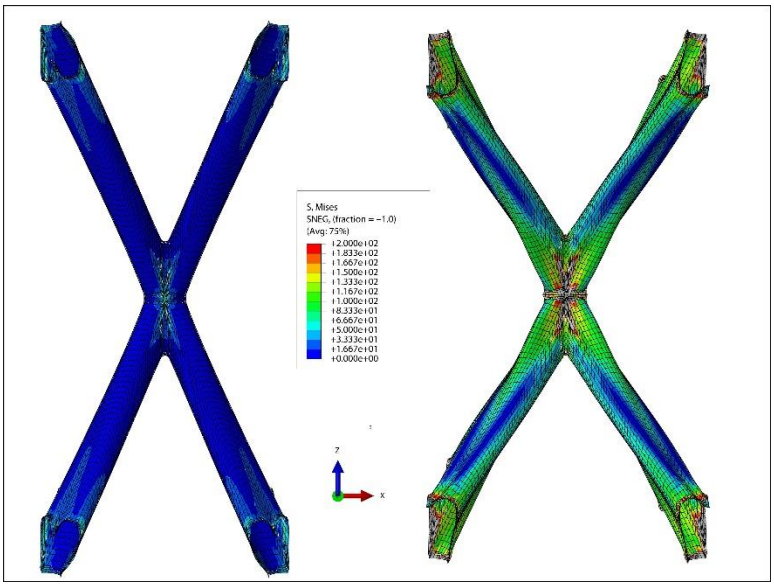

Figure 4.4 The insets represent contours of the Von Mises stress in Finite Elements simulations, with free edge (left hand) and periodic (right hand) boundary conditions.

The results of conventional stiffness measurements performed upon unloading with a universal (Instron) test frame (Figure 4.5) result in Young's moduli even lower than predicted by the free-edge BC simulations, generally by a factor 2-3. This is attributed to the fact that the necessary load application results in the characterization of a post-buckled or post-fractured lattice, which can easily be an order of magnitude more compliant than the pristine material. Although the free-edge BCs limit the constraining effects of the neighboring cells to a minimum (hence mimicking some nodal fracturing and buckling), the simulations nonetheless model a pre-buckled unit cell. Importantly, traditional Instron measurements provide moduli that are more than an order of magnitude lower than those predicted by FE simulations with periodic boundary conditions (the typical BC of choice for periodic materials). Conversely, the vibrometry measurements presented

in this research are generally ~5 times higher than the Instron measurements, and approach the simulation results obtained with fully periodic BCs (generally within a factor of 2, with the exception of sample B, $\bar{\rho} = 0.09\%$, for which the experimental result is 10 times lower than the FE result; we surmise that this is due to its "stubby" geometry, see Table 4.1). This confirms that non-contact vibrometry allows extraction of moduli of a pristine structure, without introducing damage during the measurement. The factor of 2 discrepancy with the simulations can be attributed to deviations from the idealizations assumed in the simulations (in particular the assumption that all unit cells deform identically), and to manufacturing imperfections.

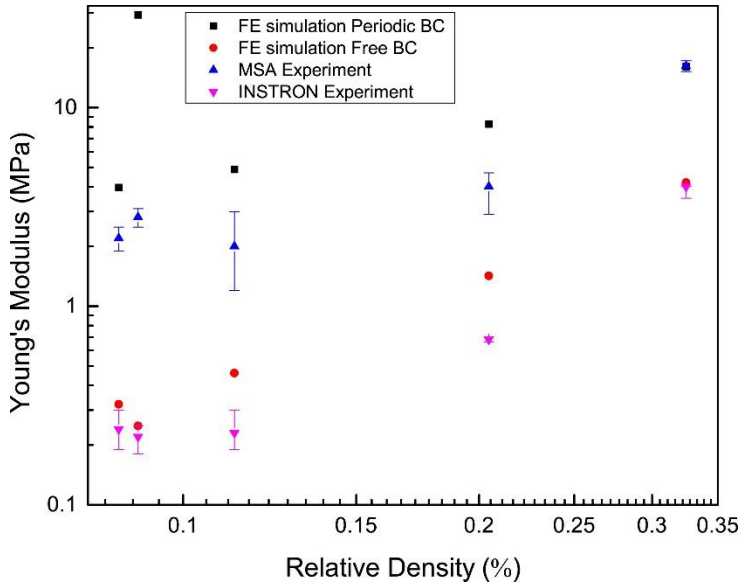

Figure 4.5 Comparison of experimental results and Finite Element simulations for the compressive modulus of ultralight micro-lattices. Notice that Laser Doppler Vibrometry (MSA) captures moduli that are consistently ~5X larger than provided by conventional compression (Instron) tests.

CHAPTER 5. CHARACTERIZATION, MODELING AND OPTIMIZATION OF DAMPING MECHANISMS IN HOLLOW METALLIC MICROLATTICES

In this chapter, we investigate the damping and energy dissipation mechanisms in hollow metallic microlattices and optimize their design for maximum energy dissipation and damping figure of merit [1], defined as $\Phi = E^{1/3} \tan\delta / \rho$, with E the effective Young's modulus of the lattice (in compression), tanδ the effective loss factor (damping coefficient) and ρ the lattice density. This material index expresses how fast a clamped plate subject to forced vibrations reaches rest when the forcing term is removed. The chapter is organized as follows: section 5.1 presents the experimental protocol adapted to separate and quantify several energy loss mechanisms possibly responsible for the unique damping characteristics of microlattices; the dominant mechanism is identified; in section 5.2, this mechanism is captured by a simple mechanical model, which is then used for optimal design studies. The summary of this chapter is available in [77].

5.1 Experimental Investigation of Energy Loss Mechanisms

5.1.1 Synopsis

All nickel hollow microlattices were fabricated with the process discussed in chapter 3. Table 5.1 reports the geometrical parameters of all samples used in this chapter.

The cyclic compressive behavior of lattices with thickness-to-diameter ratio below the critical value (Eq.(1.1)) is shown in Figure 5.1. Four nominally identical lattices (see Table 5.1 for details) were cycled to different strain amplitudes, for ~100 cycles. A few key characteristics

clearly emerge: (i) The material initially undergoes elastic deformation, which is followed by a long, fairly flat stress plateau. (ii) Upon unloading, the initial shape of the sample is almost entirely recovered. (iii) During a cycle, substantial hysteresis is observed, indicating energy dissipation (damping). (iv) The loading portion of the first cycle is substantially different from the second one, indicating irreversible fracture events; but after a few cycles of 'shakedown', the subsequent cycles quickly become self-similar, resembling the behavior of a non-linear viscoelastic material. The energy dissipated in each cycle is attributed to a number of physical mechanisms:

(i) *Fracture energy and plastic work*. Particularly important during the first few cycles, these mechanisms are expected to largely disappear after 'shakedown'.

(ii) *Elastic buckling*. When a lattice bar buckles, it dissipates strain energy, which is recovered upon unloading.

(iii) *Macro-scale friction*. When the lattice is compressed to large strains, members enter in contact with each other and dissipate energy by frictional interactions.

(iv) *Viscous dissipation*. Viscous air damping within and around the very thin hollow bars is a cause of energy loss.

(v) *Micro-scale friction*. Small micro-cracks present in the lattices dissipate energy through frictional interaction at the crack edges, even at very small applied strain.

(vi) *Intrinsic material damping*. Intrinsic damping in the constituent material contributes to energy loss.

This section describes an experimental protocol aimed at separating and quantifying the six mechanisms discussed above. Large-strain quasi-static cyclic compressive tests are performed to separate mechanism (i) from (ii) and (iii) and are described in section 5.1.2 Mechanisms (v) and (vi) are isolated by resonant experiments, performed at nearly zero strain (section5.1.3). Finally,

mechanism (iv) is separated by repeating all tests in air and vacuum (section 5.1.4). The observation and quantitative analyses of section 5.1.2-4 are ultimately summarized in section 5.1.5.

5.1.2 Large-strain measurements

All large-strain quasi-static compression tests were performed with a servo electrical INSTRON 8862 frame and a National Instrument SCXI data acquisition system. The actuator, featuring an integral concentrically mounted LVDT for precise measurement of position, moved at testing speeds of 100 mm/min to 1 μm/hr and accuracy of 10 μm/s. The load was measured by a 250gr Honeywell load cell. The LabVIEW software was used to collect load and displacement data. Engineering strain and stress are defined as $\varepsilon=\delta/L_0$, $\sigma=P/A_0$ where δ is displacement measured by the LVDT and P is the load measured by external load cell. L_0, and A_0 represent the initial length and the cross section area, respectively. Figure 5.1 shows results from samples A-D (Table 5.1) at different strain levels (5%, 10%, 25%, and 50%). All samples were without face sheets and tested for ~100 cycles.

Dissipated energy and damping capacity were extracted from the stress-strain data. The dissipated energy over a cycle, ΔU , is by definition the area within the hysteresis loop, whereas the loss coefficient, Ψ , was simply obtained by normalizing ΔU with the energy under the loading curve, U, i.e., $\Psi = \Delta U / U$ [76, 77].

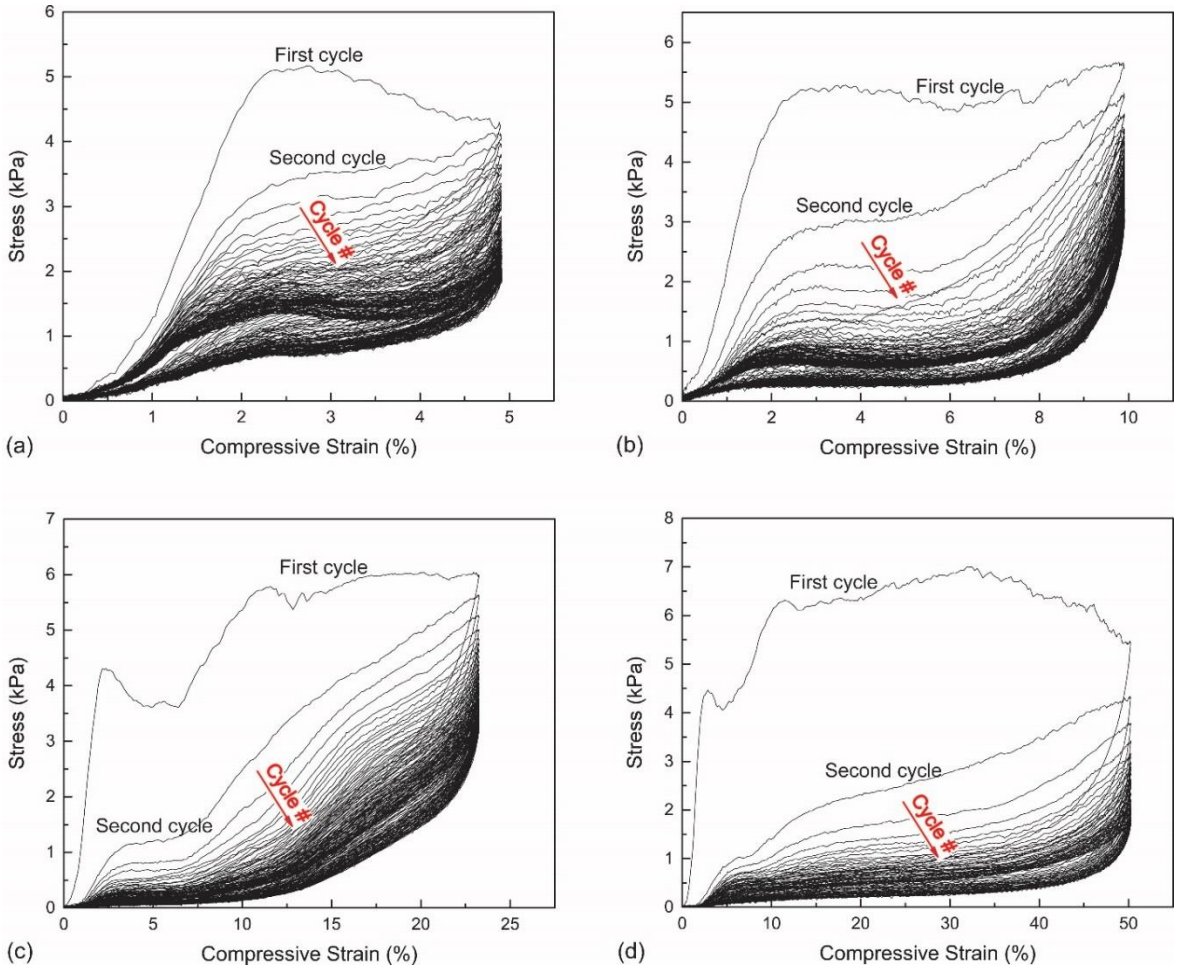

Figure 5.1 Multi-cycle compression experiments on hollow metallic microlattices: results for nominally identical samples A-D (see Table 5.1 for geometric details) at different strain amplitudes. (a) Sample A under 5% strain amplitude; (b) Sample B under 10% stain amplitude; (c) Sample C under 25% strain amplitude; and (d) Sample D under 50% strain amplitude. All samples have been cycled ~100 times.

The evolution of the dissipated energy per cycle with cycle number is plotted in Figure 5.2, for different values of compressive strain amplitude. The dissipated energy monotonically decreases with cycle number for all strain amplitudes, but with a slope that is dramatically reduced after approximately 10 cycles. The difference between the initial energy dissipation and the "plateau" value expresses the contribution of irreversible mechanisms, i.e., partial nodal fractures and possible localized plastic deformation. Conversely, the "plateau" value expresses the combination of all the other mechanisms mentioned above; this energy loss is recurrent in every

cycle and hence is available for damping applications. This plateau might include loss mechanisms that are related to large-strain phenomena (namely buckling-related damping) as well as micro-strain phenomena (intrinsic material damping, frictional losses at crack edges, etc…). Isolating these two classes of energy loss requires performing tests at virtually zero strain, hence eliminating buckling-related modes. This was accomplished as discussed in the next section.

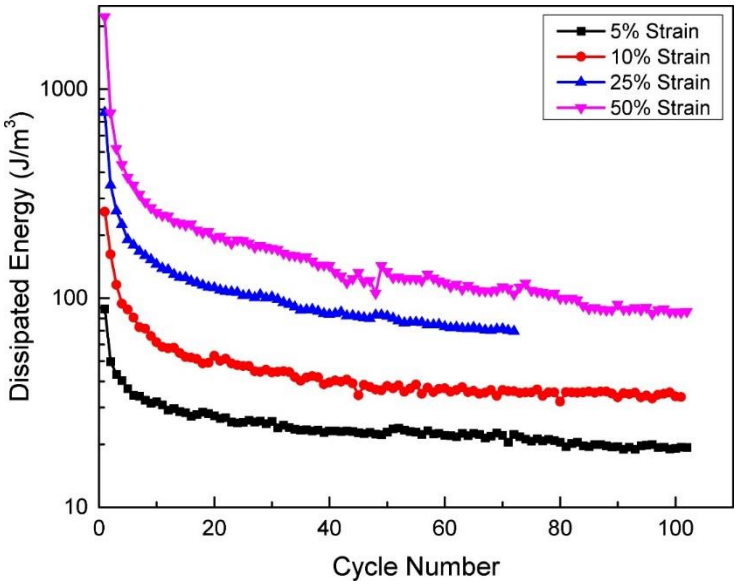

Figure 5.2 Dissipated energy vs. cycle number for nominally identical samples A-D (see Table 5.1 for geometric details) at different strain amplitudes.

We notice that a zero-slope plateau is not exactly reached after 100 cycles, indicating continued (although much reduced) damage upon cycling. This behavior would somewhat limit the applicability of these materials for high-cycle applications. This deficiency could be addressed by an increase in the toughness of the constituent material.

Table 5.1 Summary of geometrical properties of all microlattices tested in this chapter.

Sample	Wall thickness t (μm)	Strut diameter D (μm)	t/D	Strut length L (μm)	Strut angle (°)	Density (mg/cc)	Relative Density %
A	1.2±0.12	560±30	$(2.1\pm0.4)\times10^{-3}$	4662±120	60±2	11.75	0.09±0.01
B	1.2±0.12	560±30	$(2.1\pm0.4)\times10^{-3}$	4662±120	60±2	9.84	0.09±0.01
C	1.2±0.12	560±30	$(2.1\pm0.4)\times10^{-3}$	4662±120	60±2	12.08	0.09±0.01
D	1.2±0.12	560±30	$(2.1\pm0.4)\times10^{-3}$	4662±120	60±2	13.33	0.09±0.01
E	1±0.1	560±30	$(1.8\pm0.3)\times10^{-3}$	4662±120	60±2	7.66	0.075±0.01
F	0.5±0.05	120±7	$(4.2\pm0.6)\times10^{-3}$	1050±32	60±2	19.48	0.15±0.02
G	0.5±0.05	460±20	$(1.1\pm0.2)\times10^{-3}$	1743±36	55±2	8.817	0.17±0.02
H	4±0.4	430±15	$(9.3\pm0.7)\times10^{-3}$	4000±120	60±2	28.95	0.31±0.04
I	0.5±0.05	175±10	$(2.8\pm0.5)\times10^{-3}$	817±30	50±2	15.15	0.26±0.03

5.1.3 Small-strain measurements

Resonant measurements at infinitesimal strain were performed to capture intrinsic damping mechanisms, i.e. mechanisms that are not related to large deformation (or buckling) of the lattice members. All experiments were carried out with a Laser Doppler Vibrometer (Polytec MSA-500). A microlattice sample was bonded to carbon-epoxy face sheets. The lower face sheet was oscillated with a piezoelectric actuator within a sinusoidal signal at very low amplitude (~10nm), sweeping the frequency within the range 0-5kHz. The velocity of the upper plate was monitored with the Doppler Vibrometer in scanning mode (to identify the modal shapes). A representative frequency response of a sample (Sample E in Table 5.1) is shown in Figure 4.2.

As the mass of the face sheets is ~10 times larger than the mass of the sample, the sandwich panel can be modeled as a discrete oscillator, with two masses connected by a spring and a damper in parallel. This simplification allows fitting of the measured frequency response on a classic oscillator model, thus allowing extraction of the damping properties of the microlattice. Incidentally, the location of the peaks provides information of the stiffness of the sample, from which the compressive Young's modulus of the microlattice can be extracted as discussed in chapter 4. Two different methods can be used to extract the damping coefficient of the material from the shape of the resonant peak: (i) the curve fit method, where the theoretical shape of the peak is fitted on the experimental frequency response; (ii) the half-bandwidth method, where the aspect ratio of the peak is directly correlated to the damping coefficient.

The equation of motion for the relevant mass-spring-damper can be expressed as:

$$\ddot{x} + 2\omega_n \zeta \dot{x} + \omega_n^2 x = 2\omega_n \zeta \dot{y} + \omega_n^2 y \tag{5.1}$$

with ζ and ω_n the damping ratio and natural frequency of the microlattice, respectively, and *x* and *y* the displacement of the two masses (face sheets). If the lower face sheet is oscillated with a harmonic sinusoidal wave, $y(t) = Ae^{i\omega t}$, the response $x(t)$ can be written as [80]:

$$x(t) = X(i\omega)e^{i\omega t} \tag{5.2}$$

with:

$$\frac{|X(i\omega)|}{A} = \left[\frac{1+(2\zeta\omega/\omega_n)^2}{\left[1-(\omega/\omega_n)^2\right]^2+(2\zeta\omega/\omega_n)^2}\right]^{1/2} \tag{5.3}$$

For method (i), Eq. (5.3) was fitted on the experimentally measured frequency response, and the damping ratio, ζ and natural frequency, ω_n, were extracted. The results of the fit for sample E in Table 5.1 are reported in Figure. 5.3 and the extracted damping ratio was $\zeta = 0.0328$.

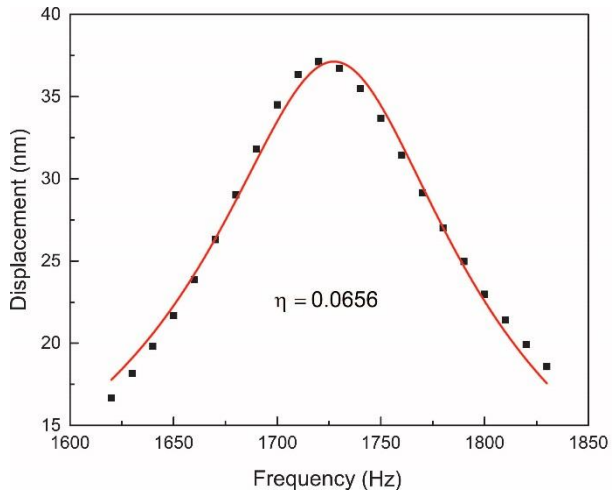

Figure. 5.3 Extraction of the damping coefficient from the frequency response of sample E (see Table 5.1 for geometric details), captured by Laser Doppler Vibrometry by using curve fit method.

Wong *et al.* [78] have reported that for loss factors $\eta = 0.28$, the half-bandwidth method (method (ii) mentioned above) is accurate enough to measure damping. In this method, the loss factor η is extracted from the ratio of the resonant peak width (measured at an amplitude of $1/\sqrt{2}$ of the peak amplitude) to the resonance frequency [81]. Figure. 5.4 schematically demonstrates the application of the half-bandwidth method for sample E (Table 5.1), from which a loss factor of $\eta = 0.0654$ was calculated. For small damping ($\zeta < 0.07$), the loss factor η is linearly related to the damping ratio, ζ as $\eta = 2\zeta$ [78]. Hence for this sample, both methods produce nearly identical results.

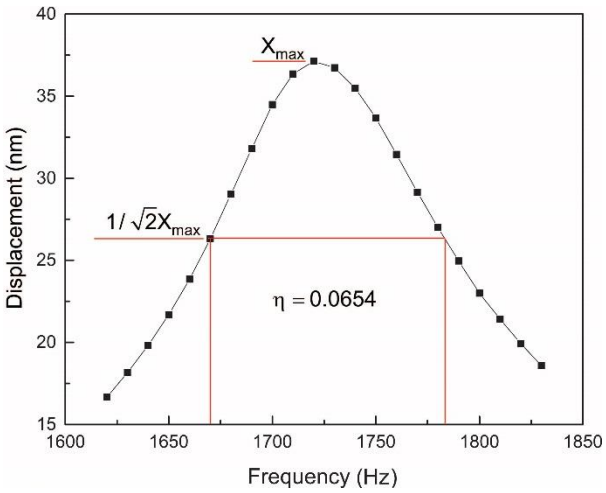

Figure. 5.4 Extraction of the damping coefficient from the frequency response of sample E (see Table 5.1 for geometric details) captured by Laser Doppler Vibrometry, by using the half-bandwidth method.

For small damping, the loss factor is also linearly related to the loss coefficient, Ψ [78]. If Ψ is calculated on a quarter-cycle (compressive loading-unloading), as indicated in section 5.1.2, the correlation is:

$$\Psi = \frac{4\pi\eta}{5} \tag{5.4}$$

This correlation allows direct comparison of the results from small-strain and large-strain experiments, hence facilitating the quantitative assessment of energy loss mechanisms in ultralight microlattices. We also notice that the loss factor, η, is equal to $\tan\delta$, with δ the phase angle between stress and strain under sinusoidal loading. This notation will be used in section 5.1.5.

5.1.4 The effect of viscous dissipation

As the ultralight microlattices under consideration are made of thin hollow bars (with diameters of the order of 100 microns), the effect of viscous dissipation by air trapped in the hollow tubes and air displaced during deformation on damping might be significant. To quantify this effect, two representative samples were tested with both the large-strain (INSTRON cyclic test) and the small-strain (Doppler vibrometry) techniques, both in air and under vacuum. The vacuum chamber pressure was less than 5mTorr. The results, reported in Figure 5.5, indicate that the effect of viscous dissipation on damping is fairly small, even under resonant conditions (less than 1% for quasi-static large-strain loading and approximately 15% for the resonant test).

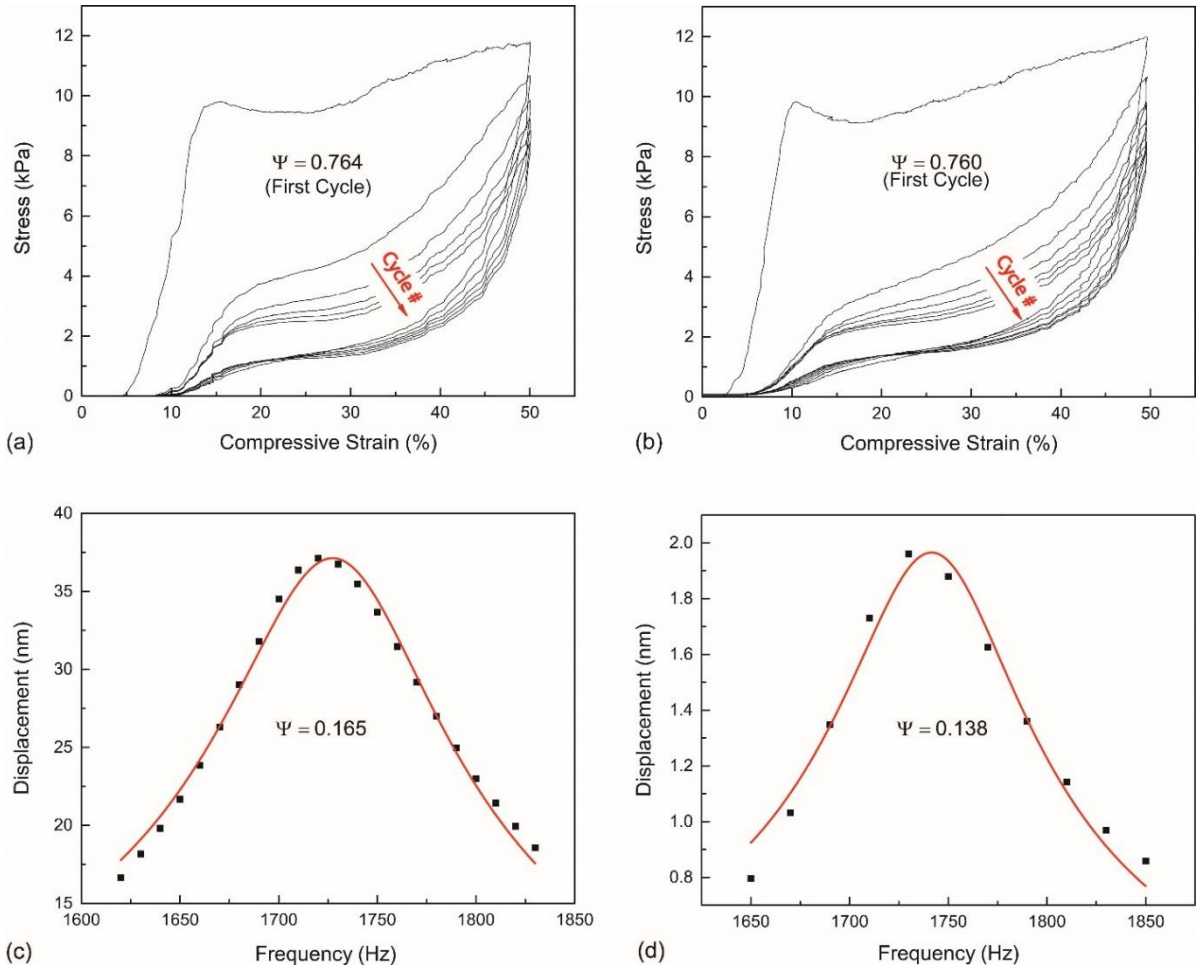

Figure 5.5 The effect of viscous damping. Stress-strain curves obtained for sample I in air (a) and vacuum (b), and resonant peaks obtained for sample E in air (c) and vacuum (d). See Table 5.1 for geometric details. Notice that viscous dissipation increases the damping coefficient by 1% in large-scale compression experiments, and by 15% in resonant experiments.

5.1.5 Quantitative assessment

In order to quantify the effect of each energy loss mechanism on the damping behavior of ultralight microlattices, it is useful to combine the results of the experiments detailed in section 5.1.2-5.1.4 as indicated in Figure 5.6. Although sample E (Table 5.1) is chosen as a representative material, the behavior is qualitatively similar for all samples under investigation.

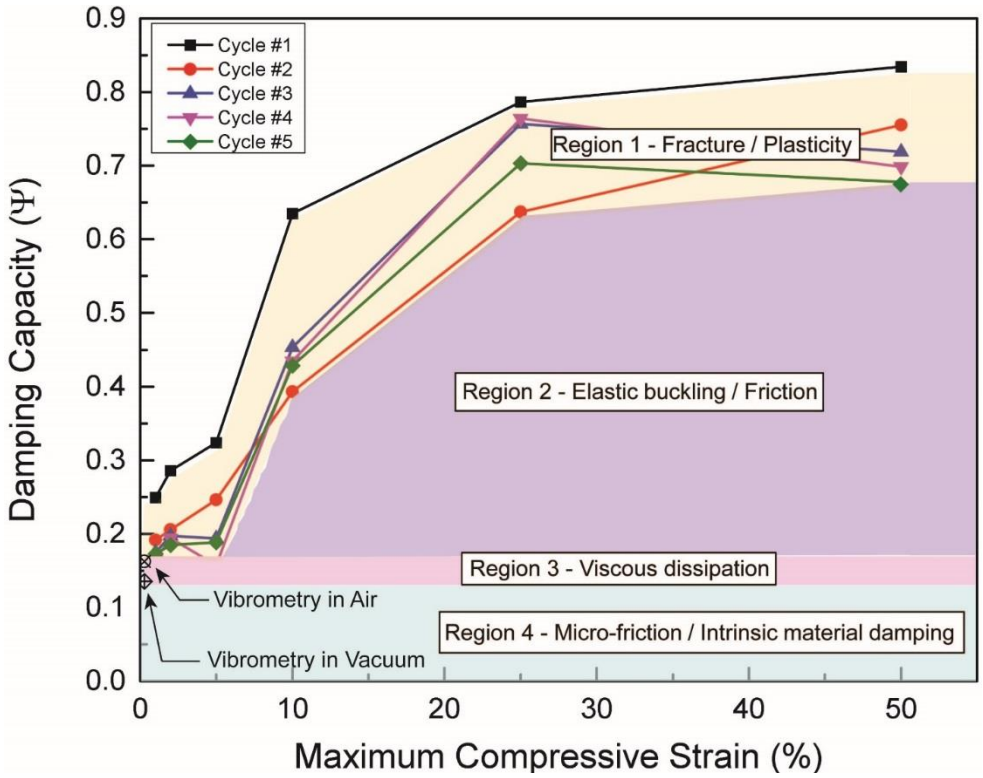

Figure 5.6 Damping capacity vs. maximum compressive strain for different cycles. The damping capacity measured by resonant tests at infinitesimal strain is consistent with the compression test results at small strain amplitude. This figure allows quantitative identification of the contributions of different damping mechanisms. The dominant mechanism (Region 2) is a unique form of structural damping, largely induced by coordinated local buckling and elastic recovery of the bars upon cycling.

The damping capacity (loss coefficient) extracted from quasi-static large-strain compression tests is reported for different maximum strains (1, 2, 5, 10, 25, and 50%) and 5 cycle numbers (only 5 cycles are reported for clarity). The damping capacity extracted from the resonant tests was reported on the same plot at zero strain. In general, the damping capacity of materials is frequency dependent; as the two experiments are performed at very different frequencies ($f<0.1$ Hz for the compression tests, and $f\sim1{,}500$Hz for the resonant tests), there is no guarantee that the damping obtained with resonant tests would be meaningful in quasi-static situations. Notice, though, that the resonant damping capacity (~0.16) agrees well with the damping capacity at the smallest finite strain (5%), suggesting minimal frequency dependence in this range and providing

confidence in the approach. Finally, the amount of viscous damping on the resonant tests (15%, see section 5.1.4) is presented as well. Notice that the damping capacity is initially a strong function of the strain amplitude, but saturates at amplitudes ~30%.

The combined results allow clear separation of the various energy loss mechanisms, and quantitatively express their contribution to the damping capacity of the microlattice. For each strain amplitude, four distinct regions are evident (Figure 5.6): Region 1, expressing contributions of fracture and plasticity, which are not really a damping phenomenon (mechanism (i) in the classification section 5.1.1); Region 2, which displays the contribution of buckling-related and frictional damping (mechanisms (ii) and (iii)), which cannot be easily separated with this experimental protocol; Region 3, expressing the contribution of viscous damping (mechanism (iv)); and finally Region 4, expressing the contribution of intrinsic material damping phenomena (responsible at most for $\eta = 0.0006$ [82]) and micro-friction (mechanism (v) and (vi)).

The relative importance of the 4 regions is a strong function of the strain amplitude. Region 2 (largely attributed to buckling-related damping) plays a significant role at strain amplitudes larger than 10% and becomes the dominant mechanism at strains in excess of 25%. The relative contributions do not change at amplitudes larger than ~30%. If we discard fracture/plasticity-related energy loss, at 50% strain, for sample E, we have: Region 2: 60%; Region 3: 4%; Region 4: 17%.

The dominant contribution of Region 2 justifies the modeling efforts presented in the following section, ultimately aimed at optimizing the microlattice geometry to maximize this damping mechanism.

It is instructive to compare the damping performance of the materials tested in this research with the universe of existing metallic materials. As discussed, the conventional figure of merit for

the damping performance of plates, $\Phi = E^{1/3} \tan\delta / \rho$ [1], is used for comparison. For all microlattices, the loss coefficient $\Psi = \Delta U / U$ is extracted from quasi-static measurements, and $\tan\delta$ is estimated from Eq. (5.4) (recall that η=tanδ). The Young's modulus, *E*, is extracted from the linear elastic portion of the stress-strain curve, and the density, ρ, is obtained by measuring both the weight and the volume of the samples. The envelope of all experimental results (Table 5.1) is presented in Figure 5.7 alongside the universe of metallic materials (monolithic metals, metal-matrix composites and metallic foams). With this choice of axes, design lines (loci of uniform Φ) have slope of -1. *Notice that ultralight nickel microlattices are vastly superior to any metal available.* It is important to emphasize, though, that the extremely low density of these samples implies that the actual amount of energy that can dissipated in each compression cycle is rather low, potentially forcing the designer to adopt unreasonably large volumes. In the next section, a simple analytical model for the dissipated energy per cycle (and for Φ) will be derived and subsequently adapted in an optimization problem to identify the geometric designs that will maximize the damping performance of microlattices.

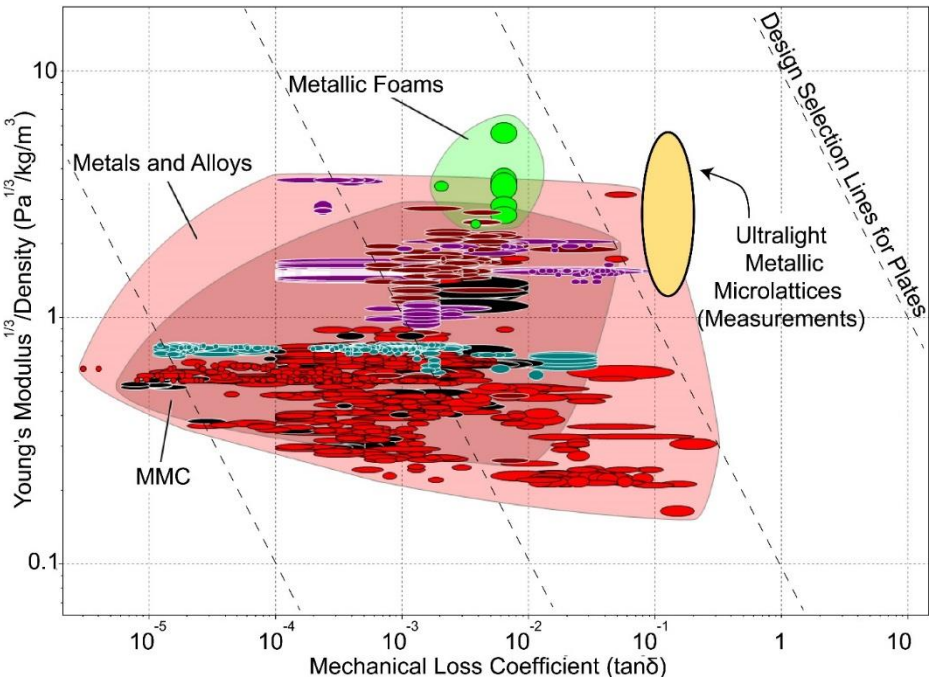

Figure 5.7 Material selection chart for vibration management of plates. All metallic materials (including Metal Matrix Composites) are depicted, alongside the hollow metallic microlattices tested in this work (the ellipse represents the envelope of experimental results).

5.2 Modeling of Buckling-related Energy Dissipation

The experimental results presented in section 5.1 clearly show that the surprisingly high energy loss exhibited by ultralight hollow microlattices upon large-strain cycling can be mostly attributed to a unique form of structural damping. This mechanism is related to coordinated local buckling of individual bars, and is explained here. Experimental evidence indicates that upon macroscopic compression, individual lattice bars locally buckle (generally near the nodes), and subsequently undergo large rotations to accommodate the global lattice strain. Buckling generally occurs in a layer-by-layer fashion (the layer of bars connected to one of the compression platens buckles first, followed by the adjacent layer, and so on until the maximum applied strain is reached). The mechanical response of an individual bar can be clearly understood with a simple

Finite Elements simulation of a hollow cylinder loaded in a cantilever mode (Figure 5.8a). The simulation is performed in dynamic mode with ABAQUS Explicit under displacement control, as convergence for these extremely unstable systems is difficult with quasi-static algorithms; nonetheless, a sufficiently small strain rate was chosen to render inertia effects negligible (the kinetic energy was verified to be very small compared to the elastic energy during the entire simulation). The cylinder is 4mm long, has a diameter of 500μm and a wall thickness of 500nm. One end is fully clamped and the other end is displaced vertically by 1mm with a displacement rate of 0.67m/s, and subsequently displaced back to the original position with the same rate. The material is modeled as elastic-perfectly plastic, with properties representative of nano crystalline Nickel (Young's Modulus, E=200GPa, Poisson's ratio, ν=0.3, yield strength, σ_y=2.5GPa and density, ρ=8000kg/m^3). The element used is a 4-node shell, with reduced integration hourglass control and finite membrane strain (S4R). The cross-section at the free end is maintained circular during the entire cycle. Self-contact (hard, frictionless) is imposed on the cylinder to realistically capture large post-buckling deformation. The shape at the end of the loading cycle, together with contours of the Von Mises stress, are presented in Figure 5.8a. The load-displacement relationship for the cylinder is shown in Figure 5.8b. After a linear-elastic response, the cylinder buckles with a sudden and almost complete drop in the load; subsequently, it continues to deform fairly linearly, but with a much reduced stiffness. Upon unloading, the cylinder retraces the post-buckling loading curve until the buckling point, and then snaps back on the pre-buckling curve. During an entire cycle, the cylinder dissipates an amount of energy given by the nearly triangular area shaded in Figure 5.8b. This energy is dissipated through high-frequency vibration of the bar. Although the bars in a microlattice sample experience a more complex loading scenario (with combinations of compression, bending and shear, and non-trivial bar-bar interactions), the fundamental behavior

does not change. The energy that is lost in a large-scale compression cycle of a microlattice can be estimated by adding the energy contributions of each bar that buckles. The next sub-section details such a model.

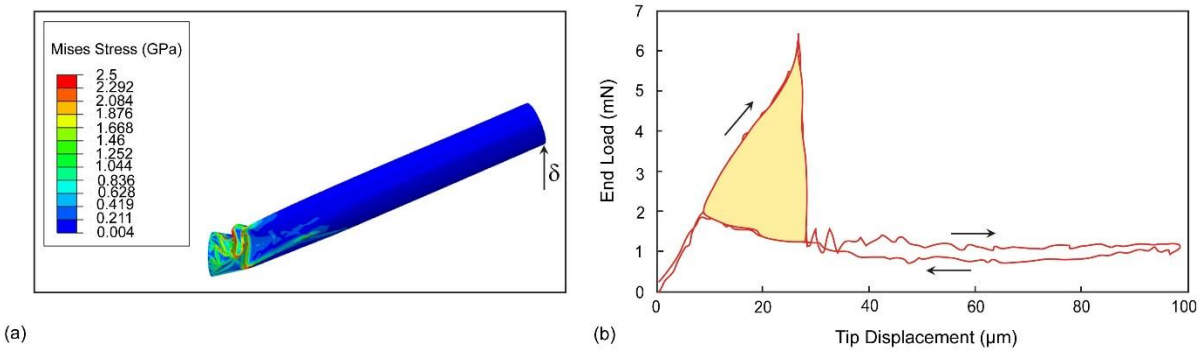

Figure 5.8 (a) Finite Element simulation of a clamped hollow cylinder loaded in a cantilever mode. (b) Load-displacement curve, showing the energy dissipated in a cycle.

Incidentally, the macroscopic compressive behavior of microlattices (Figure 5.1) can be interpreted in the context of local negative stiffness phenomena [81, 82], a mechanism that is well known to generate effective stress-strain curves similar to those in Figure 5.1 [58, 83]; the load-displacement curve of a single bar can be modeled by a tri-linear spring, with two positive stiffness sections interrupted by a sharp negative stiffness portion. Although a model of the collective behavior of tri-linear springs in series has been recently published to predict the compression behavior of carbon nanotube mats [58], the application of that model to the hollow microlattice presents a number of difficulties (largely due to bar-bar interactions and local fracture at the nodes). For the sake of this work, the simple model described below suffices to capture the main behavior of the system.

5.2.1 Mechanical model

A free-body diagram for a bar within the microlattice under compression is depicted in Figure 5.9. Notice that as the lattice topology is not stretching dominated, each bar experiences a combination of axial compression, bending and transverse shear.

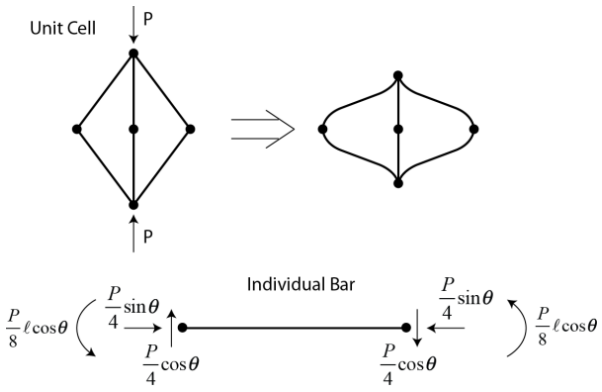

Figure 5.9 Schematic of the deformation of a unit cell of the lattice under external compression, and free-body diagram of a single bar. Note that each bar experiences a combination of axial compression, bending and shear loads.

Local buckling can occur by shell compression near the clamped end (where the normal compressive stress due to bending and axial load is maximum, see Figure 5.8a) or by shell shear (throughout the beam length). Because the shear stress is nearly zero where the normal stress is maximum (and vice versa), the two mechanisms are not heavily coupled. The implication – verified by FE simulations as explained below – is that the buckling load of the cylinder can be estimated as the minimum between the shell compression and the shell shear critical loads. Expressing the axial load and the moment on the bar as a function of the compressive load applied on one unit cell, *P*, the maximum normal compressive stress in the bar can be written as:

$$\sigma_{max} = \frac{P\ell\cos\theta}{2\pi tD^2} + \frac{P\sin\theta}{4\pi tD} \tag{5.5}$$

where t, D, ℓ and θ are the thickness, diameter, length and inclination of the lattice bar, respectively (Figure 3.2). The bar will buckle by shell compression when the maximum stress in the bar equals

the critical local buckling stress. According to classic buckling theory [86], local buckling in a cylindrical shell of circular cross section under combinations of axial compression and bending occurs when the normal stress on the compressive side of the shell reaches the critical stress for axisymmetric (compression-only) buckling i.e.:

$$\sigma_{cr} = \frac{2Et}{D\sqrt{3(1-\nu^2)}} \tag{5.6}$$

with E and ν are the Young's modulus and Poisson's ratio of the material. For the Nickel microlattice under consideration, $E = 210\text{GPa}$ and $\nu = 0.3$, respectively. By equating Eqs. (5.5) and (5.6), the buckling strength of the bar under compression-bending (equal to ¼ of the strength of the unit cell) can be expressed as:

$$P_{cr,bar} = \frac{P_{cr}}{4} = \frac{2\pi Et^2}{\sqrt{3(1-\nu^2)}(\sin\theta + \frac{2\ell\cos\theta}{D})} \tag{5.7}$$

The critical stress for shear buckling in a cylinder of circular cross-section can be estimated analytically as [87]:

$$\tau_{cr} = 1.5E\sqrt{\frac{\sqrt{Dt/2}}{\ell}}\frac{t}{D} \tag{5.8}$$

Shear buckling occurs when the maximum shear stress in a single bar (given by $P\cos\theta/(2\pi Dt)$) equals the critical stress, which leads to:

$$P_{cr,bar}^{sh} = \frac{P_{cr}^{sh}}{4} = \frac{3\pi Et^2}{4\cos\theta}\sqrt{\frac{\sqrt{Dt/2}}{\ell}} \tag{5.9}$$

The ratio between the shell shear and the shell compression buckling loads will then scale as:

$$\frac{P_{cr}^{sh}}{P_{cr}^{b+c}} \sim \left(\frac{\ell}{D}\right)^{1/2}\left(\frac{t}{D}\right)^{1/4} \tag{5.10}$$

As ℓ / D and t / D increase, shell compression buckling becomes the dominant failure mechanism. Although Eqs. (5.7) and (5.9) predict comparable buckling loads for all samples in Table 5.1, numerical buckling analyses (eigenvalue extractions) performed with ABAQUS on single cantilever bars clamped at one end and subjected to an inclined load at the other end reveal that Eq. (5.7) is very accurate while Eq. (5.9) is too conservative. The implication is that all samples under investigation fail by local shell compression buckling, at a critical load that is very well captured by Eq. (5.7). This is in agreement with visual observations during the compression experiments. To verify that shear buckling is also inconsequential for all optimal geometries presented in section 5.2.2, numerical buckling analyses (eigenvalue extraction) were performed on a number of samples, with three conclusions: (i) for $\ell / D > 4$, buckling occurs by shell compression for $t / D > 0.0025$; (ii) for $\ell / D > 8$, buckling occurs by shell compression for $t / D > 0.001$; (iii) in all cases, the critical loads are in good agreement with Eq. (5.7). As all optimal designs satisfy the geometric conditions (i) or (ii) (see Figure 5.12), shear buckling is never a concern, and will henceforth be neglected.

An energy method is used to calculate the stiffness of bar. Upon global compression, the elastic energy stored in the entire unit cell is the sum of axial, shear and bending contributions (the shear term is the smallest, but not always insignificant):

$$U = \frac{P^2 \cos^2\theta\, \ell^3}{6E\pi D^3 t} + \frac{P^2 \sin^2\theta\, \ell}{4E\pi D t} + \frac{P^2 \cos^2\theta\, \ell}{2G\pi D t} \tag{5.11}$$

with G the shear modulus of the material ($G = E/(2(1+\nu)) = 81$ GPa).

The unit cell stiffness can be defined as $K = P/\delta$, with δ the vertical displacement of the unit cell. The strain energy in the unit cell can be related to the displacement by $U = \frac{1}{2} P\delta$. By imposing that this equation be equal to Eq.(5.11), the stiffness of each bar can be calculated as:

$$K_{bar} = \frac{K}{2} = \frac{3\pi EtD^3}{2\ell^3 \cos^2\theta} \frac{1}{[1 + \frac{3}{2}\tan^2\theta(\frac{D}{\ell})^2 + 6(\frac{D}{\ell})^2(1+\nu)]} \tag{5.12}$$

Assuming that the entire elastic energy is dissipated upon buckling (a slight overestimation, as noted in Figure 5.8), the energy loss from each bar can be expressed as:

$$\Delta E_{bar} = \frac{1}{2}\frac{P_{cr,bar}^2}{K_{bar}} \tag{5.13}$$

In order to calculate the energy dissipation of the whole lattice, the number of bars that buckle at any given applied compressive strain must be evaluated. Assuming an infinite lattice experiencing layer-by-layer deformation, and assuming that each bar folds onto itself upon buckling (so that the compress cell has a thickness equal to 2D), the fraction of bars, *f*, that needs to buckle in order to accommodate the global lattice strain is given by:

$$f = \frac{\varepsilon_{\max}}{1 - D/(\ell \sin\theta)} \tag{5.14}$$

The number of bars in the whole lattice is given by $N_b = 16 n_x n_y n_z$, where n_x, n_y, and n_z are the number of unit cells in X, Y, and Z directions, respectively.

The dimensions of the lattice are related to the dimensions of the unit cell by $L = 2\ell\cos\theta_y$, $H = 2\ell\sin\theta n_z$, and $W = 2\ell\cos\theta_x$.

Finally, from a simple energy balance, the energy dissipation in the bulk structure is extracted as:

$$\Delta U = \frac{f\, N_b\, \Delta E_{bar}}{W\, L\, H} = \frac{2 f \Delta E_{bar}}{\ell^3 \sin\theta \cos^2\theta} \tag{5.15}$$

The continuum approximation underlying Eq. (5.14) is expected to be reliable for samples containing a large number of unit cells. As all samples available for characterization in this work

contained at most 3 unit cells, experimental verification of Eq. (5.15) presents some challenges. These challenges are exacerbated by the presence of manufacturing imperfections in most samples. To address these difficulties, and verify the reliability of the model, the following analysis was performed.

Figure 5.10 shows the dissipated energy per cycle after 100 cycles for four nominally identical samples (samples A-D in Table 5.1) tested at different strain amplitudes. The red markers represent experimental measurements, while the three lines are model predictions. The solid line is a plot of Eq. (5.15), for the nominal dimensions of the sample. Notice that the model significantly underpredicts the dissipated energy. This discrepancy is attributed to (i) finite size effects and (ii) manufacturing imperfections, and justified as follows. The dashed staircase curve represents predictions of the energy dissipated for each full layer collapse (one layer equals ½ unit cell), with the strains for layer collapse based on experimental observation (0 collapsed layers observed at 5% strain, 1 at 10% strain, 2 at 25% strain and 3 at 50% strain). This line represents the discrete version of Eq. (5.15) for a 2-unit cell sample. Finally, the dash-dot curve corrects for manufacturing imperfections, by estimating the dissipated energy per layer on the actual (counted) number of bars in each layer for the specific test samples (rather than calculating the number of unit cells based on measured overall sample sizes and unit cell nominal dimensions). Notice that the dash-dot curve is in very good agreement with the experimental measurements, for all values of compressive strain amplitude.

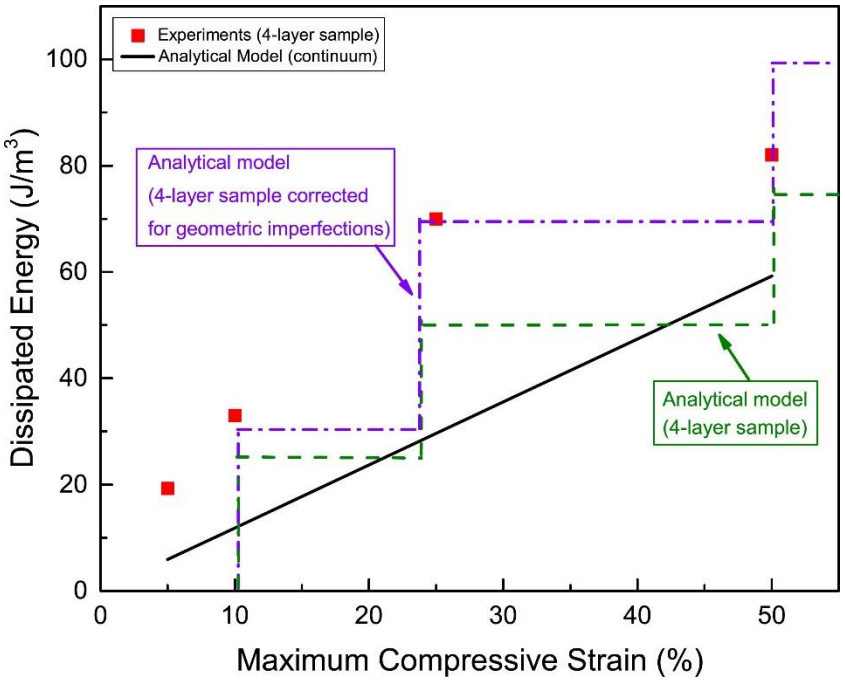

Figure 5.10 Dissipated energy in each cycle for samples A-D (the samples are nominally identical, see Table 5.1 for details) after 100 cycles, as a function of the maximum compressive strain applied in each cycle. The red markers represent experimental results, whereas the solid line depicts the analytical prediction from Eq. (5.15). The dashed line corrects the analytical model for a sample with only 4 unit cells across the thickness, based on visual observation of layer-by-layer buckling. The dash-dot line incorporates measured geometric imperfections in the samples.

In order to verify the model-experiment agreement for other sample geometries and relative densities, four different samples (samples D-G in Table 5.1) were tested at 50% compressive strain amplitude for ~100 cycles. The results are reported in Figure 5.11. Notice that the simple analytical model (Eq.(5.15)) can capture the dissipated energy per cycle quite accurately (with a discrepancy of ~13% - 45%, depending on sample geometry).

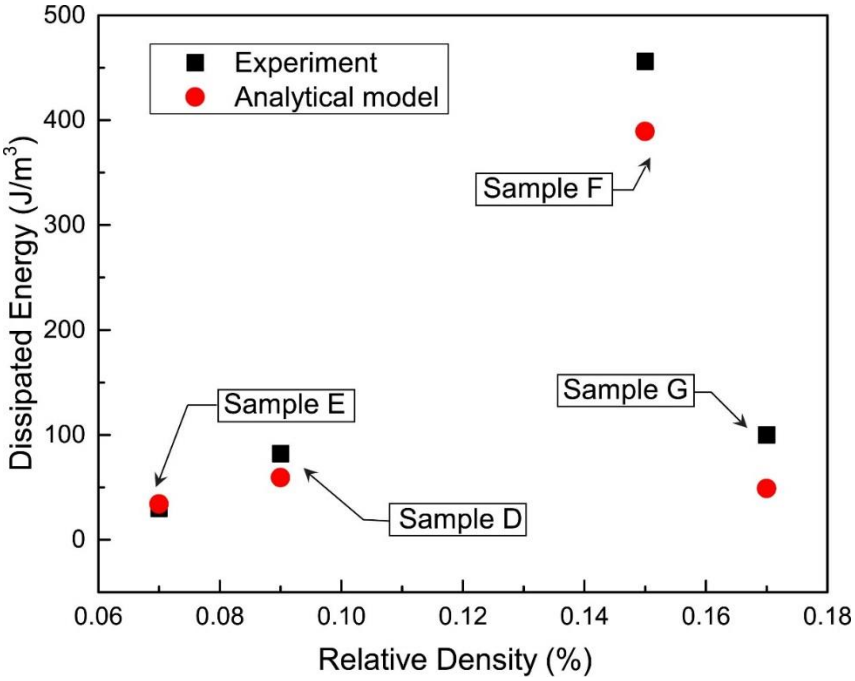

Figure 5.11 Dissipated energy in each cycle for samples D-G after 100 cycles. The black square markers represent experimental results, whereas the red circular markers depict the analytical prediction from Eq. (5.15).

It is worth emphasizing that the mechanical models presented in this section assume that the lattice response (both in terms of stiffness and strength, including the non-linear post-buckling behavior) is fully represented by the response of a single unit cell (or even a single bar). A number of recent studies have clearly indicated that this is not necessarily the case [23, 25]: this is particularly important for the buckling behavior, where different lattice topologies requires multi-cell Representative Volume Elements (RVE) of different dimensions to accurately capture the infinite lattice response [25]. A recent study showed that the situation is even more complex for hollow lattices dominated by local shell buckling, where details of the boundary conditions on the sides of the RVE have a dramatic effect; in some cases, single bar models can overpredict the buckling strength of a lattice by 2-5X [53]. Similar trends were observed for stiffness predictions, where the overprediction can be even more dramatic [54]. We emphasize that the goal of the analytical model contained in this work is to provide an order-of-magnitude estimate for the energy

loss in loading-unloading cycles on ultralight hollow lattices. The fact that simple (albeit somewhat inaccurate) models can capture the order of magnitude of the energy loss is used to (i) support the claim that structural damping is in large part due to local kinking of the bars, and (ii) extrapolate the best damping performance that can be expected from this kind of materials (see next section).

5.2.2 Trends for optimal design

The mechanical model described in the previous section can be used to explore the parameter space and identify optimal designs. Two optimization problems will be addressed: the maximization of the energy dissipated per cycle, ΔU, and the maximization of the damping figure of merit, $\Phi = E^{1/3} \tan\delta / \rho$.

5.2.2.1 Maximization of dissipated energy per cycle, ΔU

Expressed in non-dimensional form, the geometric parameters of the system are the truss angle, θ, the bar aspect ratio, D/ℓ and the cross-section aspect ratio, t/D.

The objective function (to be maximized) can be expressed as:

$$\Delta U = \frac{8\pi f E (t/D)^3}{9(1-\nu^2)\sin\theta} \frac{[1+3\tan^2\theta (D/\ell)^2/2 + 6(1+\nu)(D/\ell)^2]}{(\sin\theta + 2\cos\theta/(D/\ell))^2} \tag{5.16}$$

The range of the geometric parameters is dictated by manufacturing constraints, beam theory limitations and the recoverability condition (Eq.(1.1)), and can be expressed as follows:

$$\begin{aligned} &10^{-5} < t/D < (t/D)_{cr} \\ &2 < L/D < 16 \\ &D/\ell < 0.25 \\ &45^o < \theta < 75^o \end{aligned} \tag{5.17}$$

where L is the cell size ($L = 2\ell\cos\theta$, see Figure 3.2), and $(t/D)_{cr}$ is given by Eq.((1.1))[1].

The relative density of the samples is calculated from simple hollow truss geometry [19]:

$$\bar{\rho} = \frac{2\pi}{\cos^2\theta\sin\theta}\left(\frac{D}{\ell}\right)^2\frac{t}{D} \tag{5.18}$$

The relative density is swept in the range 0.01–2%, and for each density the constrained optimization problem described above is solved with the "fmincon" algorithm in MATLAB.

The energy loss versus the relative density of the material for different compressive strain amplitudes is depicted in Figure 5.12a, with optimal dimensions in Figure 5.12b-d. Importantly, and conveniently, the optimal lattice geometry is independent of the maximum compressive strain, whereas obviously the dissipated energy is monotonic in the maximum strain amplitude.

[1] To be consistent with a layer-by-layer deformation model (implicit in Eq.(5.14)), Eq. (1.1) is modified by assuming $\varepsilon_{\max} = 50\%$ regardless of the actual values of $\varepsilon_{\max}$. This is a conservative choice based on the observation that each layer deforms by ~50% before the next layer starts buckling.

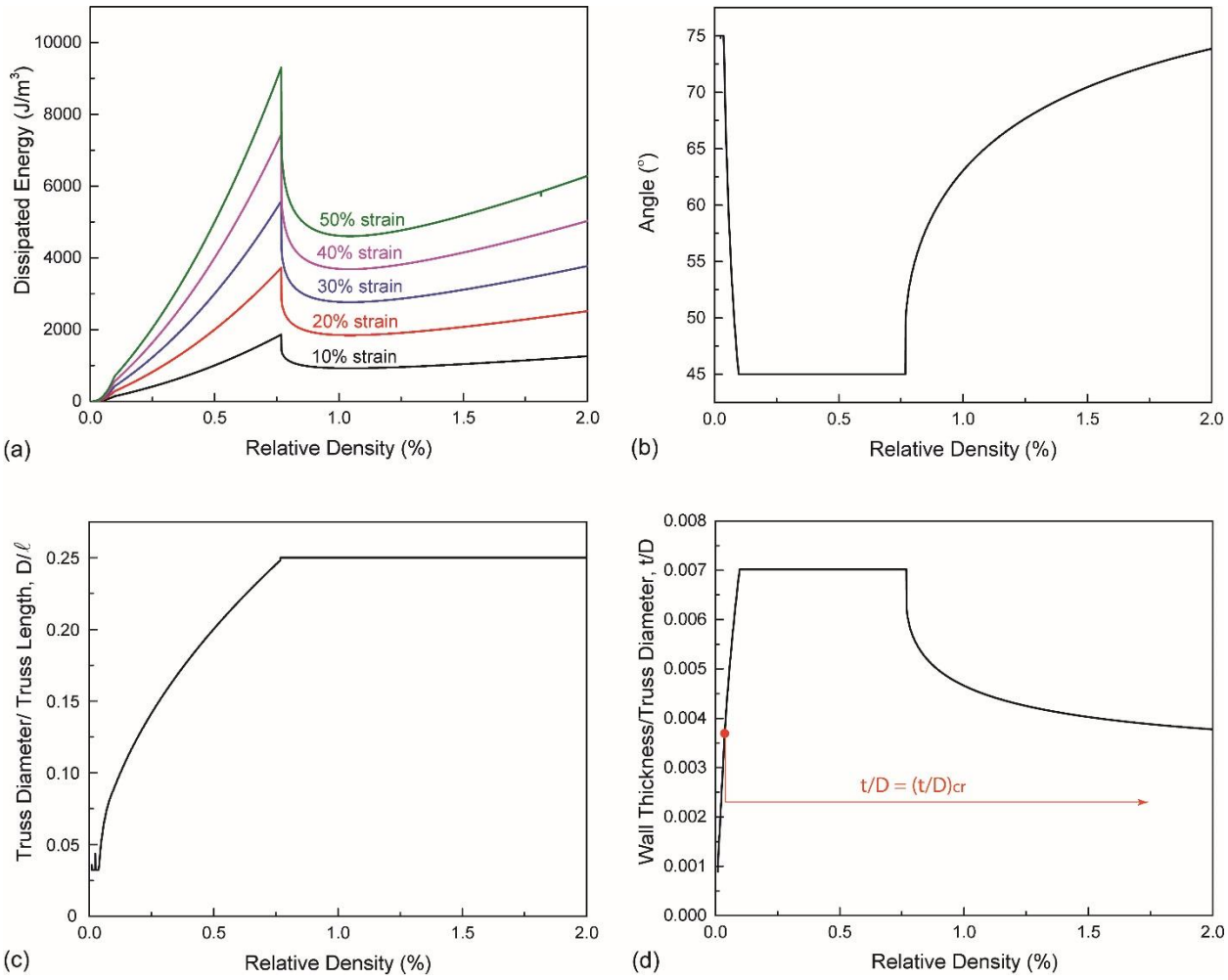

Figure 5.12 (a) Map of achievable energy loss for nickel microlattices as a function of relative density for different compressive strain amplitudes. (b-d) Optimal lattice dimensions.

Initially, t/D increases rapidly with relative density, with the angle constant at its upper bound (75°) and D/ℓ constant at its lower bound (0.032). The dissipated energy is increasing very fast with the relative density. Very soon, the $t/D < (t/D)_{cr}$ constraint becomes active, at which point a further increase in t/D (and hence the energy) is only possible with a steep decrease in angle and an increase in D/ℓ. When the angle reaches its lower bound (45°), t/D reaches a plateau and the density can only increase by further increasing D/ℓ; in this density range, the dissipated energy still increases with density, but at a much lower rate. Finally, at a relative density

of 0.75%, D/ℓ reaches its upper bound (0.25), at which point a further increase in density requires a drop in t/D and an increase in angle; the dissipated energy first drops quickly, and then starts increasing again at a very low rate. The peak in dissipated energy occurs at the relative density of 0.75%, for all applied strain levels.

Figure 5.13a compares the energy dissipation of the existing samples strained to 50% amplitude (samples D-H (Table 5.1)) with the optimal designs. As all experimentally characterized samples have $\theta = 60^o$ (Table 5.1), the optimal results for this constant angle are reported as well. According to the optimization results, for a relative density of 0.17%, the maximum energy loss at 50% strain would be 1,293 J/m^3, which is ~26 times larger than the model predictions for sample G (Table 5.1), which has the same density but different geometry. Conversely, notice that the energy dissipation for sample F (~456 J/m^3), at a relative density of 0.15%, is very close to the prediction for optimal 60^o lattices at that density (511 J/m^3). A comparison of the actual and optimal geometries reveals a striking similarity (Table 5.2), confirming the validity of the analytical model and the optimization process.

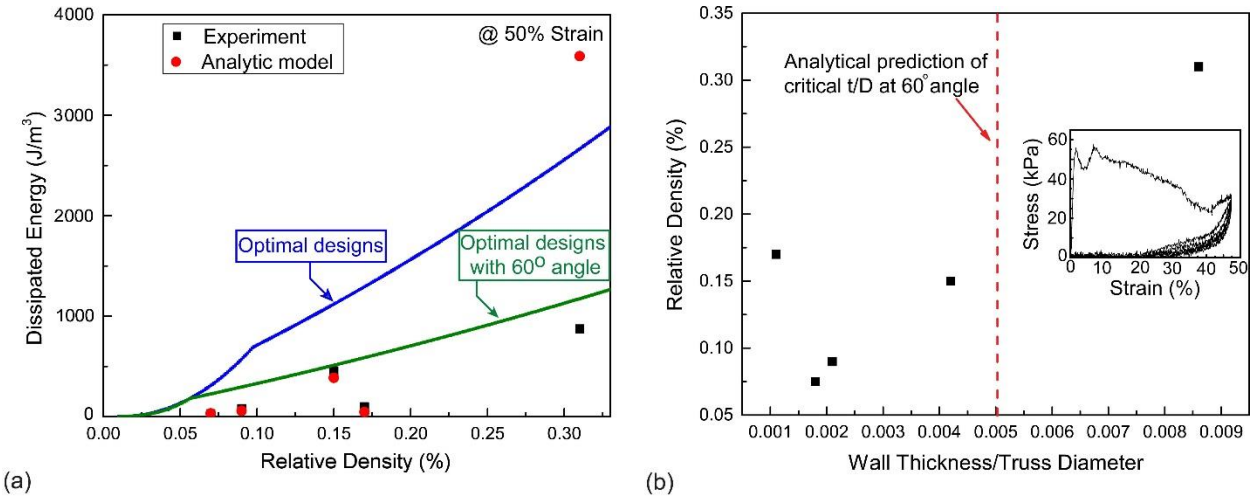

Figure 5.13 (a) Dissipated energy for a number of samples (D-H) of different relative densities (experimental results vs analytical model), compared with the energy that could be dissipated by optimally designed lattices (for the blue line, the lattice member angle is treated as a variable, whereas for the green line, the angle is fixed at 60º). (b) Calculated

relative density vs wall thickness over truss diameter for samples D-H (see Table 5.1 for details). The dotted red line represents the transition between recoverable and unrecoverable behavior. This confirms that the poor agreement between theory and model for sample H ($\bar{\rho} = 0.3\%$) is due to the fact that the sample was not designed to withstand a 50% compressive strain (see stress-strain curve in inset, confirming lack of recoverability).

Notice that the analytical model cannot capture the experimental results for sample H (Table 5.1), at a relative density of 0.31%, and that the prediction for sample H largely exceeds the optimal results at that relative density. This discrepancy is easily explained looking at the dimensions of sample H: the cross-section aspect ratio (t/D) of this sample exceeds the critical value for recoverability (Eq.(1.1)) (see Figure 5.13b). The inset in the figure confirms that sample H does not undergo elastic recovery from a strain of 50%. Once again, these observations reinforce confidence in the model.

Collectively, the optimization results indicate that an energy dissipation per cycle as large as 9,000 J/m^3 is theoretically possible from a nickel microlattice with $\theta = 45^o$, $D/\ell = 0.25$, and $t/D = 0.007$, compressed to a strain amplitude of 50%. This value is ~20 higher than the largest energy dissipation measured to date. However, an increase in dissipation energy does not necessarily guarantee an increase in damping. The next section addresses the optimization of the damping figure of merit, $\Phi = E^{1/3} \tan\delta / \rho$.

Table 5.2 Comparison of the geometries of sample F and the optimal lattice for a relative density of 0.15%.

	Strut angle (°)	Truss thickness/Truss diameter (t/D)	Truss diameter / Truss length (D/ℓ)	Dissipated Energy (J/m^3)
Sample F	60±2	$(4.2\pm0.6)\times10^{-3}$	0.11	456±50
Optimized sample	60	4.9×10^{-3}	0.10	511

5.2.2.2 *Maximization of damping figure of merit, Φ*

Analytical prediction of the damping figure of merit requires reasonable estimates of relative density, Young's modulus and $\tan\delta$. It is well known that analytical models overpredict (often dramatically) both stiffness and strength of hollow microlattices [53], [54]. In this case, the challenge is exacerbated by the substantial structural damage that ultralight samples receive upon large amplitude straining (see Figure 5.1). A crude analytical model will be attempted nonetheless and used to optimize Φ. The goal is a prediction of the trends of the optimal Φ with relative density (and information on the optimal designs), rather than a reliable prediction of Φ itself.

As suggested in [84], [88], $\tan\delta$ for a non-linear dissipating material can be estimated by the shape of the stress-strain curve of a linear viscoelastic material with the same stress and strain amplitudes, $\sigma_{\max}$ and $\varepsilon_{\max}$. The area under the compressive portion of the stress-strain curve (Lissajous figure) for a linear material can be expressed as $W_d = (2\pi/5)\sigma_{\max}\varepsilon_{\max}\sin\delta$. By equating this area to the dissipated energy in a cycle, i.e., $W_d = \Delta U$, and taking $\sigma_{\max}$ as the buckling strength of the lattice, given by [53]:

$$\sigma_{\max} = \frac{2\pi E_s (D/\ell)(t/\ell)^2}{\cos^3\theta\sqrt{3(1-\nu^2)}(1+(D/\ell)\tan\theta/2)} \tag{5.19}$$

an estimate for $\tan\delta$ can be obtained.

As equation (5.19) overpredicts the buckling strength even at the first cycle, and the lattice strength is greatly reduced after the first cycle (Figure 5.1), the resulting estimate for $\tan\delta$ results grossly conservative.

The Young's modulus of the lattice, $E = \sigma/\varepsilon$, can be estimated analytically by normalizing the unit cell stiffness expression (Eq. (5.9)). As $\sigma = P/(2\ell^2\cos^2\theta)$, $\varepsilon = \delta/(2\ell\sin\theta)$ and $K = P/\delta$, where K is the unit cell stiffness given by Eq. (5.12) we obtain:

$$E = \frac{3\pi E_s \sin\theta (D/\ell)^3 (t/\ell)}{\cos^4\theta} \frac{1}{1+\frac{3}{2}(\frac{D}{\ell})^2 \tan^2\theta + 6(1+\nu)(\frac{D}{\ell})^2} \tag{5.20}$$

As ultralight hollow microlattices immediately buckle upon compression, this estimate dramatically overpredicts the stiffness measured by the slope of the stress-strain curve under quasi-static loading [54]. As, it was shown in chapter 4 the agreement is much improved if the stiffness is measured in non-contact methods, e.g., by laser Doppler vibrometry. At any rate, the use of Eq. (5.20) somewhat offsets the over-conservative estimate of $\tan\delta$ discussed above.

For all samples, the relative density is calculated from the geometric parameters in Table 5.1 using Eq.(5.18).

To get a sense of the possible error in using this model to estimate Φ, Table 5.3 compares density, stiffness, strength, energy dissipation, and damping figure of merit extracted from the experiments and the analytical models. As expected, the model consistently overestimates stiffness, density, and strength, while slightly underestimating the energy dissipation. Clearly the actual value of the figure of merit is not reliable number, and tends to underestimate the experimental results by a factor 5-30. However, the trends of Φ with relative density are expected to be reliable.

The damping figure of merit, $\Phi = E^{1/3}\tan\delta/\rho$, was maximized under the same geometrical and physical constraints adapted in previous section (5.2.2.1) (Eq.(5.17)). Figure 5.14 shows the optimal damping figure of merit as a function of relative density. Notice that the results are independent on the compressive strain amplitudes, with all the curves collapsing on a master curve. Interestingly, the optimal geometrical parameters are identical to those for optimal energy dissipation (Figure 5.12).

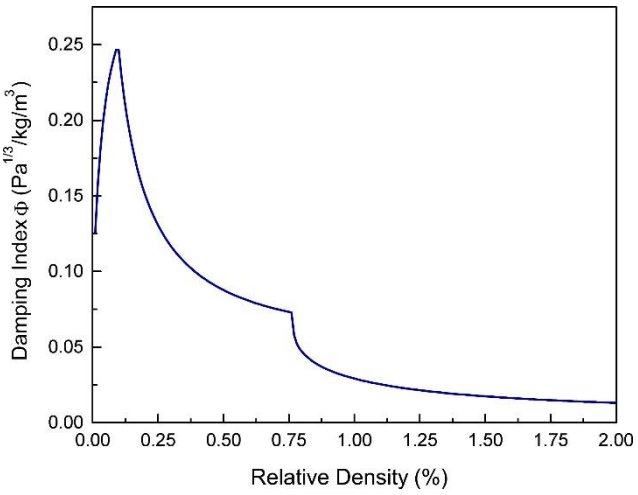

Figure 5.14 Damping figure of merit for optimal designs, as function of relative density. The result is independent on the strain amplitude. Note that the damping performance of buckling-dominated hollow metallic microlattices rapidly drops when the lattice density is increased above ~0.1%.

The damping performance Φ increases very fast with increasing relative density (by increasing D/ℓ and t/D), until the angle reaches its minimum value and t/D saturates to 0.007 (equal to $(t/D)_{cr}$ for $\theta = 45^o$), at a relative density, $\bar{\rho} \sim 0.1\%$. Beyond this point, the angle maintains its minimum value, t/D remains at the critical value and D/ℓ increases, as discussed above; this results in a dramatic decrease in Φ with further increases in relative density (the drop occurs even as the dissipated energy continues to increase, see Figure 5.14). At a relative density, $\bar{\rho} \sim 0.75\%$, D/ℓ reaches its upper bound, after which further increases in density require an increase in the angle and a decrease in t/D; this results in a second sudden drop in the damping figure of merit Φ. Eventually, Φ reaches a plateau, after which it continues to decrease very slowly.

The results clearly show that the damping performance peaks at very low relative density (~0.1%) and dramatically decreases as the density is increased. This confirms that the exceptional buckling-related damping of these novel material systems is limited to the ultralight regime. If

higher relative densities are required (for examples, to meet stiffness and/or strength constraints), additional damping mechanisms should be introduced. One possibility is the fabrication of multi-layer hollow microlattices, where one layer possesses significant intrinsic damping.

Table 5.3 Mechanical properties of different samples cyclically loaded to 50% strain.

Sample	Density (mg/cc)		Compressive modulus (MPa)		Dissipated energy (J/m^3)		Compressive strength (kPa)		Damping figure of merit, $E^{1/3}\tan\delta/\rho$	
	Experiment	Theory	Experiment	Theory	Experiment	Theory	Experiment	Theory	Experiment	Theory
D	13.3±1.3	7.8	0.14±0.05	10.3	82±10	59.3	7±1.5	25	0.77±0.1	0.1
E	7.66±0.7	6	0.3±0.15	8.6	30±7	34	3±0.6	16.6	1.59±0.2	0.11
F	19.48±2	12	0.68±0.15	16.8	456±30	389.2	20.6±2.5	78.2	0.78±0.1	0.168
G	8.817±0.8	13.5	0.22±0.1	44.9	100±10	49	5±1	40	1.53±0.2	0.05

CHAPTER 6. CHARACTERIZATION, MODELING AND OPTIMIZATION OF DAMPING MECHANISMS IN HOLLOW HYBRID MICROLATTICES

In this chapter, we formulate an analytical model for both intrinsic and structural damping mechanisms in the hybrid microlattice materials schematically depicted in Figure 6.1, with the overarching goal of designing lattices with unique combinations of high stiffness, high damping and low density. This chapter is organized as follows: section 6.1 presents an analytical model for stiffness and intrinsic damping mechanism followed by numerical validation and experimental verification; the structural damping mechanism is studied numerically and the mechanical model is presented in section 6.2; the models presented in section 6.1 and section 6.2 are used for optimal design studies in section 6.3.

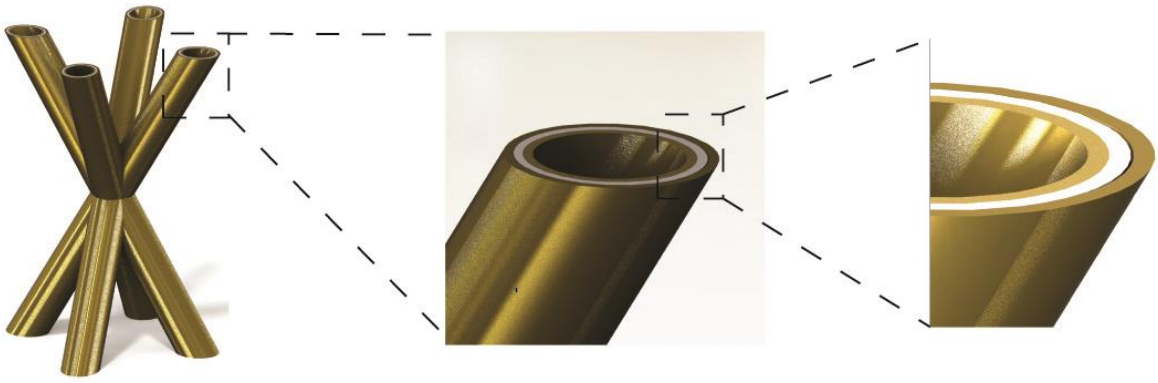

Figure 6.1 Schematic of a hybrid (metal / polymer / metal) lattice.

6.1 Stiffness and Intrinsic Damping Analysis

In this section, a mechanical model is presented to capture stiffness and constrained-layer (intrinsic) damping (section 6.1.1), and the accuracy of this model is validated by finite element

simulations (FE) in section 6.1.2. Finally, experimental measurements performed to confirm the accuracy of the model are presented in section 6.1.3.

6.1.1 Modeling stiffness and intrinsic damping

A free body diagram of a bar within the microlattice material is depicted in Figure 6.2. Notice that the bars within the lattice experiences a combination of axial compression, transverse shear, and bending moment.

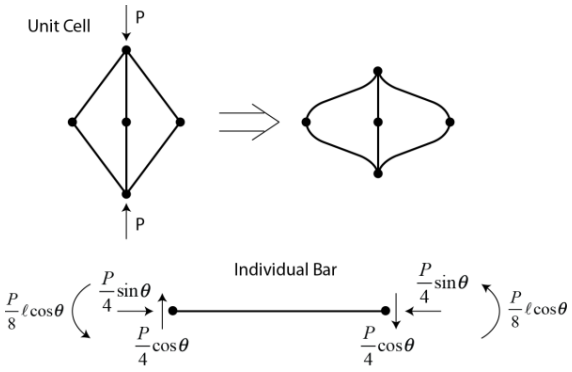

Figure 6.2 Schematic of the deformation of a unit cell of the lattice under external compression, and free-body diagram of a single bar. Note that each bar experiences a combination of axial compression, bending moment, and shear load.

The correspondence principle is used to model stiffness and damping capacity of hybrid lattices with a constrained lossy layer. The energy stored in the entire unit cell of microlattice materials, upon global compression, consists of axial, shear and bending contributions. Each of these energy terms can be readily expressed in analytical form. By imposing that the energy stored in the unit cell is equal to $U = \frac{1}{2} P\delta$, with *P* being the external load and δ the displacement, the unit cell stiffness (defined as $k = P/\delta$) can be calculated and properly rescaled to obtain the effective Young's modulus of the lattices (which in this case is a complex number). The end result is:

$$E^*_{unit\_cell} = \frac{3\pi D^3 t_{total} E^*_{voigt} \sin\theta}{\ell^4 \cos^4\theta}\left(1+\frac{3}{2}\left(\frac{D}{\ell}\right)^2 \tan^2\theta + 3\frac{E^*_{voigt}}{G^*_p}\frac{t_{total}}{t_p}\left(\frac{D}{\ell}\right)^2 / \left(1+\frac{t^i_m + t^o_m}{t_p}\frac{G_m}{G^*_p}\right)\right)^{-1} \quad (6.1)$$

where D is diameter, ℓ is length, and θ is truss angle for each bar; t^i_m, t^o_m, t_p, and t_{total} are inner metal layer thickness, outer metal layer thickness, polymer layer thickness, and the total thickness of all three layers, respectively. Note that in the analytical model the thickness of inner metal, outer metal, and polymer are all assumed to be uniform. When the bulk modulus of polymer is very large compared to its shear modulus (hence the material is incompressible), the shear modulus of the polymer is $G^*_p = \frac{E^*_p}{3}$. The shear modulus of metal is defined as $G_m = \frac{E_m}{2(1+\nu)}$. Finally, E^*_{voigt} is the effective longitudinal Young's modulus of the hybrid wall, i.e.:

$$E^*_{voigt} = E_m \frac{t^i_m + t^o_m}{t_{total}} + E^*_p \frac{t_p}{t_{total}} \quad (6.2)$$

where E^*_p, and E_m are the Young's modulus of the polymer (a complex number) and metal, respectively.

Since the effective Young's modulus is a complex number ($E^*_{unit\_cell} = E'_{unit\_cell} + iE''_{unit\_cell}$), the intrinsic damping coefficient can be extracted from the storage modulus (E'_{unit_cell}) and loss modulus (E''_{unit_cell}) as:

$$\tan\delta = \frac{\mathrm{Im}(E^*_{unit\_cell})}{\mathrm{Re}(E^*_{unit\_cell})} = \frac{E''_{unit\_cell}}{E'_{unit\_cell}} \quad (6.3)$$

The density of these lattices is expressed by simple geometric consideration as:

$$\rho = \frac{2\pi}{\sin\theta\cos^2\theta}\frac{D}{\ell}\left(\rho_m \frac{t^i_m + t^o_m}{\ell} + \rho_p \frac{t_p}{\ell}\right) \quad (6.4)$$

where ρ_m is the density of metal and ρ_p is the density of the polymer. Note that any mass accumulation at the nodes is neglected.

6.1.2 Numerical validation of stiffness and intrinsic damping models

Numerical analyses were performed using the commercial Finite Element package ABAQUS both on a single bar and a unit cell level lattices to validate the accuracy of the analytical model.

The nickel (metal face sheets) with $E_m = 210\text{GPa}$, $\rho_m = 8900\text{kg/m}^3$, and $\nu = 0.3$ was modeled as a linear elastic material, while the parylene (polymeric core) with $E_p^* = 1.358 + 0.3396i$ GPa, $\tan\delta = 0.25$, $\rho_p = 1200\text{kg/m}^3$, and $\nu = 0.49$ was modeled as a viscoelastic material in frequency domain. The long term Young's modulus of parylene was assumed to be $E_\infty = 0.37\text{GPa}$, according to the measurements of Andressen [89]. The steady-state-dynamics-direct algorithm is used to capture the behavior of hybrid lattices with polymeric layer as a lossy material (with Young's modulus being a complex number). In order to verify the accuracy of the steady-state-dynamics-direct algorithm, classic composite topologies (Voigt and Reuss) were simulated with ABAQUS, and the results were compared with both analytical models. According to the correspondence principle, the Voigt composite modulus is calculated from Eq. (6.2) and the Reuss shear modulus is expressed as:

$$\frac{1}{G_t^*} = \frac{t_p / t_t}{G_p^*} + \frac{(t_m^i + t_m^o)/t_t}{G_m} \tag{6.5}$$

A composite lattice (nickel / parylene / nickel) with length and width of $3.5\mu m$, polymer thickness of $t_p = 2.5\mu m$, and inner and outer metal thickness of $t_m^i = t_m^o = 0.5\mu m$ is modeled in ABAQUS both under shear and compression.

	Analytical Model	FE Model
Voigt Model	$E^*_{voigt} = 61.78 + 0.0535i$ GPa	$E^*_{voigt} = 61.75 + 0.0541i$ GPa
Reuss Model	$G^*_{Reuss} = 1.161 + 0.0347i$ GPa	$G^*_{Reuss} = 1.168 + 0.0349i$ GPa

Table 6.1 Comparison between analytical and FE models for Voigt and Reuss composites.

Analytical and FE models are in very good agreement (Table 6.1), confirming the accuracy of the steady-state-dynamics-direct algorithm in modeling the frequency-domain viscoelastic response of materials.

To validate the analytical model proposed in Eq. (6.1) with Finite Element simulations, two nickel / parylene / nickel samples (sample A was slender and sample B was stubby) were modeled in ABAQUS, at two different scales: single bar and single unit cell level, to isolate the effects of the nodal geometry.

Note that for FE simulation, shell elements are best suited for sample A, due to its slender nature, and similarly, solid elements are best suited for sample B due to its stubby nature.

As mentioned, shell elements are used to model sample A with $\ell = 4000\mu m$, $D = 500\mu m$, $\theta = 60^o$, $t_p = 2.5\mu m$, and $t_m^i = t_m^o = 0.5\mu m$. The Young's modulus of the lattice was extracted from the simulations and compared with the analytical prediction from Eq. (6.1) and the results are presented in Table 6.2. The results indicate that the analytical model can capture the behavior of a single bar accurately; however, it is over-estimating the unit cell stiffness. The same discrepancy was also observed in single layer metallic lattices with the same aspect ratios as that

of sample A in previous studies [54]. We attribute this discrepancy to the fact that simple beam model does not capture the effects of the nodes.

Sample B with $\ell = 1000\mu m$, $D = 250\mu m$, $\theta = 60^o$, $t_p = 16.66\mu m$, and $t_m^i = t_m^o = 4.16\mu m$ was modeled using solid elements. The Young's modulus of the lattice was extracted from the simulations and compared with the analytical prediction from Eq. (6.1) and the results are presented in Table 6.2. The results indicate that the storage modulus captured by the FE simulation for the single bar and single unit cell are very close; however, the analytical model is under-predicting the modulus in both simulations by ~19.5%. We attribute this discrepancy to the sample geometry: i.e. the wall thickness in sample B ($t_t / D = 0.1$) violates the thin-wall assumption in the analytical model. On the other hand, the loss modulus of the lattice captured by the FE simulation on the unit cell mesh is ~3x higher than from the single bar model. We attribute this difference to the nodal geometry: i.e. the polymer accumulates large shear strain in the nodal region of this stubby sample, which results in higher loss than single bar simulations. Figure 6.3 depicts the maximum principle strain in the polymeric layer of samples A and B, which clearly shows higher nodal strain in sample B compared to sample A.

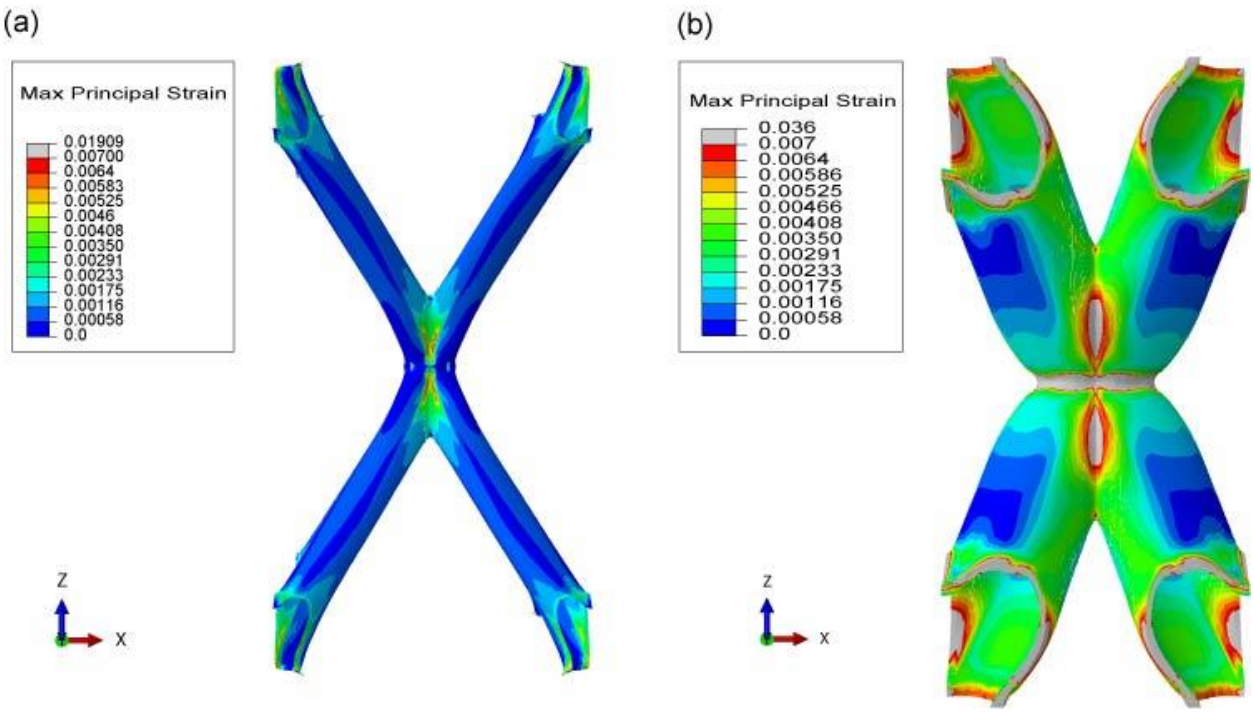

Figure 6.3 Maximum principle strain of parylene layer in (a) sample A and (b) sample B under axial compression

Altogether, the results of the FE simulation confirm that the analytical model predicts the single bar behavior accurately when the total thickness is small relative to the diameter. Furthermore, when it comes to the unit cell level, although the analytical model shows some discrepancies in predicting the storage modulus, the trend of the discrepancies is the same as in single layer lattices [54]. The model predicts the loss modulus accurately when ℓ / D is large and the node is small relative to the whole unit cell (sample A) but is under-predicting when ℓ / D is small and the node is large relative to the whole unit cell (sample B).

Table 6.2 Comparison of Young's modulus captured from analytical model, single bar, and single unit cell FE simulations.

	Finite Element young's modulus single bar (Pa)	Finite Element young's modulus unit cell	Analytical model young's modulus
Sample A	$E^* = 11.40 \times 10^6 + 9.8 \times 10^3\, i$	$E^* = 5.17 \times 10^6 + 3.47 \times 10^3\, i$	$E^* = 11.56 \times 10^6 + 9.89 \times 10^3\, i$
Sample B	$E^* = 2.58 \times 10^9 + 2.2 \times 10^6\, i$	$E^* = 2.74 \times 10^9 + 7.54 \times 10^6\, i$	$E^* = 2.06 \times 10^9 + 1.38 \times 10^6\, i$

6.1.3 Experimental verification of intrinsic damping

Resonant measurements at infinitesimal strains were performed to capture the intrinsic damping mechanism of the hybrid lattices at two different length scales; single bar, and single unit cell. A half layer tetrahedral hybrid hollow microlattice manufactured by HRL laboratories is used in these experiments. Therefore, the analytical models are modified for tetrahedral lattices and compared with the experimental results. Note that, the results of these comparisons can be applied to the octahedral lattices as well since they both exhibit the same mechanisms.

All experiments were carried out with a Laser Doppler Vibrometry (PSV-500, Polytec GmbH, Irvine, CA) depicted in Figure 6.4a . The single bar measurement is used to investigate the accuracy of the analytical model and the single unit cell measurement is used to study the effects of nodes on the intrinsic damping.

A single bar was extracted from a hybrid lattice and press-fitted to the aluminum base to create a fixed boundary condition (cantilever bar) as depicted in Figure 6.4b. The bar was assembled on top of a shaker (Labworks Inc. ET-132-2) by using petro mounting wax. The aluminum base was oscillated via a shaker with a FFT sinusoidal signal at a very low amplitude, sweeping the frequency within the range of 0-15kHz. The velocity of the aluminum base and hybrid bar were monitored with the Doppler Vibrometer in scanning mode (to identify the modal shapes).

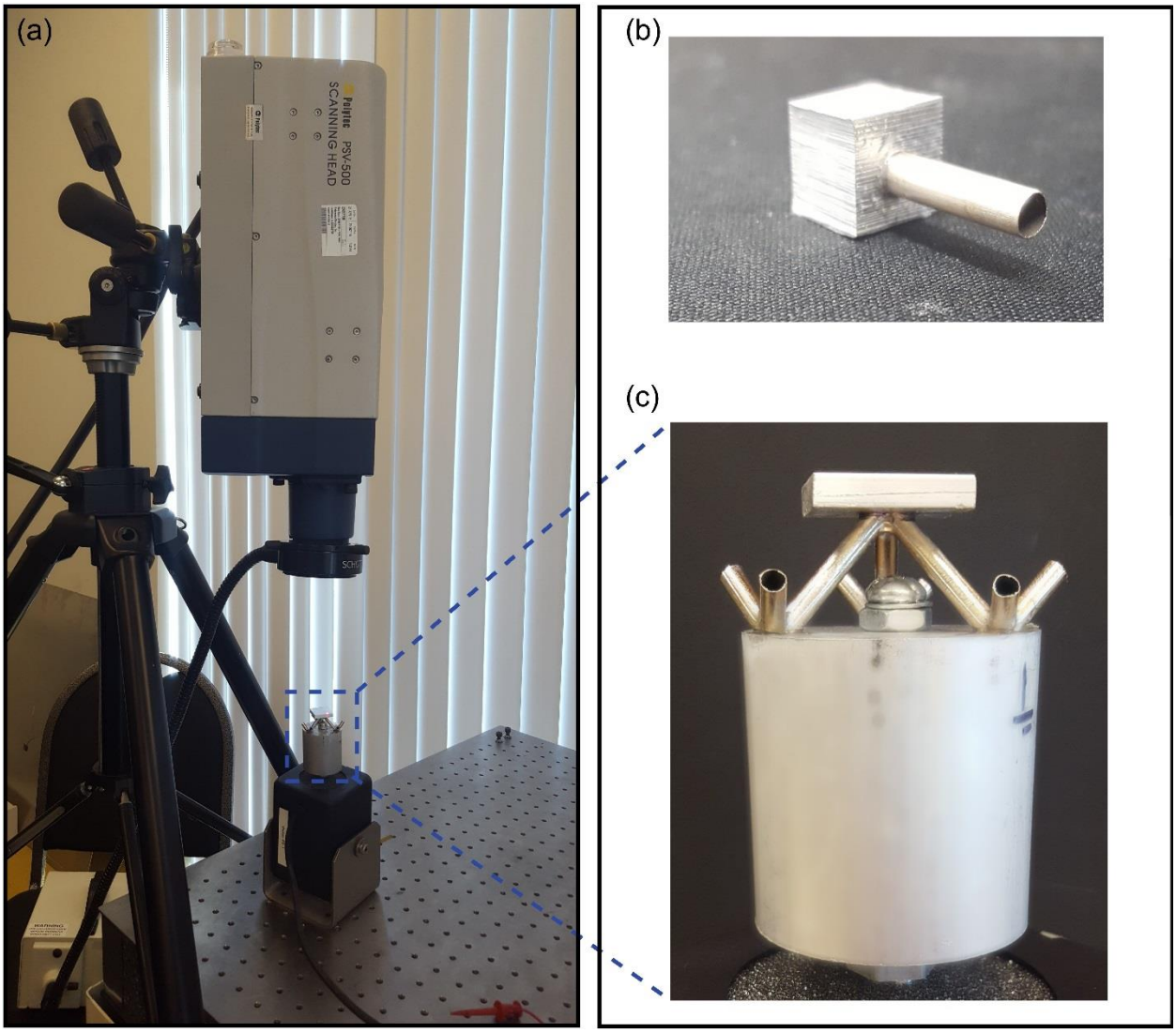

Figure 6.4 (a) Laser Doppler Vibrometry (PSV-500); (b) single bar in cantilever mode; (c) half tetrahedral unit cell bounded between two aluminum facesheets.

The response of the base plate and the bar is depicted in Figure 6.5a and b, respectively. An eigenmode was detected at ~13kHz with an out-of-plane axial mode for the aluminum base. To eliminate the effects of aluminum base excitation, *H1* transfer function, $H1 = \frac{\mathrm{Y}(\omega)}{X(\omega)}$, is used where $X(\omega)$ is the average response of the aluminum base and $Y(\omega)$ is the response of individual points on the bar with respect to the $X(\omega)$ excitation. The frequency response of every single point on the bar is calculated by using the above transfer function and the response of a single point is

depicted in Figure 6.5c. Note that in the previous measurements on metallic samples (section 5.1.3), the H1 transfer function was not used to extract the damping coefficient. This was due to the fact that the natural frequencies of the sample were below the resonance frequency of piezoelectric actuator; therefore, the excitation was uniform and the response was purely originating from the materials. However, in this measurement the natural frequencies of the sample are very close to the resonance mode of the shaker; therefore, the results is a combination of responses of the shaker and the hybrid bars, which need to be decoupled.

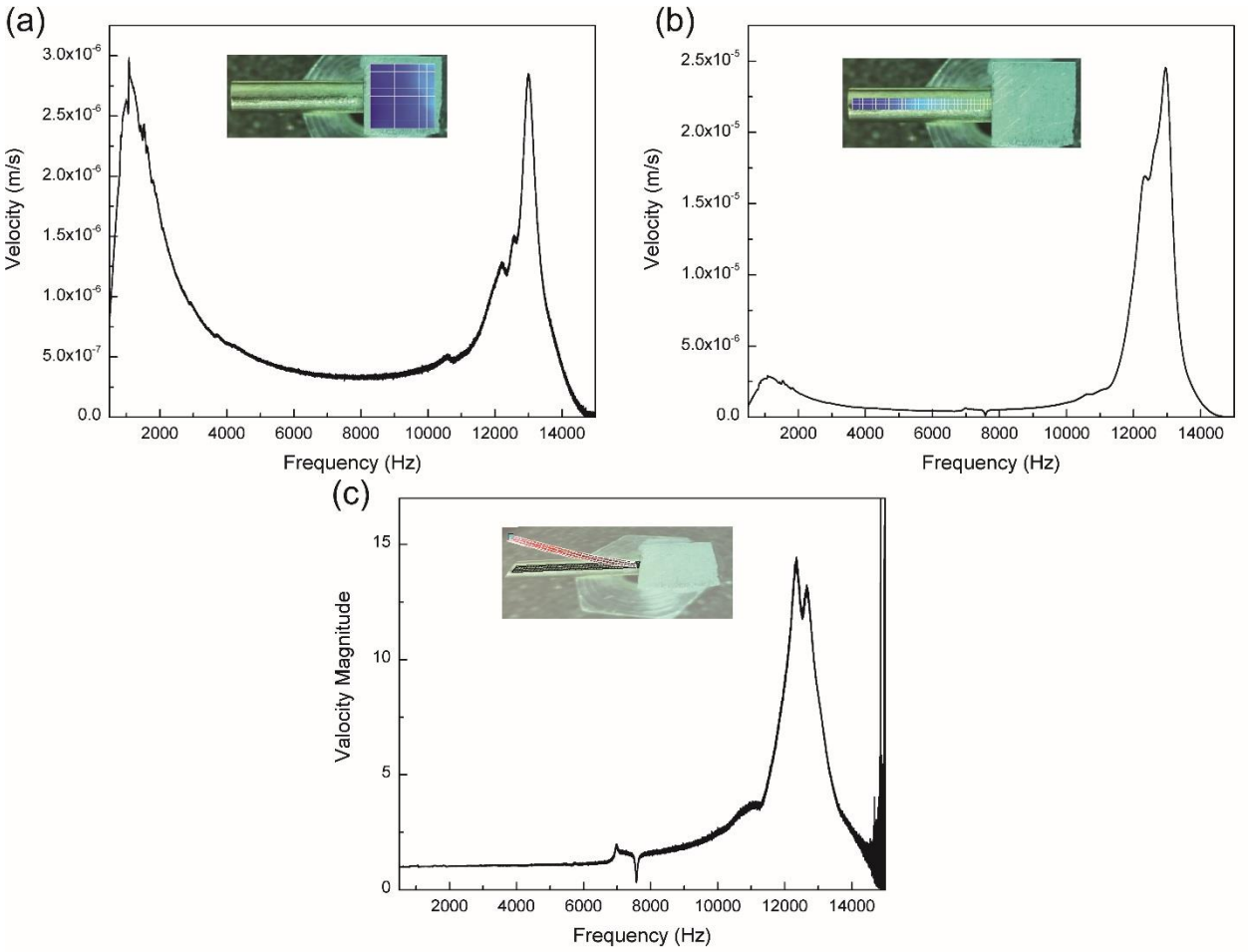

Figure 6.5 Frequency response of (a) aluminum base; (b) hybrid bar with respect to the aluminum base excitation captured by Laser Doppler Vibrometry; and (c) the result of H1 transfer function of a single bar.

As Figure 6.5c indicates, two modes are coupled at ~12kHz frequency with a first bending mode shape (inset in Figure 6.5c). A Gaussian function is used to decouple these modes from each other and the result is depicted in Figure 6.6.

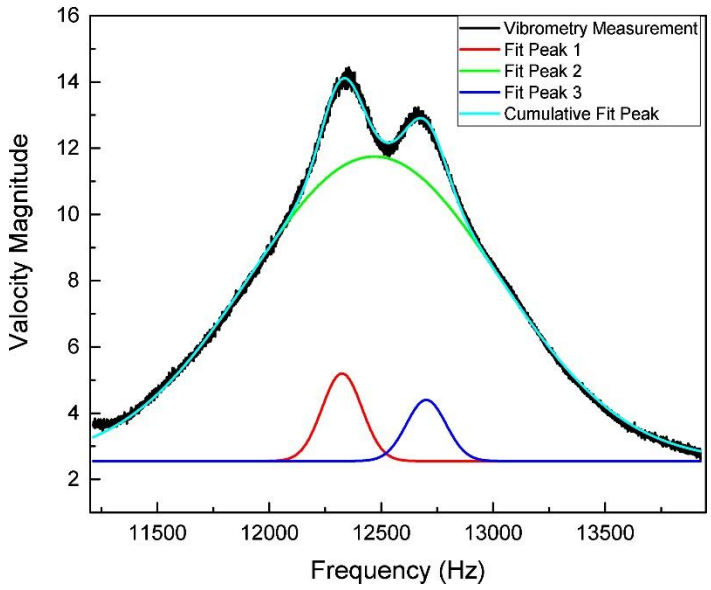

Figure 6.6 Decoupling the two frequency modes by using Gaussian function.

Two different methods can be used to capture the damping of the structure from the resonant response: (i) half bandwidth method and (ii) structural damping method. In the first method, the loss factor η is extracted from the ratio of the resonance peak width (measured at an amplitude of $1/\sqrt{2}$ of the peak amplitude) to the resonance frequency [81]. The second method is useful when the structure is damped by internal friction [80]. This damping can be calculated by equating the work done by external harmonic excitation ($F(t) = Ake^{i\omega t}$ which A is a constant and k is the spring constant) of the structure to the energy dissipated per cycle of vibration ($\Delta E_{cyc} = \int_{cyc} F dx = \int_0^{2\pi/\omega} F\dot{x}dt$). Assuming the response to this harmonic excitation is $x(t) = A|G(i\omega)|e^{i(\omega t-\phi)} = Xe^{i(\omega t-\phi)}$, the energy dissipated per cycle is:

$$\Delta E_{cyc} = -kA^2 \left|G(i\omega)\right| \omega \int_0^{2\pi/\omega} \cos\omega t.\sin(\omega t - \phi)dt = m\omega_n^2 A^2 \left|G(i\omega)\right| \pi \sin\phi \tag{6.6}$$

where $\sin\phi = \frac{c\omega}{m\omega_n^2}\left|G(i\omega)\right|$; therefore, the energy dissipated per cycle can be simplified to $\Delta E_{cyc} = c\pi\omega X^2$ where c is viscous damping coefficient. Moreover, experiments performed using a variety of materials show that energy loss per cycle due to internal friction is proportional to the square of the displacement amplitude, $\Delta E_{cyc} = \alpha X^2$ [80]. Under these circumstances the equation of motion of the structure can be written as:

$$m\ddot{x}(t) + \frac{\alpha}{\pi\omega}\dot{x}(t) + kx(t) = F(t) = Ake^{i\omega t} \tag{6.7}$$

Since $\dot{x} = i\omega x$ and $\omega_n^2 = k/m$, equation (6.7) can be rewritten as:

$$\ddot{x}(t) + \omega_n^2(1 + i\gamma)x(t) = \omega_n^2 Ae^{i\omega t} \tag{6.8}$$

where $\gamma = \frac{\alpha}{\pi k}$. The steady state solution of Eq.(6.8) is $x(t) = \mathrm{Re}[A\left|G^*(\omega)\right|\mathrm{e}^{i(\omega t - \phi^*)}]$ where $G^*(\omega) = \frac{1}{1-(\omega/\omega_n)^2 + i\gamma}$ is the equivalent of the frequency response of the structural damping.

For the sample in the test, both methods generate identical results. Figure 6.7 shows the results of the curve fit method on the two curves captured from decoupling the modes. The extracted damping ratio form both peaks are very close to each other and is equal to $\eta \sim 0.02$.

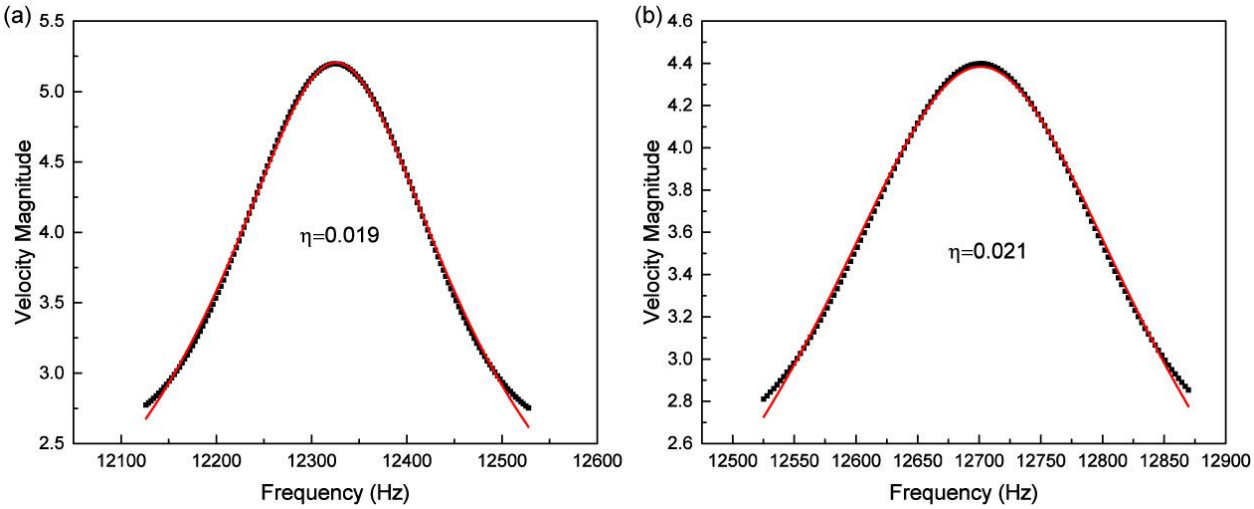

Figure 6.7 Extraction of the damping coefficient from the frequency response of a hybrid sample captured by Laser Doppler Vibrometry, by using the curve fit method (a) first curve; (b) second curve.

Frequency extraction (also known as linear perturbation analysis) was performed on a single bar with the same dimensions of the bar in the test ($\ell = 15.59\text{mm}$, $D = 3.2\text{mm}$, $t_m^i = 19.5\mu\text{m}$, and $t_m^o = 15.1\mu\text{m}$) in ABAQUS/Standard. The thickness of the polymer was swept between $t_p = 4.7 - 30\mu\text{m}$ to capture the effects of the polymer layer on the natural frequencies of the single bar. The four lowest vibration modes and corresponding eigen frequencies were obtained via eigenvalue extraction. In the sample with $t_p = 4.7\mu\text{m}$, the first and the second modes are distortion modes with identical frequencies of ~10kHz; the third mode and the fourth modes are first in-plane and first out-of-plane bending modes respectively, with identical frequencies of ~13kHz. By increasing the polymer layer thickness, the first and the second modes are switching with the third and the fourth modes and the frequencies of the bending modes are decreasing. Therefore, the two bending modes (in-plane and out-of-plane) that were captured in FE simulations are actually the two coupled modes in the experiment. The difference in the frequencies of these two modes is due to the manufacturing defects (e.g. non-uniformity of the polymer layer).

According to the modified analytical model presented in section 6.1.1, for a hybrid cantilever beam with a dimension of $\ell = 15.59\text{mm}$, $D = 3.2\text{mm}$, $t_m^i = 19.5\mu\text{m}$, and $t_m^o = 15.1\mu\text{m}$, the intrinsic damping for samples with $t_p = 4.7\mu\text{m}$, $t_p = 30\mu\text{m}$, and, $t_p = 100\mu\text{m}$ are $\eta = 2.7\times10^{-4}$, $\eta = 0.0018$, and $\eta = 0.005$, respectively. Comparing the experimental measurement ($\eta \sim 0.02$) and the prediction by analytical model shows at least 4x difference in intrinsic damping. In the analytical model, the metal damping was neglected and only the intrinsic damping of the polymer was studied; however, a study on damping of nickel hollow microlattice materials (chapter 5) indicates that the nickel structure possesses some intrinsic damping as well. Therefore, to verify the analytical model, a single layer nickel bar with the same dimensions ($\ell = 15.59\text{mm}$, $D = 3.2\text{mm}$, $t_m \sim 40\mu\text{m}$) was tested with a Laser Doppler Vibrometry to capture its intrinsic damping. The experiment was repeated with exact same conditions as explained above. The extracted damping coefficient for the single layer nickel bar is $\eta = 0.016$ for the first bending mode. The difference between the damping of hybrid bar and single layer nickel bar is ~ 0.004 which is within the range of analytical model predication when the polymer thickness varies between $t_p = 4.7 - 100\mu\text{m}$ (since the polymer layer thickness is not uniform throughout the sample, a damping within the range of thickness is acceptable).

Similarly, a single half unit cell is extracted from hybrid microlattice structure and bounded between two aluminum face sheets (Figure 6.4c). The bottom face sheet is a 5cm thick aluminum rod (which is chosen based on FE simulations to prevent having any eignmodes below a resonance frequency of the lattice) and a top face sheet is a $20\text{mm}\times20\text{mm}\times4\text{mm}$ plate which is ~10x heavier than the lattice (Figure 6.4c). The bottom plate was excited by the shaker with frequencies within the range of 0-10kHz and the top and bottom plates were scanned by Laser Doppler Vibrometry

and their responses were captured. The curve fit method is used to extract the damping coefficient of the microlattice. The result of curve fit is reported in Figure 6.8a. The damping of half unit cell hybrid lattice is $\eta = 0.018$.

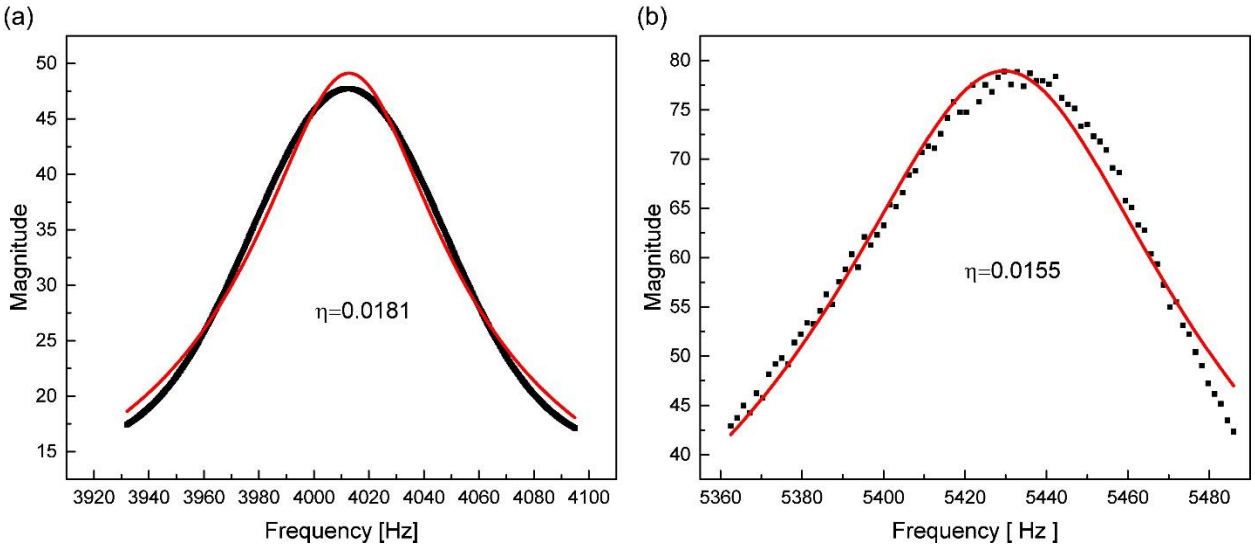

Figure 6.8 Extraction of damping coefficient from the frequency response of (a) half hybrid tetrahedral unit cell and (b) half nickel tetrahedral unit cell microlattices captured by Laser Doppler Vibrometry.

The same procedure was repeated for a half unit cell nickel lattice with $t_m \sim 40\mu m$ and a damping coefficient of $\eta = 0.015$ (Figure 6.8b). The difference between the intrinsic damping of the hybrid half unit cell and the nickel half unit cell is ~0.003, which is predicted accurately by the analytical model. According to these experiments, the damping of microlattices has been increased by 20% by adding the constrained polymeric layer. It is worth mentioning that for this specific lattice, the damping coefficient of a single bar and half unit cell are very close; however, according to FE simulations, the damping coefficient can be increased by stacking up several unit cells due to the effects of the nodes.

6.2 Structural Damping Analysis

As discussed in the previous chapters, the mechanical response of hollow lattice materials is a very strong function of their relative density: (1) For dense lattices, the typical plastic deformation plateau is observed with no recoverability. Therefore, these lattices only have intrinsic damping (intrinsic metal layer damping and constrained-layer damping) at small strains as their damping mechanism. (2) For ultralight lattices, where the thickness to diameter ratio of the bars are very small, a unique pseudo-super-elastic behavior is observed whereby full recoverability is achieved upon very large straining (in excess of 50%). In chapter 5.2 we have shown that the pseudo-super-elastic behavior in ultralight regime is due to buckling of the bars upon compression. Therefore, the ultralight lattices have two different damping mechanisms: intrinsic damping at any strain and structural damping due to buckling of the bars at large strain. In this section the structural damping mechanism for hybrid ultralight microlattices is studied. Section 6.2.1 presents a numerical analysis of the existence of this damping mechanism in hybrid hollow microlattices and section 6.2.2 presents an analytical model for it.

6.2.1 Buckling related energy dissipation mechanism

In chapter 4, a unique form of structural damping under large compressive strain was identified for metallic hollow microlatices and shown to be related to the local buckling of individual bars. In this section, we show that hybrid hollow microlattices also exhibit the same behavior under compressive strain; with a caveat that the wall thickness to diameter ratio be kept below the necessary limit to ensure that no plastic deformation occurs upon local buckling of the members and large rotations about the kinks.

This mechanism can be clearly elucidated with a simple FE simulation of a single hybrid bar loaded in cantilever mode (Figure 6.9a). To address convergence issues, a dynamic simulation

is performed in ABAQUS/Explicit under displacement control. In order to have negligible inertia effects, a very small strain rate was chosen and the kinematic energy was verified to be very small compared to the elastic energy during the entire simulation; additionally, a smooth function for displacement was used to prevent sudden shocks at the beginning of the simulation. A hollow cylinder with the diameter of 1mm, length of 4mm, polymer wall thickness of 100nm and nickel wall thickness of 538nm was chosen for the simulation. One end of the cylinder is fully clamped and the other end is displaced vertically by 200nm with a displacement rate of 0.2m/s and then unloaded to its original position. In the simulation, a nickel layer with Young's modulus of 210GPa, Poisson ratio of 0.3, yield strength of 2.5GPa, and density of 8900kg/m^3 was used; the polymer layer has Young's modulus of 1.4GPa, Poisson ratio of 0.45, yield strength of 26MPa, and density of 1040kg/m^3. Both materials are modeled as elastic perfectly plastic. Since we are not interested in the intrinsic damping behavior in this simulation, no viscoelastic properties are inserted. A 4-node shell element was used with reduced integration hourglass control and finite membrane strain (S4R). The cross-section at the free end is maintained circular during the entire cycle. Self-contact (hard, frictionless) is imposed on the cylinder to realistically capture large post-buckling deformation.

The shape at the end of the loading cycle together with contours of the Von Mises stress are presented in Figure 6.9a. The load displacement relation for a cylinder is shown in Figure 6.9b. After a linear-elastic response, the cylinder buckles with a sudden and almost complete drop in the load. It continues to deform fairly linearly thereafter, albeit with much reduced stiffness. Upon unloading, the cylinder retraces the post-buckling loading curve until the buckling point, and then snaps back on the pre-buckling curve. During the entire cycle, the cylinder dissipates an amount of energy given by the nearly triangular shaded area shown in Figure 6.9b.

In a bulk lattice under compression, a large number of bars can dissipate energy through this mechanism. The energy dissipated by the entire lattice in a cycle is roughly given by the sum of these contributions for all the bars that buckle. This energy dissipation can be approximately modeled using classic local buckling theory (discussed in the next section). The same behaviors have been observed for nickel based hollow microlattice materials; for those systems, the experimental data agreed remarkably well with the simple analytical model as shown in chapter 5.

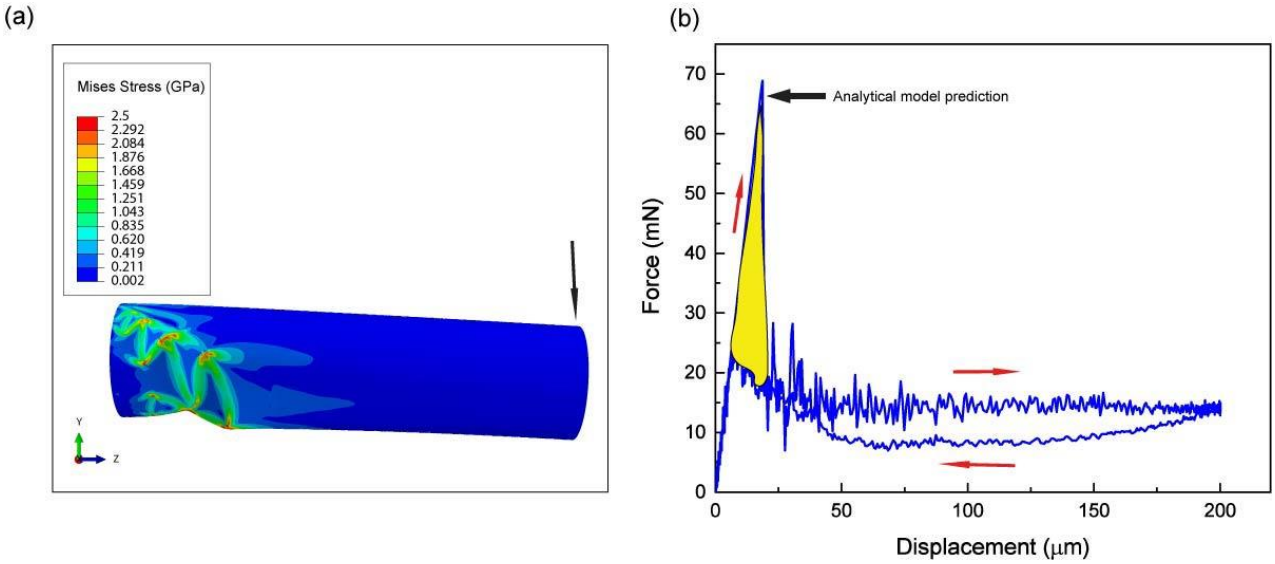

Figure 6.9 (a) Finite element simulation of a clamped hollow cylinder loaded in a cantilever mode. (b) Load–displacement curve, showing the energy dissipation in a cycle.

Before introducing the mechanical model, it is worth noting that not all the bars show the same behavior as shown in Figure 6.9. According to the previous studies [52] for single phase lattices, a simple condition can be derived to ensure that plastic deformation do not ensue during the large bar rotation induced by large compression of the cycle. This condition is here extended to hybrid lattices, and can be expressed as:

$$\frac{t_m^i + t_m^o}{D} < \frac{0.25}{\theta - \sin^{-1}((1-\varepsilon_{\max})\sin\theta)} \cdot \frac{\sigma_m}{E_m} \tag{6.9}$$

where σ_m is the yield strength on the metal layer and $\varepsilon_{\max}$ is the maximum compressive strain imposed on the lattice. Note that since the yield strain of polymer is higher than the metal, the metallic layer in the bar is first going through plastic deformation.

6.2.2 Mechanical model of buckling related energy dissipation mechanism

As shown in the previous section, the hybrid hollow microlattice materials, with certain geometry, under large compressive strain, show full recoverability. During the unloading process, such structures dissipate energy which we are going to model in this section.

As free-body diagram of a bar in the microlattice (depicted in Figure 6.2) shows, each bar in a lattice under compression experiences a combination of axial compression, bending moment, and transverse shear. Neglecting the shear load with respect to the axial and bending moment, and the effects of polymer layer, the maximum normal compressive stress $\sigma_{\max}$ on the metal layer of the bar in the lattice can be found as a function of the compressive load applied on a single unit cell, *p*, as:

$$\sigma_{\max} = \frac{p}{4\pi D(t_m^i + t_m^o)}(\sin\theta + \frac{2\ell}{D}\cos\theta) \tag{6.10}$$

The bar buckles when the maximum stress in the bar equals the critical local buckling stress and the local buckling occurs by shell compression near the clamped end. As shown in [90], in sandwich-wall hollow cylinders with small relative ratio of the polymer thickness over the diameter of the bar, the local buckling stress can be written as:

$$\sigma_{lb} = \frac{2E_m}{\sqrt{1-\upsilon_m^2}}\frac{r_g}{R} \tag{6.11}$$

where:

$$\frac{r_g}{R} = \frac{t_p + t_m}{D}\sqrt{1 + \frac{1}{3}\left(\frac{t_m}{t_p + t_m}\right)^2} \tag{6.12}$$

and E_m and ν_m are Young's modulus and Poisson ratio of the metal layer. This model assumes that the thicknesses of the inner and outer metal layers are identical ($t_m^i = t_m^o = t_m$). The optimization results also confirm that having the same metal thickness outside and inside of the polymer yields the optimal solution. By equating Eq.(6.10) and Eq.(6.11), the buckling strength of sandwich hollow bars can be expressed as:

$$P_{bar}^{lb} = \frac{P_{cr}}{4} = \frac{2\pi E_m D^2 t_m}{\sqrt{1-\nu^2}\,\ell\cos\theta\left(1 + \frac{D}{\ell}\frac{\tan\theta}{2}\right)}\left(\frac{r_g}{R}\right) \tag{6.13}$$

This model was verified by the FE simulation on a single bar loaded in cantilever mode shown in Figure 6.9b. The FE simulation predicts a critical buckling load of 64.4mN while the analytical model prediction is 66.6mN, clearly showing the accuracy of this model. On the other hand, the stiffness of one bar in the lattice can be derived from Eq. (6.1) as:

$$K_{bar} = \frac{K}{2} = \frac{3\pi D^3 t_t E_{voigt}^*}{2\ell^3\cos^2\theta}\left(1 + \frac{3}{2}\left(\frac{D}{\ell}\right)^2\tan^2\theta + 3\frac{E_{voigt}^*}{G_p^*}\frac{t_t}{t_p}\left(\frac{D}{\ell}\right)^2 \Big/ \left(1 + \frac{t_m^i + t_m^o}{t_p}\frac{G_m}{G_p^*}\right)\right)^{-1} \tag{6.14}$$

Assuming the entire elastic energy dissipated upon buckling, the energy loss from each bar can roughly modeled as:

$$\Delta E_{bar} = \frac{p_{bar}^{lb\ 2}}{2K_{bar}} \tag{6.15}$$

The number of bars in the whole lattice is given by $N_b = 16 n_x n_y n_z$, where n_x, n_y, and n_z are the number of unit cells in *X*, *Y*, and *Z* directions, respectively. The dimensions of the lattice are related to the dimensions of the unit cell by $L = 2\ell\cos\theta n_y$, $H = 2\ell\sin\theta n_z$, and $W = 2\ell\cos\theta n_x$. Finally, from a simple energy balance, the energy dissipation in the bulk structure is extracted as:

$$\Delta U = \frac{N_b f \Delta E_{bar}}{WHL} = \frac{2 f \Delta E_{bar}}{\ell^3 \sin\theta \cos^2\theta} \tag{6.16}$$

where f is the friction of the bar that needs to be buckled to accommodate the global lattice strain. Assuming layer by layer deformation and taking into account that each bar is folded onto itself upon the buckling. f is expressed as:

$$f = \frac{\varepsilon_{\max}}{1 - D/(\ell \sin\theta)} \tag{6.17}$$

6.3 Trends for Optimal Design

The mechanical models described in the previous sections can be used to explore the parameter space and identify optimal designs. Two optimization problems will be addressed in this section: (1) Maximization of the damping figure of merits, $\left|E^*\right|^{1/3} \tan\delta / \rho$, where damping is originated from the viscoelastic nature of the polymer (modeled in section 6.1.1). Damping figure of merit, $\left|E^*\right|^{1/3} \tan\delta / \rho$, expresses how fast a clamped plate subject to forced vibrations reaches to the rest state when the forcing term is removed. (2) Maximization of the dissipated energy (ΔU) in a compression cycle, originating from structural damping (modeled in section 6.2.2).

6.3.1 Maximization of intrinsic damping figure of merit, $\left|E^*\right|^{1/3} \tan\delta / \rho$

The geometric parameters of the system are expressed in non-dimensional forms, the truss angle (θ), the bar aspect ratio (D/ℓ), the ratio of metal wall thickness over length of the bar (t_m/ℓ), and the ratio of polymer wall thickness over length of the bar (t_p/ℓ). The objective function is $\left|E^*\right|^{1/3} \tan\delta / \rho$ where $\left|E^*\right|$, $\tan\delta$, ρ are given by Eq.(6.1), Eq.(6.3), and Eq.(6.4),

respectively. The range of the geometric parameters, imposed by manufacturing constraints and beam theory limitation, is expressed as:

$$\begin{aligned} &10^{-3} < D/\ell < 0.25 \\ &2 < L/D < 16 \\ &10^{-4} < t_m/\ell < 0.3 \\ &10^{-4} < t_p/\ell < 0.3 \\ &45° < \theta < 75° \end{aligned} \tag{6.18}$$

where $L = 2\ell\cos\theta$ is the cell size. As optimization studies performed with the above constraints produce optimal lattices with very high ratio of polymer to metal wall thickness ($t_p/t_m \simeq 500$), which presents substantial manufacturing challenges, we include an additional manufacturing constraint: $t_p/t_m < 10$.

The density of the lattice, given by Eq.(6.4), is swept in the range 10–1000kg/m^3, and for each density the constrained optimization problem described above is solved with the "fmincon" algorithm in MATLAB.

To elucidate the effects of the viscoelastic properties of the polymeric layer (modulus and damping coefficient) on the lattice performance, we repeat our optimization study for eight different polymers with the same $|E^*|\tan\delta = 10^8$. The Young's modulus is changed between the range of 100MPa to 50GPa and damping is changed from 0.002 to 1. The material index ($|E^*|^{1/3}/\rho$) is plotted versus the loss coefficient ($\tan\delta$) for nickel and eight different polymers in Figure 6.10a, and optimal dimensions are shown in Figure 6.10b-e.

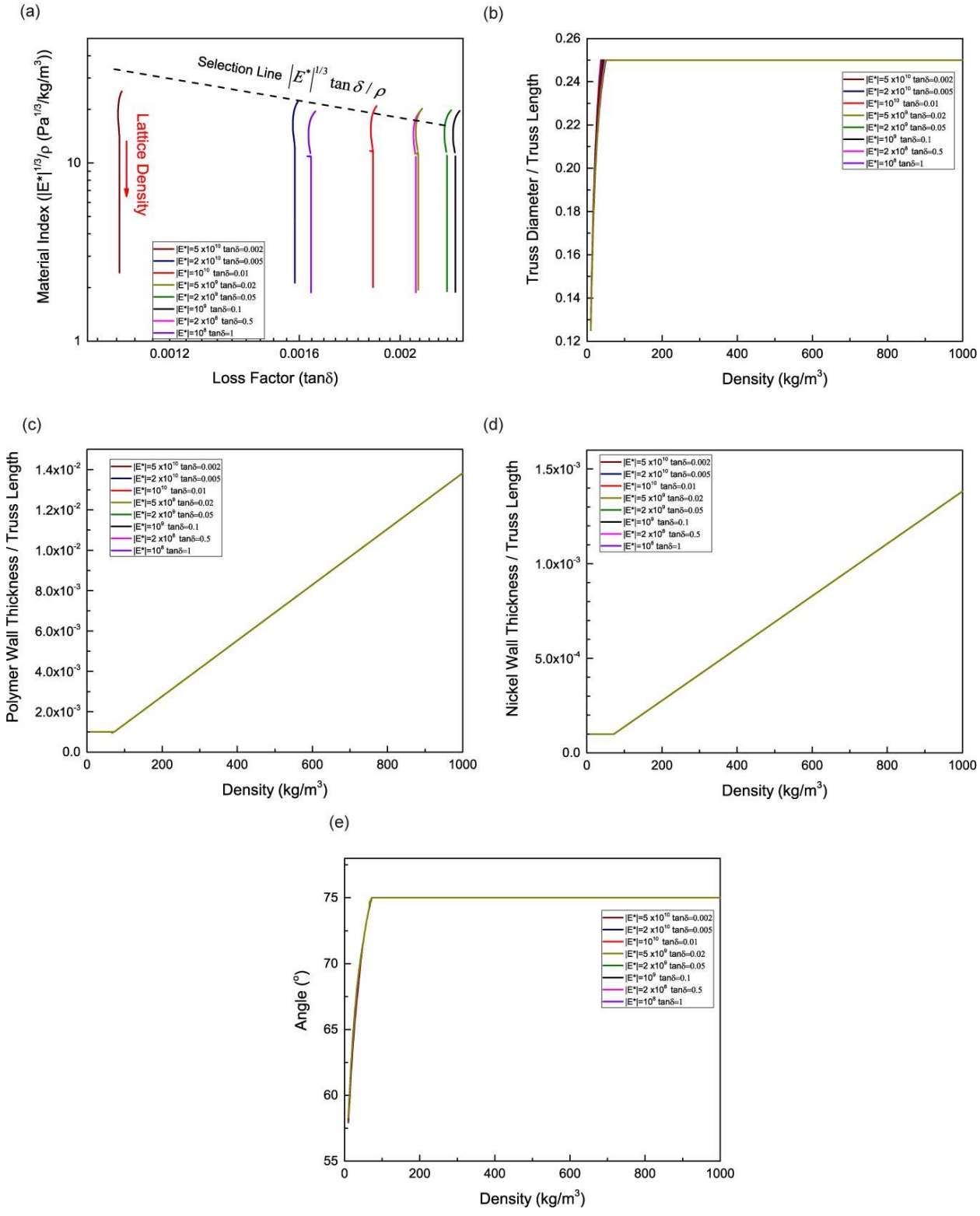

Figure 6.10 (a) Map of achievable $|E^*|^{1/3}/\rho$ of hybrid microlattices with eight different polymers. (b-e) Optimal lattice dimensions.

At the lowest densities, t_p/ℓ and t_m/ℓ remain constant while truss angle θ and D/ℓ increase as the density of the lattice is increased, leading to the decrease of the figure of merit for all the samples. As the density increases, truss angle θ and D/ℓ both hit their upper bounds, while t_p/ℓ and t_m/ℓ increase, thus leading to the decrease of the figure of merit ($\left|E^*\right|^{1/3}/\rho$) with a steeper slope. Throughout the whole density range, the $t_p/t_m<10$ constraint is active.

Young's modulus versus density and loss factor for the same optimization results are depicted in Figure 6.11. These maps allow optimal design. For example, if a minimum allowable Young's modulus is prescribed, the minimum density of the lattice and the maximum values of the damping coefficient can be identified.

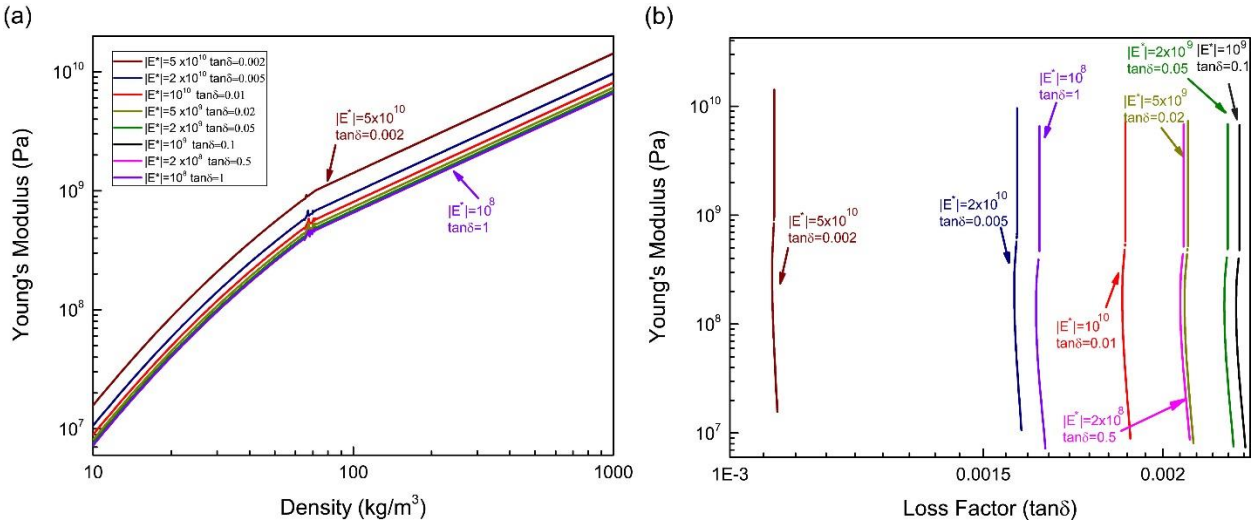

Figure 6.11 Young's modulus versus (a) density and (b) loss factor for hybrid hollow microlattices for eight different polymers.

Not surprisingly, polymers with the highest modulus yield the stiffest lattices. The effect of the polymer choice on the damping coefficient of the lattice is less trivial. For polymers with $\tan\delta<0.5$, increasing the damping coefficient of the polymer yields lossier lattices. But the trend is inverted for polymers with $\tan\delta\geq 0.5$; increasing the damping coefficient of the lattice while

maintaining $\left|E^*\right|\tan\delta = 10^8$ results in very soft polymers, which are incapable of dissipating substantial amounts of energy, thus reducing the damping performance of the lattice.

It is worth mentioning that by removing the $t_p / t_m < 10$ constraint, the lattices show higher damping and lower Young's modulus (due to the tendency to pick thicker polymer layer and thinner nickel layer); unfortunately, those lattices are very challenging to manufacture.

The results indicate that the maximum achievable damping for the lattice is equal to the damping of the polymeric layer (without adding the $t_p / t_m < 10$ constraint); however, the stiffness of the lattice would always exceed the stiffness of the polymeric layer.

In order to understand the advantages of hybrid lattices, optimized nickel / parylene / nickel lattices are compared to (1) optimized single layer nickel lattices, (2) optimized single layer parylene lattices, (3) a Reuss and Voigt composite of nickel / parylene, (4) solid nickel, and (5) solid parylene. In this study, parylene with properties of $\left|E^*\right| = 1.4\text{GPa}$, $\tan\delta = 0.25$, $\rho = 1200\text{kg/m}^3$ and nickel with properties of $E = 210\text{GPa}$, and $\rho = 8900\text{kg/m}^3$ is used. The densities of all the lattices are changed between the range of 10-1000kg/m^3 and the densities of both Voigt and Reuss composites are changed between the range of 1200–8900kg/m^3. Hybrid lattices with two different t_p / t_m constraints ($t_p / t_m < 10$ and $t_p / t_m < 25$) are used to better understand the effects of manufacturing constraints and the advantages of having thicker layer polymer. Figure 6.12a shows the material index ($\left|E^*\right|^{1/3} / \rho$) versus loss factor for the above materials. Not surprisingly, the optimized nickel lattice has the highest performance in this material index and the lowest performance in loss factor, whereas the optimized parylene lattice has the best performance in loss factor. Our hybrid lattices are clearly superior to both Voigt and Resuss composites. The optimized hybrid lattices with the $t_p / t_m < 10$ constraint activated result in lower

damping but higher stiffness; however, hybrid lattice with a $t_p / t_m < 25$ constraint result in higher damping but lower stiffness (due to thicker layer of polymer and thinner layer of nickel).

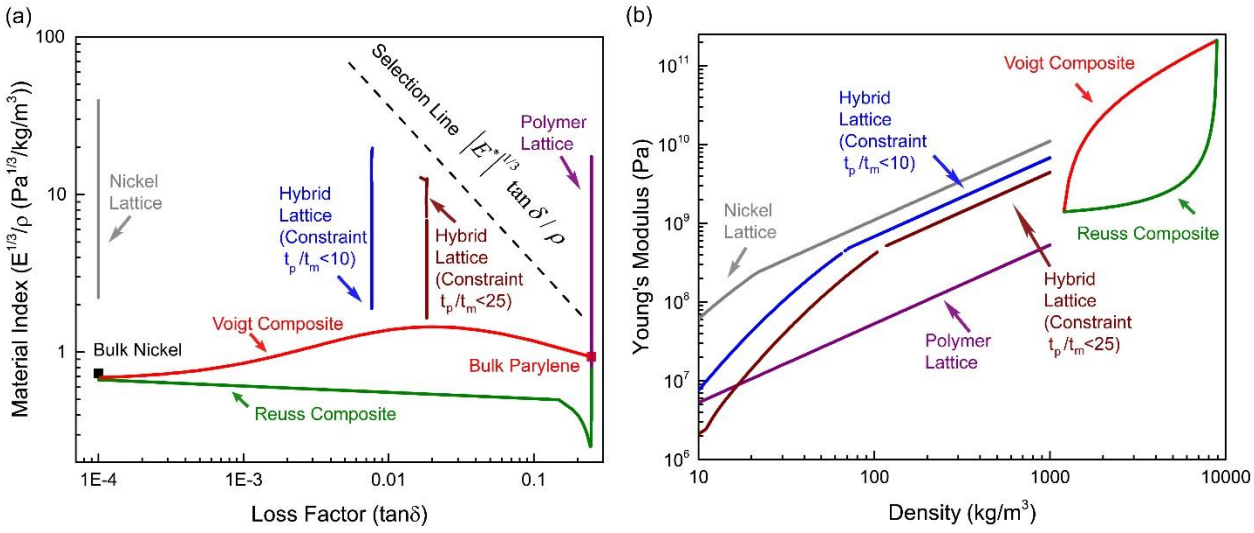

Figure 6.12 Comparison of optimized hybrid microlattices with two different constraints (($t_p / t_m < 10$ and $t_p / t_m < 25$), optimized nickel microlattices, optimized parylene microlattices, solid nickel, solid parylene and Reuss and Voigt composites. (a) Material index $\left|E^*\right|^{1/3} / \rho$ versus loss factor, (b) Young's modulus versus density,

Note that the selection line (Figure 6.12) suggest that the parylene lattices have the highest damping figure of merit; however, as Figure 6.12b indicates, the Young's modulus of parylene lattices is very small. Therefore, the hybrid lattices provide the best practical choice when high stiffness and high intrinsic damping is needed.

6.3.2 Maximization of the dissipated energy per cycle, ΔU, due to structural damping

Finally, in this section, we show how to maximize the bar buckling-induced dissipated energy per cycle in ultralight hybrid microlattices (modeled in section 6.2.2), which leads to maximization of structural damping in hybrid hollow microlattices.

In addition to the manufacturing constraints expressed in Eq.(6.18), we also impose the recoverability constraint (Eq.(6.9)). Furthermore, to avoid yielding preceding buckling as a failure mechanism, we request that:

$$\frac{p_{bar}^{lb}}{p_{bar}^{y}} < 0.9 \tag{6.19}$$

where P_{bar}^{lb} is the critical local buckling of the bar derived from Eq.(6.13) and P_{bar}^{y} is the yielding load of the bar and is calculated as:

$$p_{bar}^{y} = \frac{\pi D^2 t_m \sigma_y}{\ell \cos\theta (1 + \frac{D}{\ell}\frac{\tan\theta}{2})} \tag{6.20}$$

The constrained optimization problem described above is solved with the "fmincon" algorithm in MATLAB for each density within the range of 10–200 kg/m^3 to find the optimized dimensions i.e. truss angle (θ), bar aspect ratio (D/ℓ), ratio of metal wall thickness over length of the bar (t_m/ℓ), and ratio of polymer wall thickness over length of the bar (t_p/ℓ).

Figure 6.13 shows the dissipated energy as a function of density for the hybrid lattices constructed with eight different polymers (as described in the previous section with constant $\left|E^*\right|\tan\delta = 10^8$). Note that in all of these hybrid lattices, nickel is used as the metal layer. Figure 6.14 shows the optimal dimensions for each of the hybrid lattices.

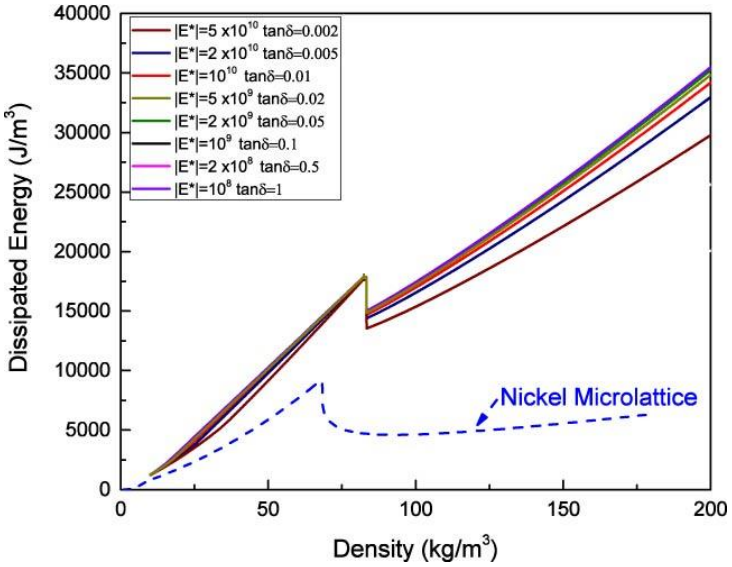

Figure 6.13 Map of achievable ΔU of hybrid microlattices for the eight different polymers compared to nickel microlattices.

As indicated in Figure 6.13, adding a polymer layer to a metallic lattice increases the energy dissipation due to the structural damping ~6-8x by increasing the local buckling load. Such gain varies only slightly for polymers with different properties. In fact, there is only a 15% difference between the increase in energy dissipation yielded by using the polymers with the lowest damping coefficient and the polymer with the highest damping coefficient. This is because the critical buckling load is a function of metal stiffness and the geometry of the lattice Eq.(6.13) rather than the properties of the polymer. Hence the properties of the polymer can be chosen exclusively based on the considerations discussed in sec. 6.3.1.

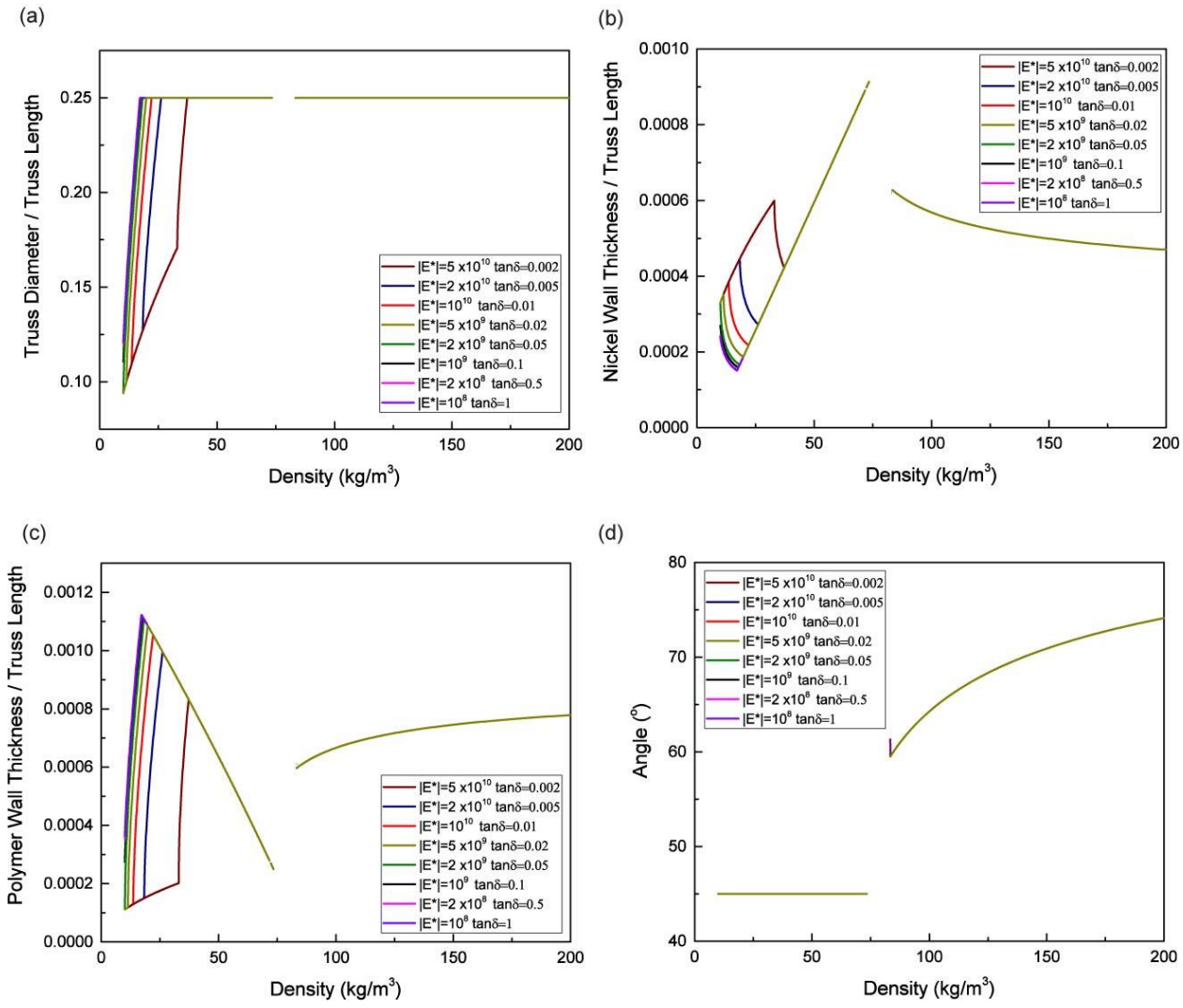

Figure 6.14 Optimal lattice dimensions for hybrid lattices that maximize the energy dissipation per cycle, ΔU.

Notice that the lattice dimensions for lattices optimized for intrinsic (section 6.3.1) and structural damping are completely different. The implication is that it is not feasible to design a single hybrid hollow lattice exhibiting both high intrinsic and structural damping.

CHAPTER 7. DEFECT ANALYSIS OF ULTRALIGHT HOLLOW METALLIC MICROLATTICES

The apparent topological simplicity in hollow microlattices suggests that mechanical properties should be accurately predicted by simple analytical models [53, 54]. However, in practice complex stress states around the hollow nodes and the presence of a variety of manufacturing-induced geometric defects throughout the lattice depress mechanical properties, making analytical estimates often grossly non-conservative. As ultralight lattices are buckling dominated, they are expected to be exceptionally affected by these imperfections.

SEM imaging of hollow microlattice materials is useful to identify the sources imperfections on these lattices. Figure 7.1 shows the hollow microlattice materials from different angles. According to these images, the defects can be categorized as follows: (1) geometric properties variations across the sample (Figure 7.1a); (2) non-circular cross section of the bars (Figure 7.1b); (3) geometric imperfections at nodes (Figure 7.1c); and (4) cracks at nodes Figure 7.1c) or along / across the bars (Figure 7.1). In this work we want to investigate the first two categories (imperfection in the bars) in great detail and investigate their effect on the mechanical properties of microlattices. Note that Ruvalcaba et al. [91] studied the effect of nodal cracks on the mechanical performance of microlattices.

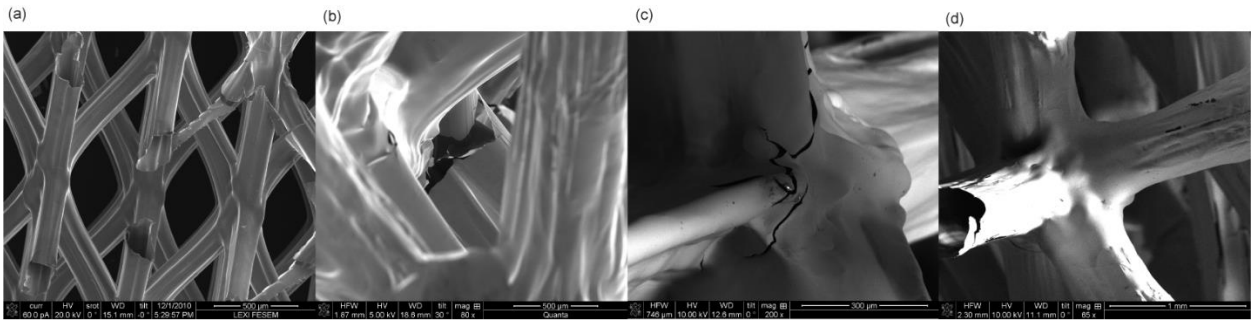

Figure 7.1 Typical geometric defects observed in hollow metallic microlattice materials.

The chapter is organized as follows: section 7.1 quantitatively presents the effects of geometric defects on the density of microlattice materials, and subsequently their strength. Section 7.2. investigates the geometry of the defects at the individual strut level. Finite elements (FE) simulations and Nano-CT scan data are used to investigate the buckling strength of a single bar in a hollow microlattice in section 7.3. The strength of the microlattices then is predicted by accounting for geometric imperfections. In section 7.4, a statistical analysis is performed on the imperfection data gathered from Nano-CT scanning of a number of hollow bars within the metallic microlattices to identify the dominant imperfection modes and build a probabilistic representation that can be used to generate samples of imperfect bars. A statistical analysis of the imperfect samples generated in section 7.4 is finally correlated with strength scatter in a typical sample in section 7.5.

7.1 Analysis of Geometric Variability at the Lattice Level

The dimensions of the microlattice materials (angle, truss length, truss wall thickness and truss diameter) are measured by scanning electron microscope (SEM) with an accuracy of ±2°, ±3%, ±10%, and ±15%, respectively. The diameter shows larger uncertainty due to the fact that the truss is narrower in the middle than the nodes; D represent the average value.

The geometric variations captured by SEM measurement on the hollow microlattices are investigated in more details in this section and their effects on density and strength of lattices are studied.

The bulk microlattice sample in our study is approximately $10cm \times 10cm \times 1.5cm$ which containing bars with the diameter of 650μm; length of 4660μm; wall thickness of 1μm; and finally truss angle of 60^o (based on SEM measurement). The density of the lattices was measured at several scales: first the density of the whole sample was measured; subsequently, the sample was cut into four stripes and the density of each stripe (Figure 7.2) was measured; finally, each stripe was cut into three blocks and the density of each block was measured. The density of the 12 small blocks (Figure 7.2) shows a standard deviation of ~5% and maximum difference of ~15%.

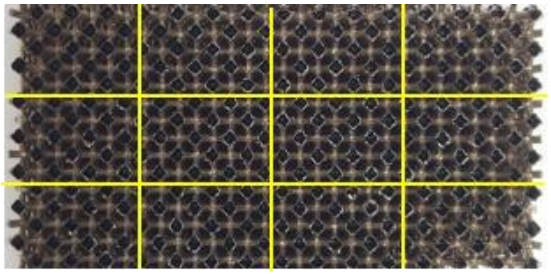

Figure 7.2 The bulk sample cut into smaller blocks.

The relative density of the samples is calculated by using analytical and CAD models, using the dimensions of the lattices provided by SEM imaging. In the analytical model, the density is expressed as:

$$\bar{\rho} = \frac{2\pi}{\cos^2\theta \sin\theta}\left(\frac{D}{\ell}\right)^2 \frac{t}{D} \tag{7.1}$$

where D, t, ℓ , θ are diameter, wall thickness, length, and angle of the truss members, respectively. This model is first-order accurate and results in overlap of material at the nodes; thus, it is expected to result in density overprediction. In the CAD model, on the other hand, the surface area of a unit

cell (with idealized geometry expressed by the PMAT mesh generator, as discussed in [53, 54]) is multiplied by the film thickness (assume to be 1μm uniformly across) to calculate the density. As shown in Figure 7.4, both of these models underpredict the relative density (the CAD model by as much as 30%). This can be tentatively explained by: (1) material accumulation specifically on the top and the bottom of the specimen, (2) non-circular cross sections, and (3) inaccuracy in measuring the dimensions using SEM.

To better understand the reason for the discrepancy, one sample was imaged in nano computed tomography (Nano-CT, with 25μm scan resolution) (Figure 7.3) and the dimensions of the bars were captured. Since the thickness of the specimen is ~1μm, the Nano-CT scan cannot capture the wall thickness of this sample (due to the minimum scan resolution with desired field of view being 25μm); however, the diameter and the length of the bars can be measured accurately, and so can the geometric defects associated with these quantities.

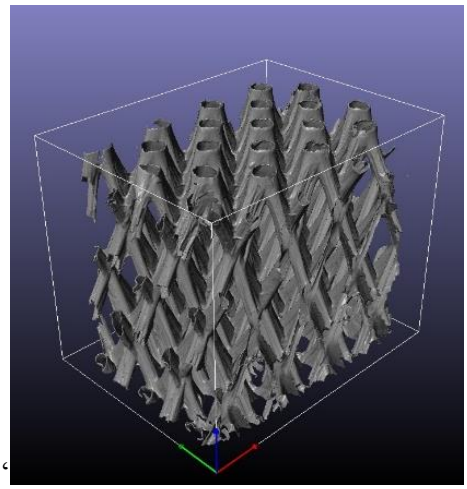

Figure 7.3 Nano-CT image of a microlattice material.

The dimensions of ~150 bars extracted from CT data are measured. The average diameter is measured as ~728μm and the average length of the bars is measured as ~3900μm. The diameter of 650μm and length of 4662μm was measured by SEM. Note that in SEM method, the length is

in fact calculated by substituting the measured SEM diameter in to the L/D ratio of the mask used in the fabrication process. The difference in the diameter measurement is due to both changes of the diameter along the sample and the non-circularity of the bars. Moreover, the difference in the length is because of slight misalignment in the UV light beams that change the location of the nodes from its ideal location leading to longer or shorter bars.

The relative density of the lattice is again calculated by using analytical and CAD models, but this time the length and diameter are average values obtained by Nano-CT scans, with the thickness provided by SEM imaging. The results presented in Figure 7.4 show that the CAD model along with Nano-CT measurements, captured the measured density accurately and not surprisingly, the first-order analytical model overpredicts the density. These results indicate that: 1) the SEM measured dimensions are inaccurate and 2) the thickness is uniform all around the sample.

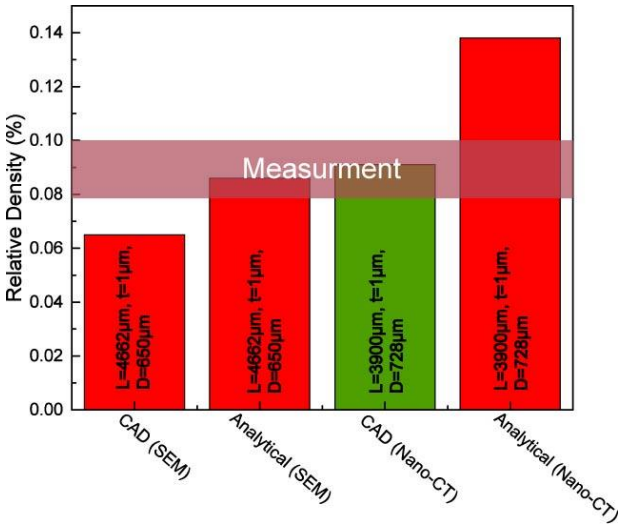

Figure 7.4 Relative density calculations using analytical and CAD models. The dimensions are measured with Nano-CT scan and SEM imaging.

To further investigate the effects of this geometry variation on the properties of the microlattice materials, the strength of all the 12 samples used above are measured under large

quasi-static compression test. All quasi-static compression tests were performed with a servo electrical INSTRON 8862 frame and a National Instrument SCXI data acquisition system. The actuator, featuring an integral concentrically mounted LVDT for precise measurement of position, moved at testing speeds of 100 mm/min to 1 μm/hr and accuracy of 10 μm/s. The load was measured by a 250lb Honeywell load cell. The LabVIEW software was used to collect load and displacement data. Engineering strain and stress are defined as $\varepsilon=\delta/L_0$, $\sigma=P/A_0$ where δ is displacement measured by the LVDT and P is the load measured by external load cell. L_0, and A_0 represent the initial length and the cross section area, respectively.

Representative stress-strain curve of the behavior of these samples is depicted in Figure 7.5a. Note that these samples show full recoverability under 30% strain (samples with ultra-low relative densities exhibit elastic recovery under compressive strain in an excess of 50% [52]).

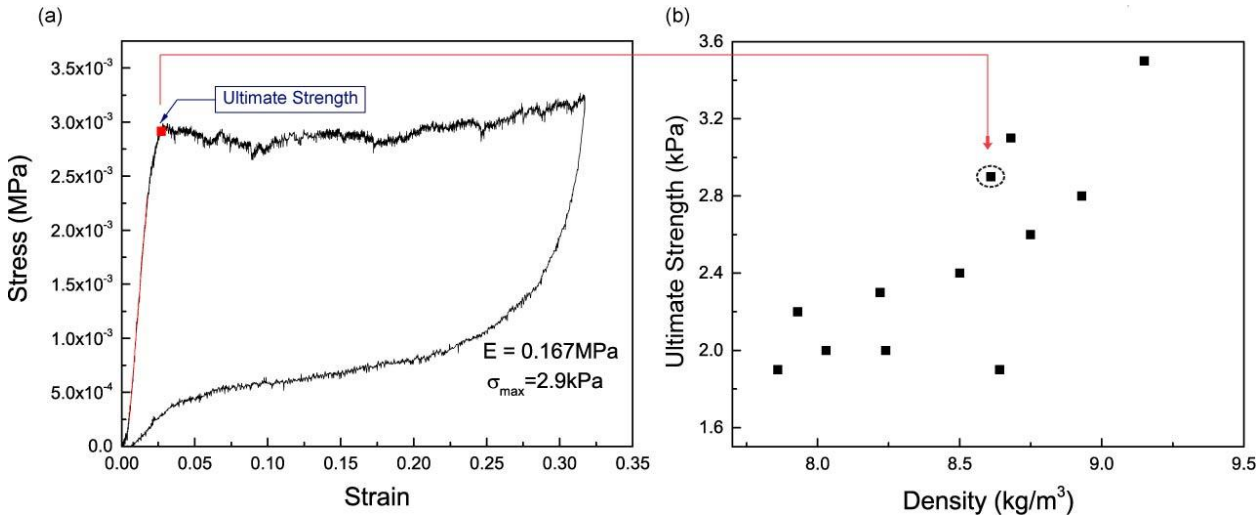

Figure 7.5 (a) Stress-Strain curve for hollow microlattices materials under 30% compressive strain (b) Maximum ultimate strength for different samples extracted from same bulk structure.

Figure 7.5b shows the relations of the maximum ultimate strength vs the density of the lattices. The results indicate that the strength of the samples correlate fairly well with the density; however, a significant scatter (as high as a factor of 2) is observed which cannot be explained by

density variation in the bulk sample. In order to farther investigate the effect of the geometric imperfections on the strength of the microlattices, the geometric defects in the individual bars are studied in detail in the next section.

7.2 Analysis of Geometric Defects at the Individual Strut Level

According to SEM (Figure 7.1) and Nano-CT (Figure 7.3) images, the geometry of individual bars in the hollow microlattice differ from one another and the cross section of the bars are non-circular. Moreover, investigating individual bars extracted form Nano-CT image of the whole sample (Figure 7.6a) shows that the geometry of the cross section of a single bar varies alongside the bar (Figure 7.6b,c). Therefore a detailed study is needed to understand the geometric imperfections of the bars in the lattice. In this section we quantify such geometric defects.

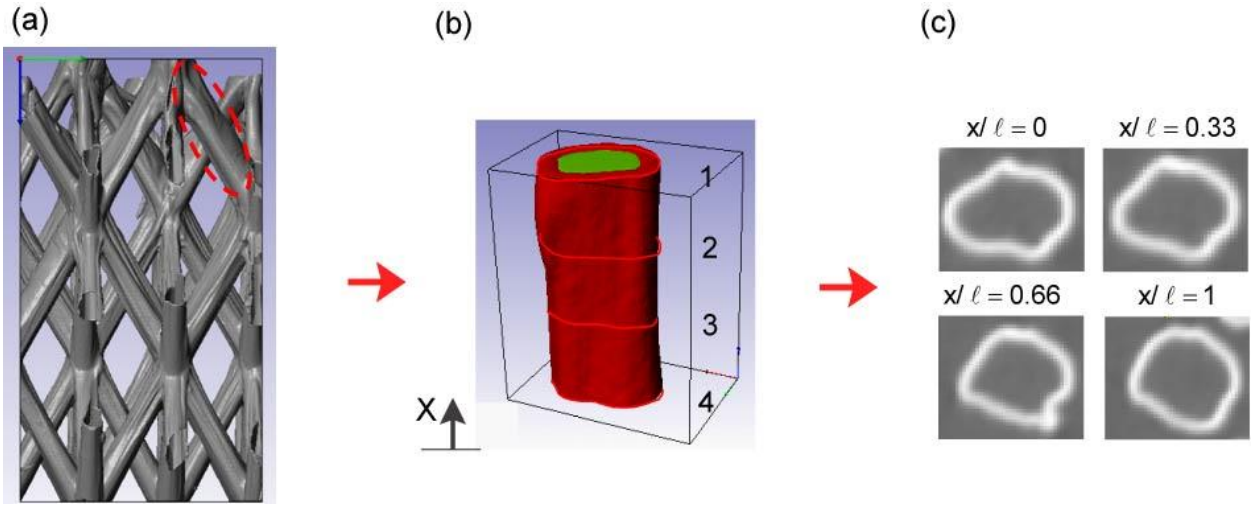

Figure 7.6 (a) Nano-CT image of a microlattice material (b) Nano-CT image of a single bar (c) Cross sections of a representative bar at different locations along the bar, as obtained by Nano-CT characterization.

By using the SIMPLEWARE software ~150 bars are extracted from Nano-CT imaging and disconnected from the nodes. The bars aligned and perfectly cut in order to have a flat surface at both edges (Figure 7.6b). A shell mesh of every single bar is extracted from the Nano-CT data

(depiction in Figure 7.7). Note that since the minimum resolvable feature of the Nano-CT is much larger than the bar thickness, the CT scan shows an artificially larger wall thickness (red edge in Figure 7.6b). Therefore two different shell mesh models were extracted from Nano-CT bars (1) outer layer mesh (2) inner layer mesh (Figure 7.6b).

A C++ program was written to analyze the hollow bar meshes extracted from Nano-CT data and measure the diameter accurately. This program divides each individual mesh into several sections 5μm apart along the x axis (perpendicular to the cross section) and measures the perimeter of each section. The perimeters are used to extract the nominal diameter of a circle with the same perimeter. In order to calculate the effective diameter of each bar, we averaged the inner and outer diameters. Figure 7.7 shows the effective diameter of the inner and outer layer at different cross sections for a single bar. The average value of the inner and outer diameter is shown as a dashed line.

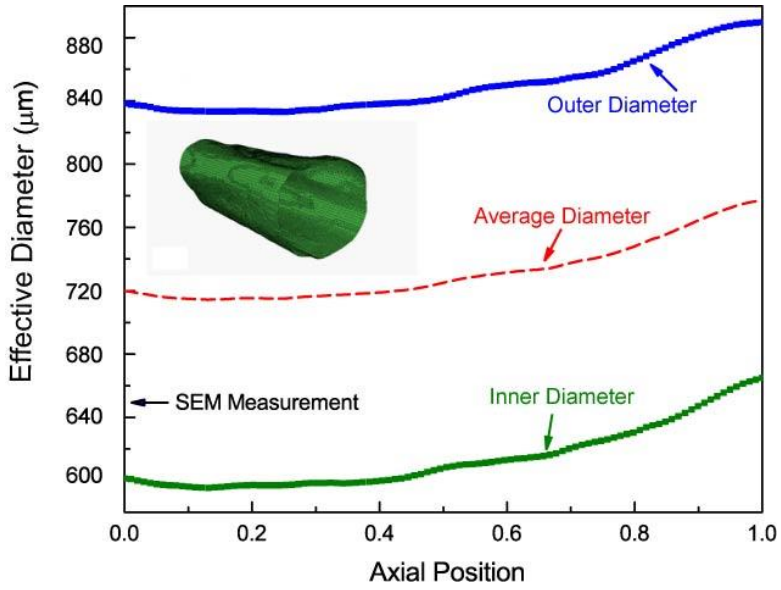

Figure 7.7 Inner, outer and average diameter of a single bar extracted from Nano-CT image (depiction of meshed single bar extracted form Nano-CT images).

Note that the results demonstrated in this paper are from a test with 50μm resolution in order to decrease computational costs. More specifically, we ran our experiments using 50μm and

25μm (the best possible resolution of Nano-CT scan for this sample). The max error observed between these two resolutions were only ~4% and moreover no difference is seen in the cross-sectional geometry, therefore low resolution data is used for all the analysis.

It is worthy of mentioning that due to the artificial thickness of the bar the extracted shell meshes are from outer and inner layers, however in reality the main bar shell is somewhere in the middle of these two models. By using the SIMPLEWARE software (ScanIP) the middle shell bar between the outer and inner layer is extracted. This model is analyzed with C++ code and again the diameter at different cross sections is measured. The results indicate that the average diameter (captured from average of the inner and outer shell model) is very close to the middle shell data (less than ~1% error). Therefore for further analysis the middle shell model is used instead of two inner and outer shells to decrease the computational cost.

~150 bars are detached from Nano-CT data and their middle bar shell models are extracted and the C++ program is used to capture the diameter at different locations. Figure 7.8 shows the diameter as a function of the location along the bar, for all bars within the lattice block. The results indicate that the diameters of the bars at the bottom layer tend to be bigger than the diameters of the ones in the middle and top layers of the lattice. This is mostly due to the changes in the diameter of the UV beam as it passes through the monomer bath (if the intensity of the UV beams is high enough to propagate into the monomer and the exposure time is large enough, it results in increasing in the diameter of the bars by moving through the monomer).

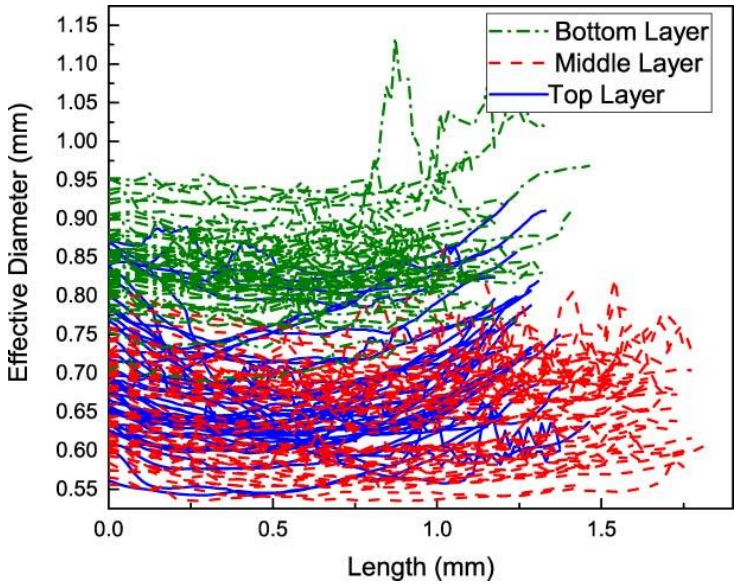

Figure 7.8 The average diameter of the bars within different layers in the lattice.

Hence we showed that the diameter of the bar is not uniform along the bar, while the average bar diameter varies with sample location; furthermore, the bars are highly non-circular. The variation of each bar from a perfect cylinder is calculated as follows.

By using a C++ program, the centroid of each cross section is calculated and the average of the centroid for each bar is captured, in addition to the average diameter. At each section, a circle is drawn with the average diameter of the whole lattice (~728μm calculated from averaging the diameter of each bar at each cross section) and the center of the average centroid of that bar (Figure 7.9a). Finally, the offset of the scanned bar from circular cross section is found at different angles (the offset is measured at intervals of 1 degree). Figure 7.9b shows the results for a specific bar, in terms of deviation from circularity as a function of axial and angular coordinates.

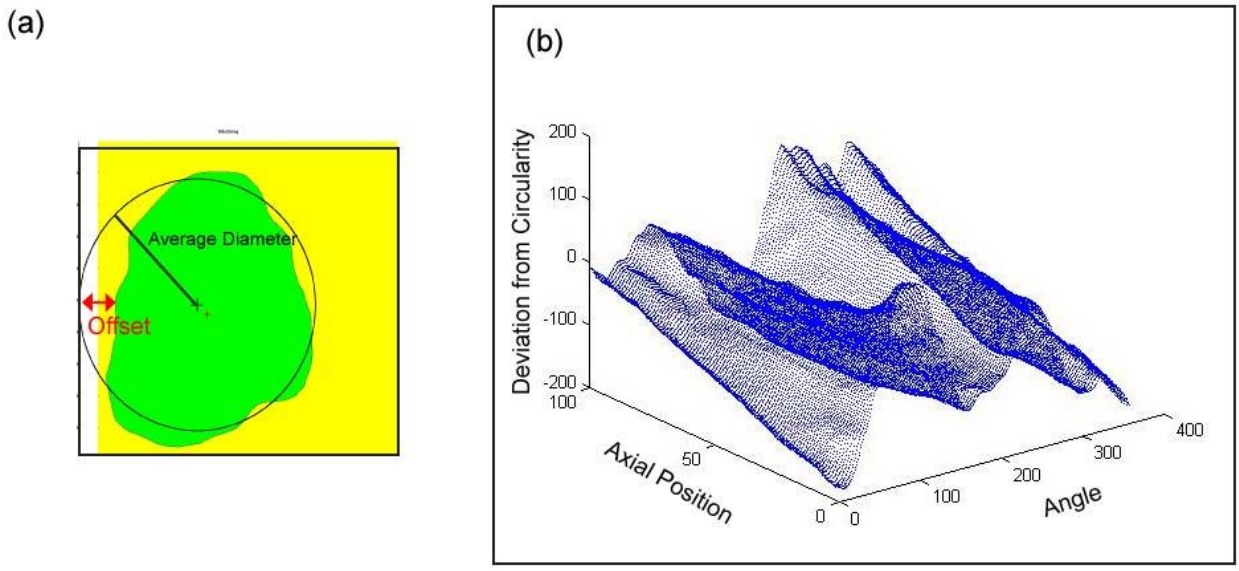

Figure 7.9 The deviation of (a) cross section from from a perfect circle and (b) single bar from cylinder at different angular and axial locations.

As Figure 7.9b shows there is a large deviation from circularity, which might be responsible for the high scatter in the strength data that was seen in the previous section (Figure 7.5b). In the next section we quantify the effect of these deviations on the strength of bars.

7.3 Effects of Bar Shapes on Buckling Strength

In order to investigate the effects of non-circularity on the strength of microlattices, the bars derived from Nano-CT scan were modeled by Finite Elements (FE) analysis, and the buckling load for each of them was extracted. A single bar in a microlattice under compression load experiences a combination of shear and axial load. Since the bar is non-circular, the angle of the shear load changes the amount of the load it can tolerate before buckling; therefore, the shear component of the load was circled around the bar to test all possible orientations of the bar relative to the loading direction (Figure 7.10a).

Shell elements (S3) were used to model the bars and 1μm thickness was assigned to them. One end of the bar was fully clamped and the other end was loaded under compression and shear

load (no rotation is allowed, to best approximate the loading condition within a lattice sample). In the simulation, a nickel layer with the Young's modulus of 210GPa, Poisson ratio of 0.3, and density of 8900kg/m^3 was used. To capture the effects of geometric nonlinearity, the bar was preloaded in a static simulation, followed by a buckling analysis. The shear load was applied along 20 different directions around the circle (18 degrees apart depicted in Figure 7.10a), resulting in 20 FE simulations per bar and total of ~3000 simulations. In order to prepare the input deck for FE simulation as well as extract buckling loads from FE results, a Python program was written. The simulations were run on the HPC cluster using ABAQUS CAE.

The behavior of one CT-derived bar in the microlattice under uniaxial compression is depicted in Figure 7.10b. The results show the critical buckling load at different orientations of the bar relative to the loading direction along with their mode shapes. It is clear that the critical buckling load is a strong function of the bar orientation. The bar extracted from the CT image could fail by local buckling in either shear or compression, depending on their orientations in the unitcell. Note that, according to buckling modes (depiction in Figure 7.10b), if the bar buckles under shear instead of compression, it carries more load.

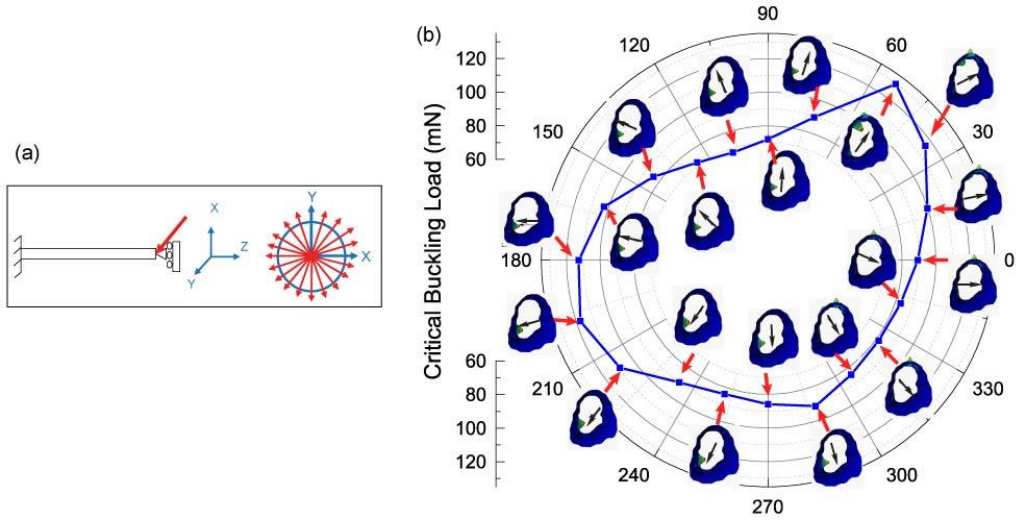

Figure 7.10 (a) Schematic view of one bar in the unit cell under uniaxial compression load. (b) The critical buckling load of the CT-derived mesh and their buckling mode shapes.

The critical buckling load captured from CT-derived bar was then compared to the analytical model and FE simulation to better understand the effects of non-circularity. According to a previous study [53] on failure mechanism of hollow microlattice materials, in the ultralight regime the structure fails under local buckling. The local buckling occurs by shell compression near the nodes where the normal compressive stress due to bending and axial load is maximum or by shell shear throughout the beam length. For slender bars, compression buckling is generally the dominant failure mechanism, but this conclusion changes for stockier bars.

The bar will buckle by shell compression when the maximum compressive stress in the bar on the unitcell equals the critical local buckling stress. Therefore, the buckling load of the bar under compression-bending can be expressed as:

$$P_{cr,bar}^{b+c} = \frac{P_{cr}^{b+c}}{4} = \frac{2\pi E t^2}{\sqrt{3(1-\nu^2)}(\sin\theta + \frac{2\ell\cos\theta}{D})} \tag{7.2}$$

The same conclusion can be driven for shear buckling. Shear buckling occurs when the maximum shear stress in single bar equals the critical stress, leading to:

$$P_{cr,bar}^{sh} = \frac{P_{cr}^{sh}}{4} = \frac{3\pi Et^2}{2\cos\theta}\sqrt{\frac{\sqrt{Dt/2}}{\ell}} \tag{7.3}$$

For the particular bar demonstrated in Figure 7.10b with the length of 1.28mm and the average diameter of 708μm, the critical buckling load is calculated both from analytical model and FE simulations (Figure 7.11a). According to both the analytical model and FE simulation, the bar with geometry specified above buckles under shear load (the loads captured from analytical model and FE simulation are very close). Importantly, the results depicted in Figure 7.11a show that the critical buckling loads for an actual bar is always lower than those for a circular bar with the same length and diameter.

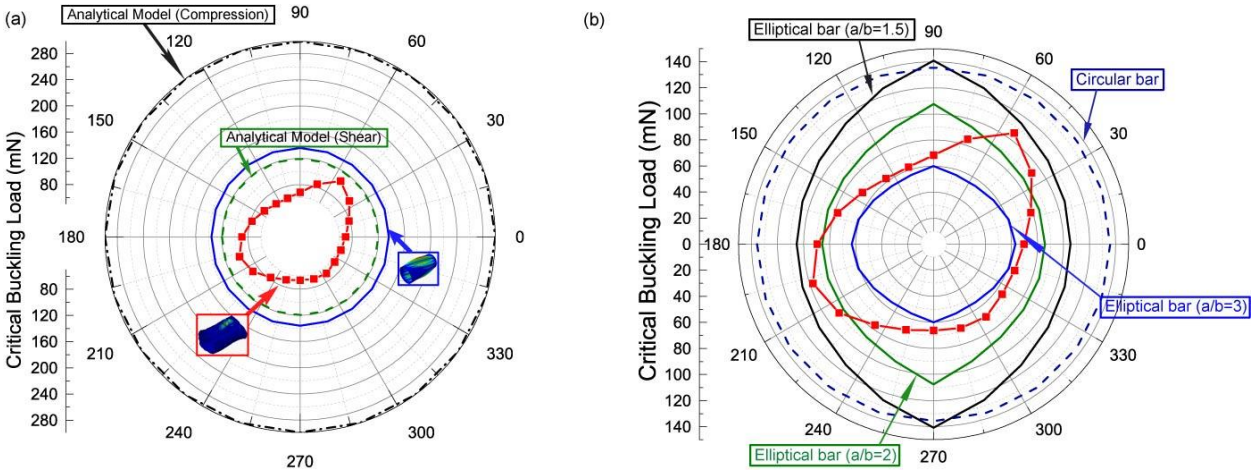

Figure 7.11 (a) Comparison of the critical buckling load of a CT-derived bar and an idealized circular bar of the same mass; analytical model and FE simulations (b) Comparison of the critical buckling load of a CT-drived bar and idealized circular and elliptical bars of equal mass.

Visual inspection of various cross sections of the bars in microlattice materials suggests that the cross sections are closer in shape to ellipses than circles. Therefore, the mechanical strength of the CT-derived bar was compared with that of an elliptical bar with the same perimeter (and hence mass). The comparison was repeated for three elliptical bars with different aspect ratio of the major axis to the minor axis ($a/b = 1.5$, $a/b = 2$, and $a/b = 3$). The major and minor axes

are calculated for the bar with the average diameter of 708μm and length of 1.28mm. The elliptical bars were loaded at different directions and the critical buckling loads were extracted. Figure 7.11b compares the critical buckling load of CT-derived bars and ideal circular and elliptical bars. The results indicate that elliptical bars are weaker than the circular bar. The CT-derived mesh critical buckling load for this specific bar is very similar to the elliptical bar with $a/b=2$.

It is worthy of mentioning that in practice bars used in the microlattices are longer than a CT-derived bar for various reasons (e.g. CT-derived bars are disconnected from nodes and hence are shorter); therefore, to confirm that the same pattern exists in the longer bars, the circular and elliptical bars were modeled with a 3.9mm length (the average length of the bar in the unitcell). The results confirm that elliptical bars are weaker than the circular bar and they even become weaker as the length is increased.

The results of single CT-derived bar were presented in this section and compared to the circular and elliptical bars as a representative behavior of all the bars. However, the behavior of all the bars are important for predicting the behavior of the lattice. Therefore, as mentioned before, all the CT-derived bars were modeled in FE simulation and their critical buckling load were captured. The results of each bar were compared to the behavior of a circular bar with the same perimeter and length as the length of each individual bar. The magnitude of the average deviation of critical buckling load of the CT-derived meshes from perfectly circular bars is calculated for each individual bar. Figure 7.12a shows the deviation of CT-derived bar from circular bar versus the ratio of the diameter over the length of the bar. The results indicate that by decreasing the aspect ratio, the deviation of the critical load of the CT-derived meshes from the circular bar is increasing. The aspect ratio of the bars in this lattice is $D/\ell \sim 0.18$ (with average diameter of

728μm and average length of 3900 μm); therefore, the deviation of the critical load of CT-derived meshes from circular bar is expected to be around 80%.

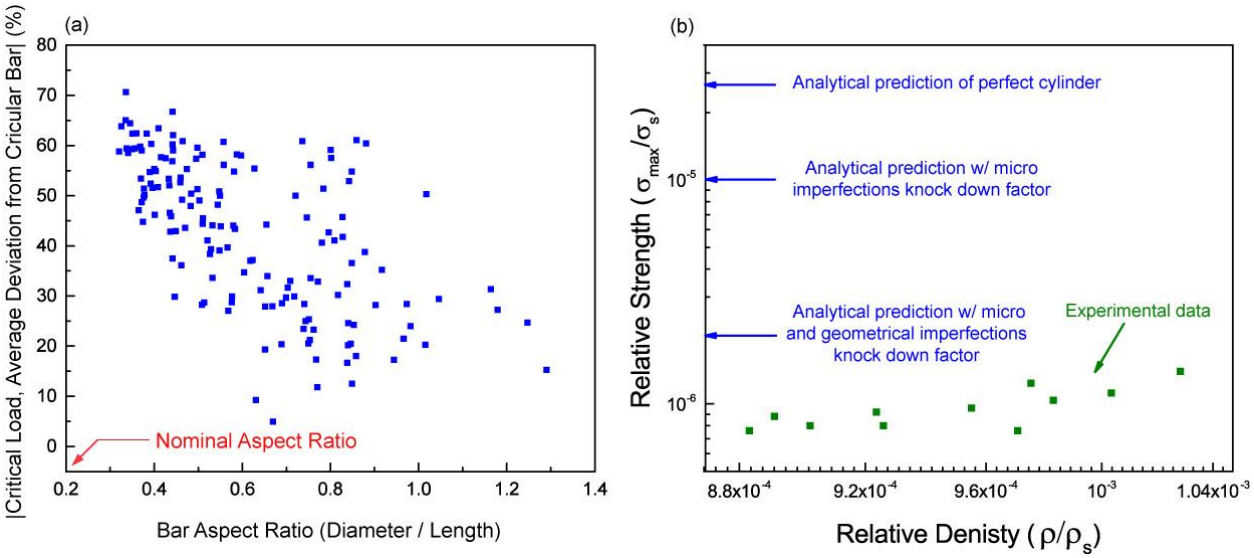

Figure 7.12 (a) Average deviation of the critical load of CT-derived mesh from circular bar versus bar aspect ratio. (b) The comparison of experimental data and analytical model predictions of the strength of a bulk lattice calculated based on local buckling with and without taking into account micro and geometric imperfections.

The buckling strength of the ultralight microlattice can be expressed as $\sigma_{lb} = p_{cr} / (2\ell^2 \cos^2(\theta))$ where p_{cr} is the critical buckling load of the unitcell (calculated from eq. (7.2) or eq.(7.3)) and $2\ell^2 \cos^2(\theta)$ is the effective area of the unitcell. By using this equation, the critical buckling stress for the tested microlattices (with average length of 3900μm, average diameter of 728μm, wall thickness of 1μm and angle of 60 degree) is calculated. The relative strength (critical strength of the lattice over the yield strength of nickel (2.5GPa)) versus the relative density, plotted in Figure 7.12b, indicates that the analytical prediction for strength of the lattice is 20X higher than the experimental results. According to [92], in practice, the load carrying capacity of hollow thin wall cylinders are always lower than predications by elastic buckling theory. This is mainly due to micro imperfections and usually addressed by adding a knock down

factor. Buckling load of the bar under compression-bending with knock down factor can be expressed as [92]:

$$P_{cr,bar}^{b+c} = \frac{P_{cr}^{b+c}}{4} = \frac{2\gamma\pi Et^2}{\sqrt{3(1-\nu^2)}(\sin\theta + \frac{2\ell\cos\theta}{D})} \tag{7.4}$$

where the knock down factor can be expressed as:

$$\gamma = 1 - 0.901(1 - e^{-\phi}) \tag{7.5}$$

where:

$$\phi = \frac{1}{16}\sqrt{\frac{D}{2t}} \tag{7.6}$$

The critical buckling strength for the lattice is decreases by factor ~2.5X when the micro imperfection knock down factor is used. On the other hand, according to sensitivity analysis of hollow bars in the microlattices, Figure 7.12a, the deviation of critical load from perfect cylinder for the bar with aspect ratio of ~0.18 ($D/\ell = 728/3900$) is ~80% which can be used to analytically predict the failure of non-circular bars in the structure. As Figure 7.12b shows, the analytical prediction considering geometric and micro imperfections in the bar, agrees well with the experimental data; however, there is still a 2X difference between the analytical prediction and experimental data. This difference can be explained with the presence of the crack at the structure that suppresses the strength of the lattice [91]. However, the high scatter seen in experimental data is not justified yet. In the next section statistical analysis on Nano-CT derived mesh is presented to identify the source of distribution in experimental data.

7.4 Statistical Analysis of Imperfection Data via POD

One of the most common ways to represent (stochastic) variabilities is through the use of random processes (fields) that are numerically constructed to encapsulate the available information such as the correlation structure or the marginal probability density functions. As the information available, even in the case of a continuously varying field such as geometric imperfection, is often limited to a finite number of sets of measurements collected at certain spatial positions, the path taken towards any probabilistic construction must ensure the consistency; that is as more data is gathered the more closely the statistical properties of the constructed random field should resemble those of the underlying stochastic process. In what follows we perform a statistical analysis of imperfection data gathered from Nano-CT scanning of a number of bars within the metallic microlattices with two goals (i) identifying the dominant imperfection modes (ii) building a probabilistic representation that can be used to generate samples of imperfect bars. While the first of this two goals is more of an exploratory nature the second goal, if achieved, would allow for a statistical analysis of a particular mechanical response of bars, e.g. their instability behavior.

The idea we follow here is similar to that adapted in Ghanem et. al. [93] and is based on a dimension reduction scheme, Karhunen-Loeve Transform or KLT [94], that allows for writing a random process in terms of series representation that involves a set of uncorrelated random variables and a set of "deterministic" functions. No particular form for the statistics, e.g. correlation, and marginal probability distribution, of the stochastic field will be assumed. Instead the mean, correlation function, and the marginal (and potentially the joint) distribution of the reconstructed field will be matched with those of the measurements. To further explain the idea here let $g(x,\theta)$ be the random field representing the geometric flaws. Using KLT this stochastic field can be written in the form of following series representation:

$$g(x,\theta) = \bar{g}(x) + \sum_i \sqrt{\lambda_i}\phi_i(x)\zeta_i(\theta) \tag{7.7}$$

In the above equation $\bar{g}(x)$ denotes the mean (average) geometric flaw field and stochastic quantities are identified by their dependence on θ. The real connection between Eq.(7.7) and the gathered data on geometric flaws is that in practice we deal with samples of a discretized version of the random process that is samples of a random vector. The above equation is therefore re-written in the following form:

$$\mathrm{G}(\theta) = \bar{G} + \sum_i \sqrt{\alpha_i}\Phi_i\xi_i(\theta) \tag{7.8}$$

where G and Φ_i now denote vectors. Furthermore, the eigenpairs (α_i, Φ_i) of the covariance matrix of $G(\theta)$ are approximated using the eigenpairs of the sample covariance matrix for geometric imperfection data Eq. (7.8) is called a Proper Orthogonal Decomposition (POD)–since the eigenvectors Φ_i are orthogonal–and allows for transforming the high dimensional vector G to a few "uncorrelated" random variables ξ_i, samples of which can be obtained from samples of G and the orthogonality property of eigenvectors Φ_i.

7.5 Practical Implementation on Nano-CT Data

Figure 7.13a shows how a sample from geometric imperfection field measured along the length of a typical CT-derived bars and at different angular positions is turned into a 2D sample. Assuming the imperfection measurements are recorded at discrete points on the surface, a typical sample is stored in a matrix resembling a digitized version of an image (see Figure 7.13b). A sample of the random vector G in the above discussion is the vector obtained by concatenating the columns (or rows) of such a matrix.

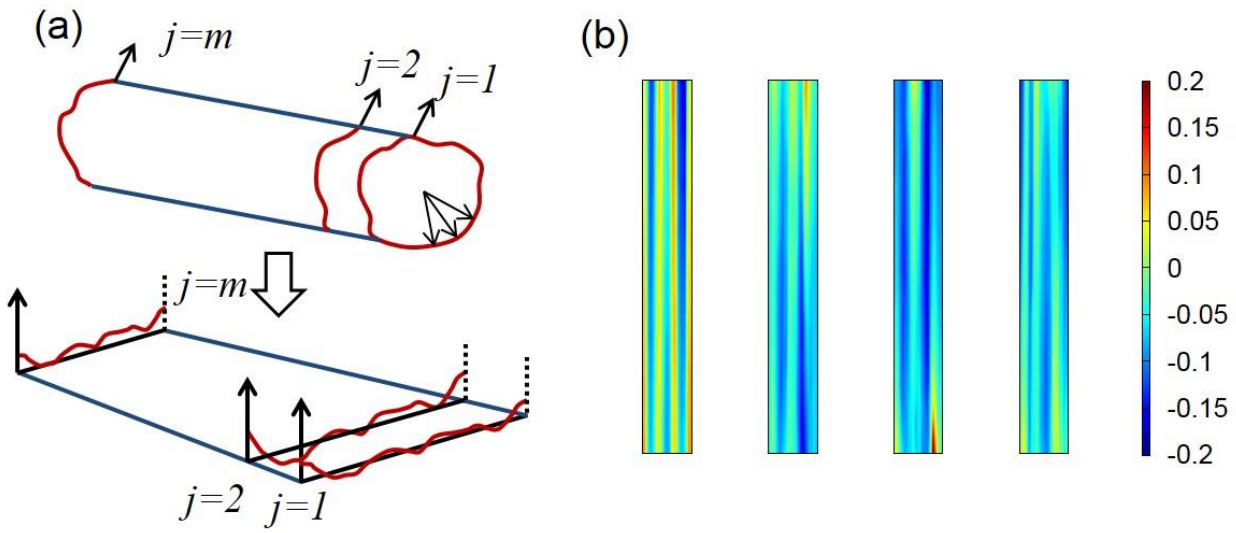

Figure 7.13 (a) Transforming geometric imperfection measurements into a 2D sample. (b) Sample imperfection fields; the vertical access shows the longitudinal direction of the bars while the horizontal axis shoes the circumferential direction.

Figure 7.14a shows the first few dominant imperfection modes obtained from POD of imperfection data while Figure 7.14b shows four imperfect bars generated by sampling from random variables ξ_i in Eq. (7.8) and plugging them back in Eq. (7.8).

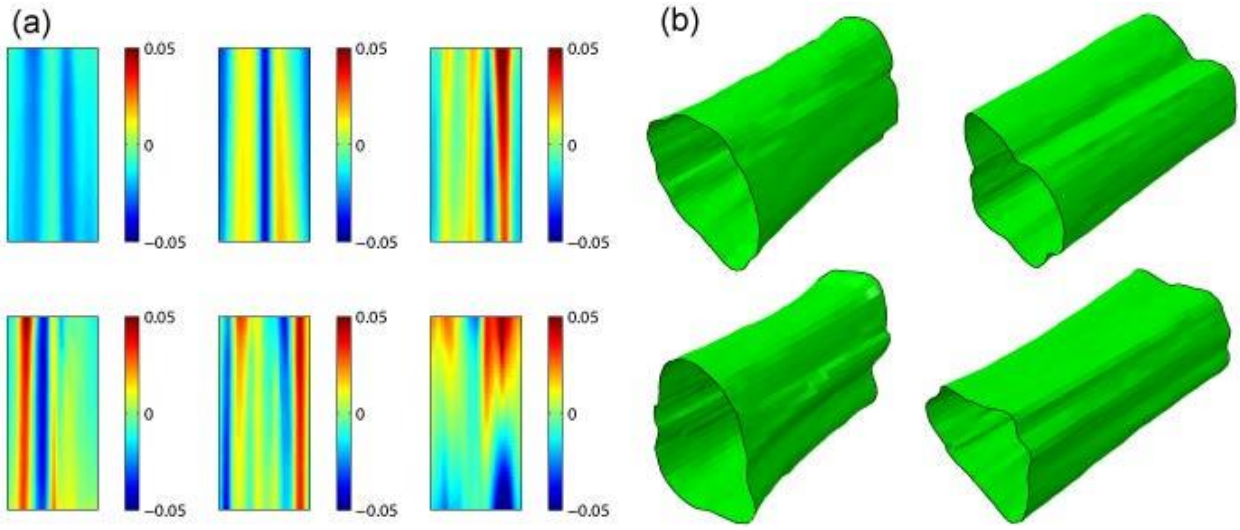

Figure 7.14 (a) The first 6 dominant imperfection modes. (b) first four imperfect bars generated by sampling from random variables.

To further investigate the source of scatter seen in the experimental data, ~120 bars are extracted from Nano-CT data and used in order to generate 2000 imperfect bars with the length of 1.1mm. Note that since the bars in the Nano-CT are detached from the nodes, it is impossible to have a bar with the actual length of 3.9mm. However, the statistical analysis of the effect of the deviations from circularity on the strength of shorter bars can be extended to the bars used in the structure in practice. Finite element (FE) buckling analyses were performed on these bars using the same material (i.e. nickel), same meshes (i.e. S3 shell elements), same boundary conditions (i.e. one end clamped and no rotational freedom at the other end), and the same load as in the simulation described in section 7.3. The shear load was applied in 20 different angles around the circle (18 degrees apart depicted in Figure 7.10a), resulting in 20 FE simulations per bar and total of 40000 simulations. Python program was used to generate the input deck and to post process the data.

The critical buckling load captured from these simulations were compared to the critical buckling load of a cylindrical bar with length of 1100μm, diameter of 728μm (the average diameter of lattice), wall thickness of 1μm. The deviation of the critical buckling load of generated imperfect bars from perfect cylinder were found. Figure 7.15a shows the frequency of deviation of the critical buckling strength of generated imperfect bars from perfect cylinder. According to the data, the standard deviation is ~14% (Figure 7.15a). The critical buckling load prediction from previous section taking into account both micro and geometric imperfections is then used and the standard deviation of 14% is applied to it.

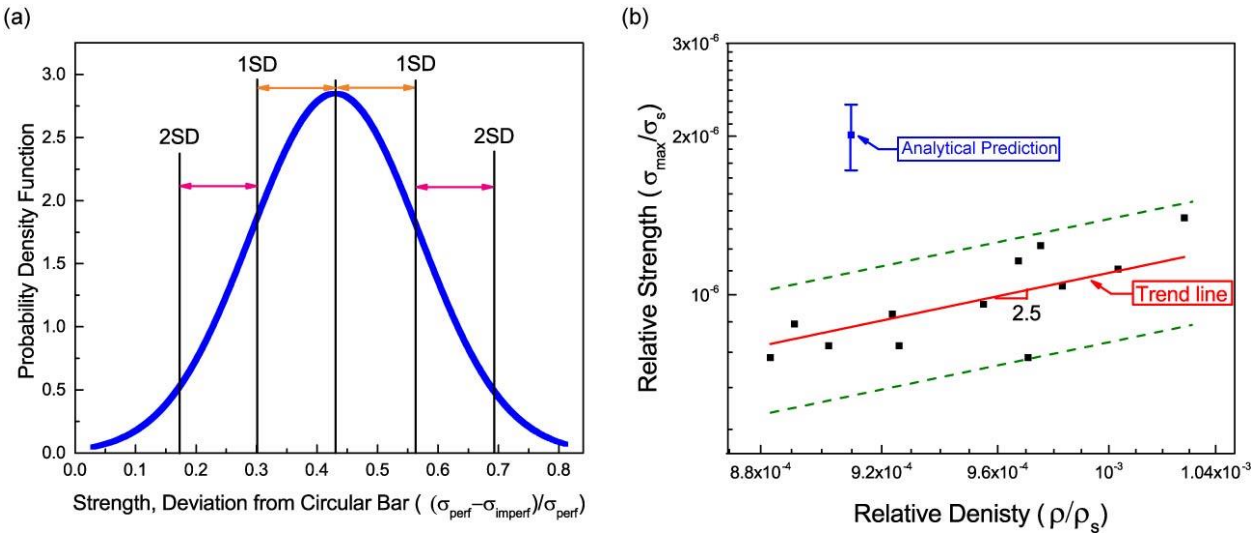

Figure 7.15 (a) Frequency of deviation of critical strength of imperfect bars from the circular bar. (b) The upper and lower limits of the strength of a bulk lattice calculated based on buckling response of non-circular bars both analytically and experimentally.

Figure 7.15b shows the analytical prediction of strength of the lattice taking into account the micro and geometric imperfection knock down factor as well as standard deviation of strength of the lattice base on the geometric imperfection variations from bars to bars. According to previous work on the strength of microlattice materials [52], trend line with a slope of 2.5 is measured, for relative strength vs relative density in the ultra-light regime. Therefore, the trend line with slope of 2.5 is fitted to our experimental data (red solid line) and the standard deviation for the relative strength of those data is calculated (dashed green line).

According to Figure 7.15b the variation in the relative strength of the twelve tested specimen can be explained by the variations in the geometric imperfections from bar to bar. Note that the deviation from analytical model is smaller than the deviation captured in experimental results, this can be due to the experimental error and handling damages of the samples.

CHAPTER 8. CONCLUSIONS

In the course of this dissertation, the stiffness and damping mechanisms in metallic and hybrid hollow microlattices are investigated. Analytical models are proposed and validated by finite elements simulations and experimental characterization. The models are then adapted in optimization studies. The highlights of conclusions for each chapter are as follows:

In chapter 4, we showed that contact measurement techniques are not applicable to Young's modulus measurements on ultralight cellular materials with deformation governed by localized buckling and/or fracture events, as the necessary load application results in the characterization of a post-buckled or post-fractured lattice. We demonstrated that a combination of non-contact scanning Vibrometry experiments and Finite Elements simulations yields values of the Young's modulus that are as much as 10 times higher than those obtained by traditional compression tests, and close to those predicted by FE simulations with periodic boundary conditions. As these BCs correctly capture the symmetry of the sample as well as loading conditions, and predict a compatible deformation field (unlike the free-edge BCs in good agreement with the compression test results), we conclude that the proposed technique significantly increases the accuracy of the measurement. With fabrication of additional samples, all the three Young's moduli of an orthotropic lattice material can be obtained. A similar approach based on in-plane detection can be used for the extraction of shear moduli.

In chapter 5, the damping performance of ultralight hollow metallic microlattices is investigated. Through a combination of large-strain quasi-static compression experiments and infinitesimal-strain resonant tests, the physical mechanisms responsible for energy loss in each compression cycle (and hence damping) were separated and quantified. For strains larger than ~10%, the dominant mechanism is a unique form of structural damping, whereby elastic local

buckling of individual bars releases energy upon loading. A simple mechanical model is introduced to relate the energy loss per cycle to the geometric parameters of the microlattice and the maximum strain amplitude. While being extremely simplistic, this model has a good agreement with a wide range of experimental results obtained on samples of different relative densities (and hence dimensions) at different strain amplitudes. Finally, the mechanical model is adapted in an optimal design study, where the geometric properties of the lattice are optimized for maximum values of a well-known damping figure of merit. The results show that hollow metallic microlattices are superior to any existing metallic material in terms of damping performance, and hence can provide an excellent platform for vibration isolation. The caveat is that buckling-related damping (the unique and dominant damping mechanism) employed by hollow microlattices, requires relative densities well below 1%, limiting the strength, stiffness and energy absorbed per unit volume that microlattices can provide.

This deficiency can be obviated by fabricating hollow lattices with a more complex wall topology, incorporating elastomeric materials with substantial intrinsic damping; this would allow combining two different damping mechanisms (structural buckling-related damping and intrinsic viscous damping in the elastomer), with a potentially substantial increase in the damping figure of merit. In chapter 6, the damping performance of hollow hybrid microlattices is investigated. An analytical model is introduced to capture the intrinsic damping mechanism due to constrained-layer damping phenomenon. The analytical model is validated by finite element simulations at single bar and single half unit cell levels with two different geometries. Infinitesimal-strain resonant tests were performed on both hybrid and single layer nickel microlattices at single bar and single unit cell levels to verify the accuracy of this model. At ultralight regime, single layer lattices show full recoverability under large compressive strain hence dissipating energy. This

mechanism is investigated by finite element simulation for hybrid unit cell and the same performance as single layer unit cell was observed. A simple analytical model is proposed to relate the energy dissipation per cycle to the geometric parameters and its accuracy is validated by FE simulations. Finally, the mechanical models are adapted in an optimal design study where the geometric properties of the lattice are optimized for maximum well-known figure of merit and maximum energy dissipation per cycle due to intrinsic damping and structural damping mechanisms, respectively. The results show that the constrained-layer damping increases the damping performance of microlattices. The energy dissipation mechanism increases by 6-8x in ultralight regime and the experimental data indicates 20% increase in intrinsic damping. Hence, by choosing optimal geometries the amount of damping increases even more. The caveat is that the optimal geometry maps for these optimization studies are different from each other, therefore, at ultralight regime we cannot obtain lattices with maximum intrinsic and structural damping performances. Moreover, the optimization study shows that polymers with high stiffness and high damping results in hybrid lattices with better vibration isolation performance.

In chapter 7, the effects of manufacturing defects on the mechanical performance of ultralight hollow microlattice materials are investigated. The density and strength variations across a bulk sample are measured. The results show that the strength correlates quite well with the density, albeit with a significant scatter. Nano-CT scans were performed to accurately measure the dimensions of each bar in the sample, identify the source of imperfections and quantify the effects of this imperfection on the strength of the lattice. Aided by a rigorous statistical analysis, these results indicate that the significant non-circularity of the bars is largely responsible fro the scatter in experimental strength data. This suggests that by controlling the manufacturing process of these

lattice more carefully and by decreasing the bar non-circularity we can obtain lattices with much better mechanical performance.

REFERENCES

[1] M. F. Ashby, A. Evans, N. A. Fleck, L. J. Gibson, J. W. Hutchinson, and H. N. G. Wadley, *Metal Foam: A Design Guide*. Butterworth Heinemann.

[2] G. LJ and A. MF, *Cellular Solids: Structure and properties*. Cambridg University Press.

[3] N. a. Fleck, V. S. Deshpande, and M. F. Ashby, "Micro-architectured materials: past, present and future," *Proc. R. Soc. A Math. Phys. Eng. Sci.*, vol. 466, no. 2121, pp. 2495–2516, 2010.

[4] A. G. Evans, J. W. Hutchinson, N. A. Fleck, M. F. Ashby, and H. N. G. Wadley, "The topological design of multifunctional cellular metals," *Prog. Mater. Sci.*, vol. 46, no. 3–4, pp. 309–327, 2001.

[5] A. G. Evans, J. W. Hutchinson, and M. F. Ashby, "Multifunctionality of cellular metal systems," *Prog. Mater. Sci.*, vol. 43, no. 3, pp. 171–221, 1998.

[6] H. N. G. Wadley, N. A. Fleck, and A. G. Evans, "Fabrication and structural performance of periodic cellular metal sandwich structures," *Porous Mater.*, vol. 63, no. 16, pp. 2331–2343, Dec. 2003.

[7] L. Valdevit, J. W. Hutchinson, and A. G. Evans, "Structurally optimized sandwich panels with prismatic cores," *Int. J. Solids Struct.*, vol. 41, no. 18–19, pp. 5105–5124, Sep. 2004.

[8] N. Wicks and J. W. Hutchinson, "Optimal truss plates," *Int. J. Solids Struct.*, vol. 38, no. 30–31, pp. 5165–5183, Jul. 2001.

[9] L. Valdevit, Z. Wei, C. Mercer, F. W. Zok, and A. G. Evans, "Structural performance of near-optimal sandwich panels with corrugated cores," *Int. J. Solids Struct.*, vol. 43, no. 16, pp. 4888–4905, Aug. 2006.

[10] A. G. Evans, M. Y. He, V. S. Deshpande, J. W. Hutchinson, A. J. Jacobsen, and W. B. Carter, "Concepts for enhanced energy absorption using hollow micro-lattices," *Int. J. Impact Eng.*, vol. 37, no. 9, pp. 947–959, 2010.

[11] H. J. Rathbun, D. D. Radford, Z. Xue, M. Y. He, J. Yang, V. Deshpande, N. A. Fleck, J. W. Hutchinson, F. W. Zok, and A. G. Evans, "Performance of metallic honeycomb-core sandwich beams under shock loading," *Int. J. Solids Struct.*, vol. 43, no. 6, pp. 1746–1763, Mar. 2006.

[12] C. I. Hammetter, R. G. Rinaldi, and F. W. Zok, "Pyramidal Lattice Structures for High Strength and Energy Absorption," *J. Appl. Mech.*, vol. 80, no. 4, pp. 041015–041015, May 2013.

[13] T. A. Schaedler, C. J. Ro, A. E. Sorensen, Z. Eckel, S. S. Yang, W. B. Carter, and A. J. Jacobsen, "Designing metallic microlattices for energy absorber applications," *Adv. Eng. Mater.*, vol. 16, no. 3, pp. 276–283, 2014.

[14] G. C. Kiessling, "Modern Packaging," p. 287, 1961.

[15] R. A. Olson and L. C. B. Martins, "Cellular Ceramics in Metal Filtration," *Adv. Eng. Mater.*, vol. 7, no. 4, pp. 187–192, 2005.

[16] S. Baudis, F. Nehl, S. C. Ligon, A. Nigisch, H. Bergmeister, D. Bernhard, J. Stampfl, and R. Liska, "Elastomeric degradable biomaterials by photopolymerization-based CAD-CAM for vascular tissue engineering.," *Biomed. Mater.*, vol. 6, no. 5, p. 055003, 2011.

[17] T. J. Lu, H. a. Stone, and M. F. Ashby, "Heat transfer in open-cell metal foams," *Acta Mater.*, vol. 46, no. 10, pp. 3619–3635, 1998.

[18] L. Valdevit, A. Pantano, H. A. Stone, and A. G. Evans, "Optimal active cooling performance of metallic sandwich panels with prismatic cores," *Int. J. Heat Mass Transf.*,

vol. 49, no. 21–22, pp. 3819–3830, 2006.

[19] L. Valdevit, A. J. Jacobsen, J. R. Greer, and W. B. Carter, "Protocols for the Optimal Design of Multi-Functional Cellular Structures: From Hypersonics to Micro-Architected Materials," *J. Am. Ceram. Soc.*, vol. 94, pp. s15–s34, 2011.

[20] T. J. Lu, L. Valdevit, and A. G. Evans, "Active cooling by metallic sandwich structures with periodic cores," *Prog. Mater. Sci.*, vol. 50, no. 7, pp. 789–815, Sep. 2005.

[21] A. Vigliotti and D. Pasini, "Linear multiscale analysis and finite element validation of stretching and bending dominated lattice materials," *Mech. Mater.*, vol. 46, no. 0, pp. 57–68, Mar. 2012.

[22] A. Vigliotti and D. Pasini, "Stiffness and strength of tridimensional periodic lattices," *Comput. Methods Appl. Mech. Eng.*, vol. 229–232, pp. 27–43, 2012.

[23] S. Arabnejad and D. Pasini, "Mechanical properties of lattice materials via asymptotic homogenization and comparison with alternative homogenization methods," *Int. J. Mech. Sci.*, vol. 77, no. 0, pp. 249–262, Dec. 2013.

[24] S. Arabnejad Khanoki and D. Pasini, "Fatigue design of a mechanically biocompatible lattice for a proof-of-concept femoral stem," *J. Mech. Behav. Biomed. Mater.*, vol. 22, no. 0, pp. 65–83, Jun. 2013.

[25] A. Vigliotti, V. S. Deshpande, and D. Pasini, "Non linear constitutive models for lattice materials," *J. Mech. Phys. Solids*, vol. 64, no. 0, pp. 44–60, Mar. 2014.

[26] S. K. Maiti, L. J. Gibson, and M. F. Ashby, "Deformation and energy absorption diagrams for cellular solids," *Acta Metall.*, vol. 32, no. 11, pp. 1963–1975, 1984.

[27] W. Chen and T. Wierzbicki, "Relative merits of single-cell, multi-cell and foam-filled thin-walled structures in energy absorption," *Thin-Walled Struct.*, vol. 39, no. 4, pp. 287–306,

2001.

[28] F. Han, Z. Zhu, and J. Gao, “Compressive deformation and energy absorbing characteristic of foamed aluminum,” *Metall. Mater. Trans. A*, vol. 29, no. 10, pp. 2497–2502, 1998.

[29] A. G. Evans, M. Y. He, V. S. Deshpande, J. W. Hutchinson, A. J. Jacobsen, and W. B. Carter, “Concepts for enhanced energy absorption using hollow micro-lattices,” *Int. J. Impact Eng.*, vol. 37, no. 9, pp. 947–959, 2010.

[30] H. Wadley, K. Dharmasena, M. He, R. McMeeking, A. Evans, T. Bui-Thanh, and R. Radovitzky, “An active concept for limiting injuries caused by air blasts,” *Int. J. Impact Eng.*, vol. 37, no. 3, pp. 317–323, 2010.

[31] C. D. D. Johnson, “Design of Passive Damping Systems,” *J. Mech. Des.*, vol. 117, no. B, p. 171, 1995.

[32] C. Erin, B. Wilson, and J. Zapfe, “AN IMPROVED MODEL OF A PNEUMATIC VIBRATION ISOLATOR: THEORY AND EXPERIMENT,” *J. Sound Vib.*, vol. 218, no. 1, pp. 81–101, Nov. 1998.

[33] N. Zhou and K. Liu, “A tunable high-static–low-dynamic stiffness vibration isolator,” *J. Sound Vib.*, vol. 329, no. 9, pp. 1254–1273, Apr. 2010.

[34] I. Buckle, S. Nagarajaiah, and K. Ferrell, “Stability of Elastomeric Isolation Bearings: Experimental Study,” *J. Struct. Eng.*, vol. 128, no. 1, pp. 3–11, Jan. 2002.

[35] M. D. Rao, “Recent applications of viscoelastic damping for noise control in automobiles and commercial airplanes,” *J. Sound Vib.*, vol. 262, no. 3, pp. 457–474, 2003.

[36] P. Number, “United States Patent [19] [54],” pp. 0–4, 1984.

[37] D. L. Platus, “Negative-stiffness-mechanism vibration isolation systems,” 1999, vol. 3786, pp. 98–105.

[38] C. M. A. Vasques and J. Dias Rodrigues, “Active vibration control of smart piezoelectric beams: Comparison of classical and optimal feedback control strategies,” *Comput. Struct.*, vol. 84, no. 22–23, pp. 1402–1414, 2006.

[39] A. Preumont, *Vibration control of active structures: An Introduction*. Springer, 2011.

[40] T. Bailey and J. E. Hubbard, “Distributed piezoelectric-polymer active vibration control of a cantilever beam,” *J. Guid. Control. Dyn.*, vol. 8, no. 5, pp. 605–611, 1985.

[41] J. Banhart, “Manufacture, characterisation and application of cellular metals and metal foams,” *Prog. Mater. Sci.*, vol. 46, no. 6, pp. 559–632, 2001.

[42] J. Banhart, J. Baumeister, and M. Weber, “Damping properties of aluminium foams,” *Mater. Sci. Eng. A*, vol. 205, no. 1–2, pp. 221–228, Jan. 1996.

[43] T. Pritz, “Dynamic Young’s modulus and loss factor of plastic foams for impact sound isolation,” *Journal of Sound and Vibration*, vol. 178, no. 3. pp. 315–322, 1994.

[44] A. Asadpoure, M. Tootkaboni, and L. Valdevit, “Optimal design of multiphase architected materials for energy dissipation,” *J. Comput. Methods Appl. Mech. Eng.*

[45] S. Shan, S. H. Kang, J. R. Raney, P. Wang, L. Fang, F. Candido, J. A. Lewis, and K. Bertoldi, “Multistable Architected Materials for Trapping Elastic Strain Energy,” *Adv. Mater.*, vol. 27, no. 29, pp. 4296–4301, 2015.

[46] B. Haghpanah, L. Salari-Sharif, P. Pourrajab, J. Hopkins, and L. Valdevit, “Multistable Shape-Reconfigurable Architected Materials.”

[47] A. J. Jacobsen, W. Barvosa-Carter, and S. Nutt, “Micro-scale Truss Structures formed from Self-Propagating Photopolymer Waveguides,” *Adv. Mater.*, vol. 19, no. 22, pp. 3892–3896, 2007.

[48] A. J. Jacobsen, W. Barvosa-Carter, and S. Nutt, “Micro-scale truss structures with three-

fold and six-fold symmetry formed from self-propagating polymer waveguides," *Acta Mater.*, vol. 56, no. 11, pp. 2540–2548, 2008.

[49] J. R. Greer and J. T. M. De Hosson, "Plasticity in small-sized metallic systems: Intrinsic versus extrinsic size effect," *Prog. Mater. Sci.*, vol. 56, no. 6, pp. 654–724, 2011.

[50] T. A. Schaedler, A. J. Jacobsen, A. Torrents, A. E. Sorensen, J. Lian, J. R. Greer, L. Valdevit, and W. B. Carter, "Ultralight metallic microlattices.," *Science*, vol. 334, no. 6058, pp. 962–5, 2011.

[51] X. Zheng, H. Lee, T. H. Weisgraber, M. Shusteff, J. DeOtte, E. B. Duoss, J. D. Kuntz, M. M. Biener, Q. Ge, J. a Jackson, S. O. Kucheyev, N. X. Fang, and C. M. Spadaccini, "Ultralight, ultrastiff mechanical metamaterials.," *Science*, vol. 344, no. 6190, pp. 1373–7, 2014.

[52] A. Torrents, T. A. Schaedler, A. J. Jacobsen, W. B. Carter, and L. Valdevit, "Characterization of nickel-based microlattice materials with structural hierarchy from the nanometer to the millimeter scale," *Acta Mater.*, vol. 60, no. 8, pp. 3511–3523, 2012.

[53] L. Valdevit, S. W. Godfrey, T. a. Schaedler, A. J. Jacobsen, and W. B. Carter, "Compressive strength of hollow microlattices: Experimental characterization, modeling, and optimal design," *J. Mater. Res.*, vol. 28, no. 17, pp. 2461–2473, 2013.

[54] S. W. Godfery and L. Valdevit, "A Novel Modeling Platform for Characterization and Optimal Design of Micro-Architected Materials," 2012, pp. 1–10.

[55] K. J. Maloney, C. S. Roper, A. J. Jacobsen, W. B. Carter, L. Valdevit, and T. A. Schaedler, "Microlattices as architected thin films: Analysis of mechanical properties and high strain elastic recovery," *APL Mater.*, vol. 1, no. 2, pp. 1–8, 2013.

[56] A. Cao, P. L. Dickrell, W. G. Sawyer, M. N. Ghasemi-Nejhad, and P. M. Ajayan, "Super-

Compressible Foamlike Carbon Nanotube Films," *Science (80-.).*, vol. 310, no. 5752, pp. 1307–1310, Nov. 2005.

[57] J. Yin, X. Li, J. Zhou, and W. Guo, "Ultralight three-dimensional boron nitride foam with ultralow permittivity and superelasticity," *Nano Lett.*, vol. 13, no. 7, pp. 3232–3236, 2013.

[58] F. Fraternali, T. Blesgen, A. Amendola, and C. Daraio, "Multiscale mass-spring models of carbon nanotube foams," *J. Mech. Phys. Solids*, vol. 59, no. 1, pp. 89–102, 2011.

[59] A. Rafsanjani, A. Akbarzadeh, and D. Pasini, "Snapping Mechanical Metamaterials under Tension," *Adv. Mater.*, vol. 27, no. 39, pp. 5931–5935, 2015.

[60] D. Restrepo, N. D. Mankame, and P. D. Zavattieri, "Phase transforming cellular materials," *Extrem. Mech. Lett.*, vol. 4, pp. 52–60, 2015.

[61] T. Collins and K. Kochersberger, "Constrained Layer Damping Test Results for Aircraft Landing Gear," in *Structural Dynamics, Volume 3: Proceedings of the 28th IMAC, A Conference on Structural Dynamics, 2010*, T. Proulx, Ed. New York, NY: Springer New York, 2011, pp. 303–314.

[62] L. R. Meza, A. J. Zelhofer, N. Clarke, A. J. Mateos, D. M. Kochmann, and J. R. Greer, "Resilient 3D hierarchical architected metamaterials.," *Proc. Natl. Acad. Sci. U. S. A.*, vol. 112, no. 37, pp. 11502–7, 2015.

[63] D. Jang, L. R. Meza, F. Greer, and J. R. Greer, "Fabrication and deformation of three-dimensional hollow ceramic nanostructures," *Nat Mater*, vol. 12, no. 10, pp. 893–898, Oct. 2013.

[64] J. C. Wallach and L. J. Gibson, "Defect sensitivity of a 3D truss material," *Scr. Mater.*, vol. 45, no. 6, pp. 639–644, 2001.

[65] A. J. Jacobsen, W. Barvosa-Carter, and S. Nutt, "Compression behavior of micro-scale truss

structures formed from self-propagating polymer waveguides," *Acta Mater.*, vol. 55, no. 20, pp. 6724–6733, 2007.

[66] L. Kiesewetter, J. M. Zhang, D. Houdeau, and A. Steckenborn, "Determination of Young's moduli of micromechanical thin films using the resonance method," *Sensors Actuators A. Phys.*, vol. 35, no. 2, pp. 153–159, 1992.

[67] J. P. Cleveland, S. Manne, D. Bocek, and P. K. Hansma, "A nondestructive method for determining the spring constant of cantilevers for scanning force microscopy," *Rev. Sci. Instrum.*, vol. 64, no. 2, pp. 403–405, Feb. 1993.

[68] Q. Qin, F. Xu, Y. Cao, P. I. Ro, and Y. Zhu, "Measuring true young's modulus of a cantilevered nanowire: Effect of clamping on resonance frequency," *Small*, vol. 8, no. 16, pp. 2571–2576, 2012.

[69] N. G. Chopra and A. Zettl, "Measurement of the elastic modulus of a multi-wall boron nitride nanotube," *Solid State Commun.*, vol. 105, no. 5, pp. 297–300, 1998.

[70] A. International, *ASTM E1875 − 08 Standard Test Method for Dynamic Young's Modulus, Shear Modulus, and Poisson's Ratio by Sonic Resonance1s*, vol. 03:01. .

[71] A. International, *ASTM E1876 − 09- Standard Test Method for Dynamic Young's Modulus, Shear Modulus, and Poisson's Ratio by Impulse Excitation of Vibration1*, vol. 03:01. .

[72] I. Ritchie, "Improved resonant bar techniques for the measurement of dynamic elastic moduli and a test of the Timoshenko beam theory," *J. Sound Vib.*, vol. 31, no. 4, pp. 453–468, 1973.

[73] G. C. Righini, A. Tajani, and A. Cutolo, *An Introduction to Optoelectronic Sensors*, vol. 7. 2009.

[74] P. Castellini, M. Martarelli, and E. P. Tomasini, "Laser Doppler Vibrometry: Development

of advanced solutions answering to technology's needs," *Mech. Syst. Signal Process.*, vol. 20, no. 6, pp. 1265–1285, 2006.

[75] L. Salari-Sharif and L. Valdevit, "Accurate Stiffness Measurement of Ultralight Hollow Metallic Microlattices by Laser Vibrometry," *Exp. Mech.*, vol. 54, no. 8, pp. 1491–1495, 2014.

[76] L. Meirovitch, *Analytical methods in vibrations.* New York: Macmillan, 1967.

[77] L. Salari-Sharif, T. a. Schaedler, and L. Valdevit, "Energy dissipation mechanisms in hollow metallic microlattices," *J. Mater. Res.*, vol. 29, no. 16, pp. 1755–1770, 2014.

[78] C. R. Wong and E. J. Graesser, "The Relationship of Traditional Damping Measures for Materials with High Damping Capacity."

[79] B. L. Lazan, *Damping of Materials and Members in Structural Mechanics*. New York: Pergamon Press Ltd., 1968.

[80] L. Meirovitch, *Fundamentals of vibrations*. .

[81] "ASTM Standard Test Method for Measuring Vibration-Damping Properties of Materials," 2010.

[82] J. Lohmiller, C. Eberl, R. Schwaiger, O. Kraft, and T. J. Balk, "Mechanical spectroscopy of nanocrystalline nickel near room temperature," *Scr. Mater.*, vol. 59, no. 4, pp. 467–470, Aug. 2008.

[83] R. S. Lakes, T. Lee, a Bersie, and Y. C. Wang, "Extreme damping in composite materials with negative-stiffness inclusions.," *Nature*, vol. 410, no. 6828, pp. 565–567, 2001.

[84] H. Kalathur and R. S. Lakes, "Column dampers with negative stiffness: high damping at small amplitude," *Smart Mater. Struct.*, vol. 22, no. 8, p. 084013, 2013.

[85] I. Benichou and S. Givli, "Structures undergoing discrete phase transformation," *J. Mech.*

Phys. Solids, vol. 61, no. 1, pp. 94–113, 2013.

[86] C. R. Calladine, *Theory of Shell Structures*. Cambridg University Press, 1983.

[87] J.G.Teng and J.M.Rotter, *Buckling of Thin Metal Shells*. .

[88] L. Dong and R. Lakes, "Advanced damper with high stiffness and high hysteresis damping based on negative structural stiffness," *Int. J. Solids Struct.*, vol. 50, no. 14–15, pp. 2416–2423, Jul. 2013.

[89] E. Andreassen, "Stress relaxation of polypropylene fibres with various morphologies," *Polymer (Guildf).*, vol. 40, no. 14, pp. 3909–3918, 1999.

[90] B. Budiansky, "On the minimum weights of compression structures," *Int. J. Solids Struct.*, vol. 36, pp. 3677–3708, 1999.

[91] N.M. Ruvalcaba, A. Ortega, A. Asadpoure, and L. Valdevit, "Uniaxial strength of hollow microlattices with partially cracked nodes."

[92] "Bucklnig of Thin-walled Circular Cylinder," *Natl. Aeronaut. Sp. Adm.*, 1965.

[93] R. G. Ghanem and A. Doostan, "On the construction and analysis of stochastic models: Characterization and propagation of the errors associated with limited data," *Uncertain. Quantif. Simul. Sci.*, vol. 217, no. 1, pp. 63–81, Sep. 2006.

[94] Michel Loeve, *Probability theory*. New York: Springer-Verlag, 1978.

[95] K. Sharp, D. Mungalov, and J. Brown, "Metallic Cellular Materials Produced by 3D Weaving," *Procedia Mater. Sci.*, vol. 4, no. Complete, pp. 15–20, 2014.

[96] L. Zhao, S. Ha, K. W. Sharp, A. B. Geltmacher, R. W. Fonda, A. H. Kinsey, Y. Zhang, S. M. Ryan, D. Erdeniz, D. C. Dunand, K. J. Hemker, J. K. Guest, and T. P. Weihs, "Permeability measurements and modeling of topology-optimized metallic 3-D woven lattices," *Acta Mater.*, vol. 81, pp. 326–336, 2014.

[97] S. M. Ryan, S. Szyniszewski, S. Ha, R. Xiao, T. D. Nguyen, K. W. Sharp, T. P. Weihs, J. K. Guest, and K. J. Hemker, “Damping behavior of 3D woven metallic lattice materials,” *Scr. Mater.*, vol. 106, pp. 1–4, 2015.

APPENDIX A: STIFFNESS MEASUREMENTS OF ORTHOTROPIC LATTICES

As mentioned in chapter 4 the microlattices under consideration are orthotropic. If the x and y directions are equivalent, six elastic constants would be needed to fully characterize the elastic response of the material. As the presence of the face sheets (essential for optical detection) and the single-axis detection limit the number of modes that can be observed, fitting the entire elastic tensor to the observed peaks presents significant challenges. However, this technique can be adapted to capture all the elastic constants by eliminating the undesired factors such as face sheets and single axis detection. Since, the face sheets are essential for optical detections in hollow microlattices, lattices with different topology can be used to expand the method developed in chapter 4.

Micro-architected metallic lattice materials manufactured through a non-crimp 3D weaving technique [95] has received attention during past years. The wires in this structure can be tailored to optimize specific properties such as fluid permeability [96], high damping at high temperatures [97], and high stiffness, by bounding wires together. Measuring all components of stiffness matrix of these lattices is important for future practical applications; however, using the known standard techniques (e.g. uniaxial compression, 3-point bending) is challenging due to the deformation and movement of the wires as well as bounding between them. Therefore, the non-contact method introduced in chapter 4 can be suitable for measuring the stiffness of these lattices.

3D woven lattices are built of wires with diameter ranging between micrometer to millimeter of either OFHC Cu (oxygen free high conductivity copper) or Chromel-A (a NiCr alloy of 80% nickel and 20% chromium). The 3D weaving process essentially stacks pairs of

orthogonally oriented warp and fill wires, which are then bound in process, with Z-wires that pass through the thickness. The wires are bounded together to create high stiffness lattice. In this section, we discuss how method explained in chapter 4 is adapted to capture the elastic constant of 3D woven metallic lattices: the material assumed to be orthotropic instead of isotropic.

Measuring natural frequencies

Resonant test at very small strain were performed to capture the natural frequnies and mode shapes of 3D woven metallic lattices. The experiment was carried out with a Laser Doppler Vibrometer (Polytec PSV-500). The experimental setup is depicted in Figure A. 1.

Figure A. 1 (a) Resonant test setup for Laser Doppler Vibrometer, (b) Piezoelectric with 3D woven lattice attached to it.

The 3D woven material was excited with a piezoelectric actuator with a harmonic signal at a very low amplitude, sweeping the frequency between 0-5kHz. The sample was attached to the piezoelectric by using Petro wax. The velocity of the top wires in the sample at various locations were monitored by LDV to identify the frequency response and mode shapes. The average frequency response is depicted in Figure A. 2. It is worthy of mentioning that the in-plane modes cannot capture by this setup.

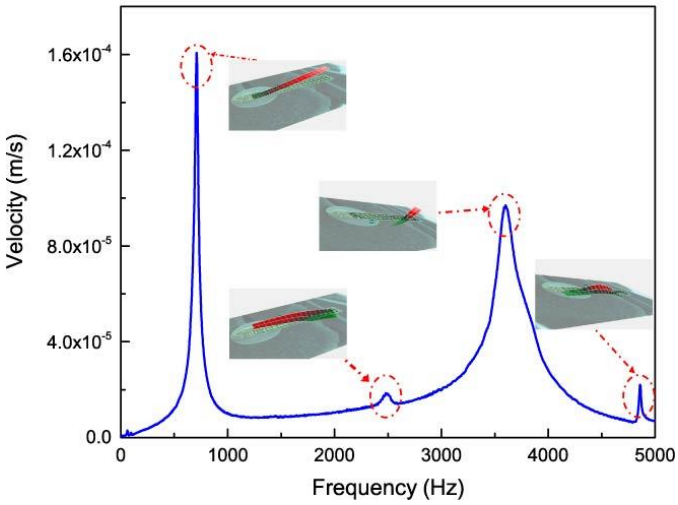

Figure A. 2 Average frequency response of 3D woven lattice captured by Laser Doppler Vibrometry.

As shown in Figure A. 2 the natural frequencies are ~700Hz, ~2400Hz, ~3600Hz, and ~4800Hz. The mode shapes captured by LDV at these frequencies indicate that the first mode (at ~700Hz) is first bending mode, the second mode (at ~2400Hz) is first torsional mode, the third mode (at ~3600Hz) is second bending mode, and the forth mode (at ~4800Hz) is second torsional mode (see insets in Figure A. 2).

Finite element simulations

As shown in chapter 4, the stiffness of microlattices can be accurately measured by using non-contact resonant approach. The LDV measurements coupled with Finite Elements Analysis (FE) is used to extract the Young's modulus in ultralight microlattices. The same technique is applied in this study to measure the normal and shear stiffness of 3D woven metallic lattices; however, the material is defined as orthotropic in 3D woven lattices. Finite Element simulations were preform with ABAQUS to extract the relation between natural frequencies and all stiffness components. The sample with dimensions of $4.8mm \times 3mm \times 22mm$ (Figure A. 3) was modeled as orthotropic solid with nine engineering constants ($\nu_{xy}, \nu_{xz}, \nu_{yz}, E_x, E_y, E_z, G_{xy}, G_{xz}$, and G_{yz}).

The rectangular sample were meshed with 8-node linear solid elements (C3D8R) and linear perturbation analysis were performed to extract natural frequencies of the sample. The density of the core was measured by weighing the lattice and dividing the mass by the volume (3043kg/m^3).

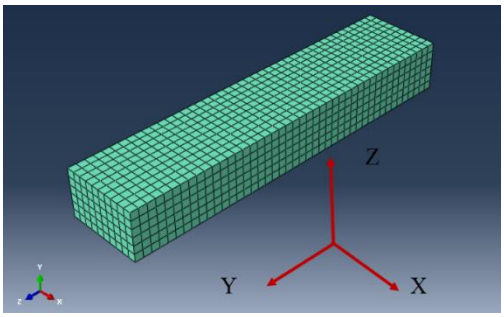

Figure A. 3 Sample modeled in FE simulation and the corresponding coordinate system.

In order to investigate the sensitivity of natural frequencies of the sample to each engineering constant, few simulations were preform on ABAQUS and at every simulation one of the constants was changed. The results indicate that changes in natural frequencies are negligible when the Poisson ratios varies between 0-0.5, therefore $\nu_{xy} = \nu_{xz} = \nu_{yz} = 0.3$ is used for all simulations. Moreover the results show ~0.8% changes in natural frequencies when E_x, E_z, and G_{xz} varies by factor of 5-10. Since the stiffness constants, E_x, E_z, and G_{xz}, are not affecting natural frequencies, they are assumed to be 1Gpa, 1GPa, and 0.5GPa, respectively for all simulations for the sake of finding other engineering constants. Note that out of nine engineering constants for orthotropic materials, three of them (E_y, G_{xy}, and G_{yz}) affect the natural frequencies and can be measured by using this technique.

Thousands of input decks were generated by using Python code in which the longitudinal stiffness, E_y, was swept from 100MPa to 5GPa with the step size of 100MPa and the in-plane shear stiffness, G_{xy}, and out-of-plane shear stiffness, G_{yz}, were swept from 50MPa to 2GPa with

the step size of 100MPa. These simulations ran on the HPC cluster. The results were analyzed and the natural frequencies are extracted as a function of longitudinal stiffness E_y, in-plane shear stiffness G_{xy}, and out-of-plane shear stiffness G_{yz}.

Natural frequencies captured from FE simulations were matched to the natural frequencies of the 3D woven sample measured with LDV and the longitudinal stiffness, E_y, in-plane shear stiffness, G_{xy}, and out-of-plane shear stiffness, G_{yz} were extracted for the sample.

According to the continuum FE simulations, the first four eignmodes (Figure A. 4) are first bending mode, first in-plane mode, first torsional mode, and second bending mode; however, the sequence varies according to the stiffness properties in each simulation.

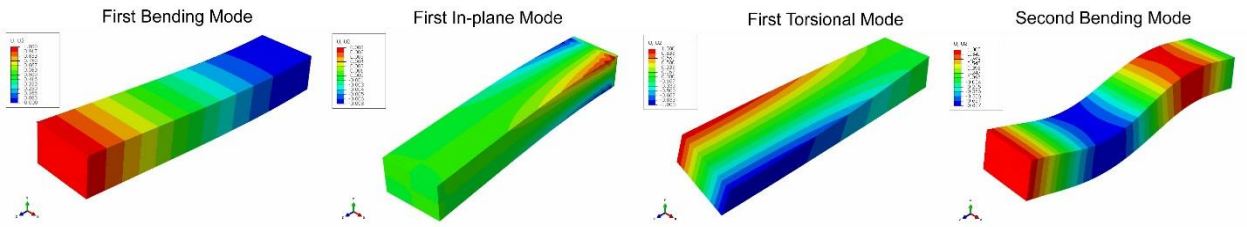

Figure A. 4 Mode shape captured by FE simulation. From left to right: first bending, first in-plane, first torsional, and second bending modes.

The first bending, second bending, and first torsional modes captured by resonant measurement are matched within 5% error to the first bending, second bending, and first torsional modes captured by the FE simulations, respectively. Note that the second torsional mode is coupled with in-plane mode due to the geometric imperfections and cannot be used to extract the stiffness. The comparison indicates that out of 19000 simulations, there are three simulations in which the first 3 modes match to the experimental results. These three simulations have an in-plane shear modulus of $G_{xy} = 250MPa$, and out-of-plane share modulus of $G_{yz} = 150MPa$; however, the longitudinal stiffness E_y varies between 1.6-1.8GPa.

The 4-point bending test was performed on the same sample, and 1GPa longitudinal stiffness was measured. The 4-point bending measurement underestimated the stiffness of the material due to the deformation and movement of the wires as well as bounding between them.

Moreover, the finite element simulation is performed on woven cantilever sample represented with the wire models (Figure A. 5). The wires were modeled using: (A) solid elements and (B) beam elements. Brazing was modeled with the solid elements in model A, and with beam elements in model B. Eigen analysis requires all components to have well defined boundary conditions with no rigid translations; therefore, 'freely floating' fill wires were removed from model A to enable the eigenvalue analysis. Such model 'treatment' has negligible effects on the stiffness since loose wires do not contribute directly to the stiffness; however, removing such wires reduces the overall mass of the system and increases its natural frequency. Eigenvalue analysis of the solid element model A returned the following modes: 1200 Hz (first bending mode), 2600 Hz (first torsional mode), 4200 Hz (second bending mode). The eigenvalue analysis of the solid element model A showed qualitative agreement with the experiment and the sequence of modes was well predicted but the modal frequencies were higher than anticipated. The first natural frequency (bending) was predicted as 1200 Hz, whereas the measured value was ~700 Hz; and, second mode (torsional) was simulated as ~2600 Hz whereas it was measured as 2400 Hz. The discrepancies can be explained by the fact that FE simulation underestimates the mass.

The beam model B, employs beam elements where the rigid motions of the 'floating' fill wires were eliminated by attaching one end of each fill wire to a fixed boundary point via a soft spring (less than 0.5% of each wire stiffness). This approach ensures that fill wires can move 'freely' (with negligible resistance), while enabling the eigenvalue analysis. Eigenvalue analysis yields ~500 Hz for first bending mode frequency, and ~1000 Hz for first torsional frequency.

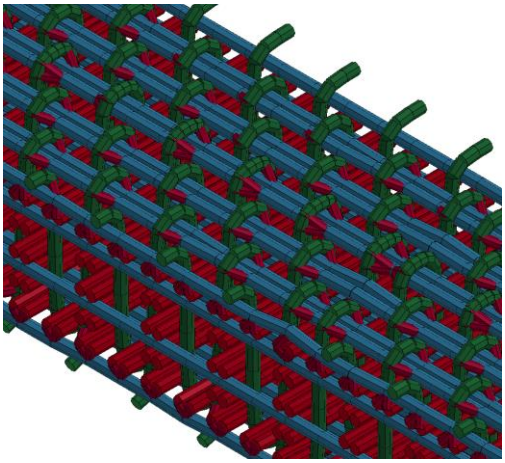

Figure A. 5: Woven lattice model consisted of solid element.

Natural frequencies of the solid elements (A) and beam elements (B) enveloped the experimental results. The beam model under predicted natural frequencies because beam elements underrated the true stiffness and the bonds; On the other hand the solid element model assumes solid connection between all neighboring nodes, whereas according to previous studies, the woven lattice bonds are not achieved perfectly for all nodes, hence resulting in overestimating frequencies.

To summarize, the engineering constants of the 3D woven materials are measured by using Laser Doppler Vibrometry and FE simulations. The out-of-plane measurements used to captured longitudinal stiffness E_y, in-plane shear stiffness G_{xy}, and out-of-plane shear stiffness G_{yz} while in-plane measurements can be used to measure E_x, E_z, and G_{xz}. The comparison between the measured frequency and the FE simulations confirms the accuracy of the model.